



IFSTTAR

Département Composants et Systèmes – Laboratoire LISIS

École Polytechnique

Laboratoire de Physique des Interfaces et Couches Minces

Thèse présentée pour obtenir le grade de
DOCTEUR DE L'ÉCOLE POLYTECHNIQUE
Spécialité : Physique

par **Fulvio MICHELIS**

Suivi immergé de durabilité du béton par nano capteurs sans fil

Wireless Nano Sensors for Embedded Durability Monitoring in Concrete

Soutenue vendredi 9 octobre 2015
devant le jury composé de

Rapporteurs	M. Paolo BONDAVALLI M. George MALLIARAS	Thales Research and Technology École Nationale Supérieure des Mines de Saint-Étienne
Examineur	M. Thierry GACOIN	Ecole Polytechnique - LPMC
Invité	M. Michel HARDY	Engie CRIGEN
Directeur de thèse	M. Yvan BONNASSIEUX	Ecole Polytechnique – LPICM
Encadrante référente	Mme Bérengère LEBENTAL	IFSTTAR
Encadrante	Mme Laurence BODELOT	Ecole Polytechnique - LMS

Thèse préparée dans le Département Composants et Systèmes de l'IFSTTAR et dans le Laboratoire de Physique des Interfaces et Couches Minces de l'École Polytechnique.

Research funded by the French institute of science and technology for transport,
spatial planning, development and networks (IFSTTAR)

Recherche financé par le 'Institut français des sciences et technologies des
transports, de l'aménagement et des réseaux (IFSTTAR)

MERCI, THANKS, GRAZIE

Pendant cette thèse j'ai eu la chance d'être supporté par une multitude de personnes qui ont facilité la réussite de cette thèse grâce à leur aide et à leur expertise.

En premier, je voudrais adresser un GRAND, GRAND merci à Bérengère pour ses conseils, pour sa patience et pour son encouragement. Elle a été le principal pilier à la base de cette thèse!! De plus, les échanges continus avec elle m'ont formé et guidé dans ce monde de la recherche et de l'innovation. Merci.

Merci également à Yvan, pour avoir soutenu énergiquement cette thèse et pour sa direction. Cette thèse doit aussi beaucoup à Laurence, pour sa disponibilité et son assistance soutenue.

De plus, je voudrais exprimer ma gratitude envers Jean-Marc Laheurte pour m'avoir accueilli dans son laboratoire et m'avoir fourni son expertise pour le développement de l'antenne.

Je suis très reconnaissant envers Jean Charles Vanel pour sa collaboration sur le développement du circuit électronique, et pour avoir participé avec tant d'idées nouvelles.

Je voudrais remercier le support technique fondamental et les conseils d'Eric Piedallu, Sandrine Moscardelli, Sandrine Marceau, Erick Merliot, Jean-Luc Bachelier, Jean-luc Sorin, Denis Tondelier, Eleonor Caristan, Garry Rose et Frédéric Farci.

Pour leur apport important pendant leurs stages, je voudrais exprimer ma gratitude à Fadi Zaki, Benjamin Caduc, Yaowu Zang, Aladdin Kabalan et Houssam Retima

Je remercie toute l'équipe du PICM à l'Ecole Polytechnique et le LISIS à l'IFSTTAR pour leur soutien pendant ces trois ans. Un remerciement particulier aux collègues doctorants pour l'atmosphère détendue et amicale.

Si pendant ces trois ans de thèse j'ai pu me rapprocher du monde de l'enseignement, c'est principalement grâce à Jean-Luc Polleux. Merci beaucoup pour la confiance et pour m'avoir offert cette grande opportunité !

Un ringraziamento alla mia famiglia per il loro supporto fisico, logistico e morale in questi tre anni non sempre facili. Vorrei terminare con un ringraziamento speciale per B! L'averti al mio fianco è stato fondamentale!

MERCI, THANKS, GRAZIE!

RÉSUMÉ

Suivi immergé de durabilité du béton par nano capteurs sans fil

Mettre en œuvre le développement durable en construction nécessite de prolonger la durée de vie des structures grâce à la détection précoce des fragilités structurales. Celles-ci trouvent très souvent leur origine au cœur même des structures, au niveau de défauts micrométriques. Détecter ces défauts in situ et en temps réel représente un défi scientifique et technologique majeur et aucune solution bas coût n'est actuellement disponible. Cette thèse présente le premier nanocapteur intelligent sans fil pour le suivi noyé des structures en béton.

Le système est composé de trois parties : un élément sensible, un circuit de conditionnement du signal, et une antenne. Le premier est un capteur de déformation fabriqué par impression jet d'encre de nanotubes de carbone sur polymère. Ces capteurs sont fabriqués en série, jusqu'à 140 à la fois. Ils ne présentent pas d'hystérésis, résistent aux cyclages mécaniques, et sont très reproductibles en termes de résistance et de sensibilité (en température et en déformation) au sein d'une même série. Les capteurs sont sensibles également au pH et à l'humidité, ce qui suggère que cette technologie pourrait être adaptée à la création de nano capteurs multifonctionnels.

Le circuit de conditionnement est à bas coût et faible consommation énergétique. Il met en forme le signal du capteur tout en compensant sa sensibilité à la température. L'antenne a été conçue pour maximiser sa portée à cœur du béton, permettant ainsi la communication sans fil des mesures du capteur vers l'utilisateur. Le système, protégé par un boîtier spécialement conçu, est alimenté par une batterie pour une durée de vie estimée à plus de 5 ans. Le volume total du système final est plus de 3 fois inférieur à l'état de l'art des capteurs noyés.

De nombreuses expériences en laboratoire ainsi que dans une structure en béton de taille réelle suggèrent que le dispositif est capable d'observer à la fois l'ouverture de micro fractures dues à des charges appliquées et les déformations micrométriques dues à des dilatations thermiques. De plus, nos capteurs à base de nanotubes ont montré une durabilité plus importante au cœur du béton que des capteurs de déformation métalliques commerciaux.

En conclusion, les résultats scientifiques et technologiques de ces travaux montrent le fort potentiel applicatif des nano capteurs sans fil pour l'instrumentation noyée des matériaux cimentaires.

ABSTRACT

Wireless Nano Sensors for Embedded Durability Monitoring in Concrete

Making the construction industry more sustainable requires the extension of the life of structures, achievable through the anticipation of structural deficiencies. Structural deficiencies often originate at the core of concrete structures from micro scale defects, whose detection is the key to predict structural ageing. The in-situ, real-time detection of such defects remains a major scientific and technological challenge and no cost effective technique is currently available. In this thesis, we present the design, fabrication and validation of the first wireless nano sensor node for embedded monitoring of concrete structures.

The device is composed of 3 main parts: a sensing element, a conditioning circuit and an antenna. The first is a highly reproducible, hysteresis-free, flexible sensor fabricated by inkjet printing carbon nanotubes (CNTs) on polymer. We achieved the batch production of more than 140 sensors and also demonstrated low dispersion in device resistance as well as in its sensitivity to strain and temperature. The sensor also responds to humidity and pH, indicating that this fabrication process is adapted to the creation of a multifunctional nano sensor.

The low-cost, low-power conditioning circuit adapts the sensors' output to the input requirements of a regular analog-to-digital converter (ADC), compensating for temperature sensitivity. The antenna is specifically designed to maximise transmission through concrete for the wireless communication of the measurements. Power is supplied by a battery enabling the operation of the node for over 5 years. The circuitry is housed in a protective casing to insulate it from the harsh concrete environment. The volume of the assembled device is more than 3 times smaller than state of the art embedded nodes for concrete.

The devices are tested both in laboratory conditions and in real-size concrete structures. The outputs of the sensors embedded in a mortar slab under 3-point bending tests suggest that the devices are capable of detecting the opening of micro cracks caused by increasing load. Moreover, continuous outdoor deployment since December 2014 demonstrates that this setup may be capable of detecting thermal-induced micrometric deformations and suggests that our technology provides a higher durability for embedded monitoring than commercial metallic strain gauge.

In conclusion, the scientific and technological results of this research show the strong applicative potential of wireless nano sensors for embedded monitoring of concrete materials.

TABLE OF CONTENT

MERCI, THANKS, GRAZIE	I
RÉSUMÉ	III
ABSTRACT	V
TABLE OF CONTENT	VII
I. INTRODUCTION	1
I.1 Structural Health Monitoring of concrete structures.....	5
I.1.1 Motivations for Structural Health Monitoring	5
I.1.2 Requirements for Structural Health Monitoring	5
I.1.3 Surface Structural Health Monitoring	6
I.1.4 Limitations of Surface Structural health monitoring.....	8
I.1.5 Volume Structural Health Monitoring	9
I.2 Carbon Nanotubes: a promising material for embedded Structural Health Monitoring.....	13
I.2.1 Innovative propositions for detection of micro deformation	13
I.2.2 Self-sensing composites with embedded nano fibres.....	13
I.2.3 Multifunctional carbon nanotube sensors	15
I.3 Electronic architectures for volume Structural Health Monitoring.....	17
I.3.1 Wired technologies for SHM	17
I.3.2 Wireless technologies for SHM	17
I.4 Goal and added value of the thesis.....	21
II. FLEXIBLE CARBON NANOTUBE-BASED SENSING ELEMENT	23
II.1 Introduction	25
II.2 Added value of the produced sensing element.....	27
II.3 Methods.....	29
II.3.1 Fabrication.....	29
II.3.2 Physical and electrical characterizations.....	30

II.4	Characterization of deposition.....	35
II.4.1	Morphology of the carbon nanotube network	35
II.4.2	Device resistance	37
II.4.3	Reproducibility of the fabrication process	38
II.5	Piezoresistivity of the device - characterization.....	39
II.5.1	Piezoresistive behaviour for large deformations	39
II.5.2	Linearity and repeatability of the piezoresistive behaviour for small deformations	39
II.5.3	Response time.....	41
II.5.4	Quasi-static cyclability and hysteresis-free operation in quasi-static mode42	
II.5.5	Temperature compensation	43
II.5.6	Relevance of the device for crack detection in concrete	43
II.5.7	Conclusion.....	44
II.6	Piezoresistivity of the device – Model and Interpretation.....	45
II.6.1	State of the art.....	45
II.6.2	Outline of the simulation	46
II.6.3	CNTs modelled as straight rigid sticks.....	48
II.6.4	CNTs modelled as sinusoidal rigid tubes	53
II.7	Sensitivity to other parameters	63
II.7.1	Sensitivity to pH.....	63
II.7.2	Humidity sensitivity	63
II.7.3	Passivation.....	64
II.8	Conclusion : a flexible, multifunctional CNT-based sensing element.....	65
III.	WIRELESS ELECTRONIC PLATFORM FOR DATA ACQUISITION AND COMMUNICATION	67
III.1	Architecture of the wireless sensor node.....	69
III.2	Signal conditioning electronics	71
III.2.1	Goals and constrains.....	71
III.2.2	Inadequacy of the traditional Wheatstone bridge.....	72
III.2.3	Proposed architecture for signal conditioning.....	74

III.2.4	Simulation of the circuit.....	79
III.2.5	Circuit Fabrication.....	81
III.2.6	Characterization of the circuit.....	82
III.2.7	Perspectives.....	84
III.3	Analog-to-Digital conversion and management of the wireless communication protocol.....	85
III.4	Antenna.....	87
III.4.1	Goals and constraints.....	87
III.4.2	Design of the antenna.....	91
III.5	Assembly of the system.....	95
III.5.1	Components to be assembled.....	95
III.5.2	Assembly.....	95
III.5.3	Protection for embedded applications.....	96
III.6	Tests in mortar.....	97
III.7	Perspectives.....	99
III.7.1	Antenna optimisation.....	99
III.7.2	Energy harvesting.....	99
III.8	Conclusions.....	101
IV.	VALIDATION OF THE SOLUTION THROUGH APPLICATION	103
IV.1	Operation in mortar.....	107
IV.1.1	Methodology.....	107
IV.1.2	Results.....	109
IV.1.3	Conclusions and future work.....	112
IV.2	Operation in concrete.....	114
IV.2.1	Methodology.....	114
IV.2.2	Results.....	119
IV.2.3	Conclusions.....	124

V. CONCLUSIONS AND PRESPECTIVES	125
VI. APPENDIXES	129
VI.1 Appendix I – Optimisation of the fabrication process of the CNT-based..	131
VI.1.1 Preliminary test to optimize the fabrication of the CNT sensor	131
VI.1.2 Fabrication of the sensors.....	136
VI.2 Appendix 2 – Bibliography of the author.....	139
VI.3 Appendix 3 – Teaching and supervision of students.....	141
VII. BIBLIOGRAPHY	143

PART I.

INTRODUCTION

PART I.

INTRODUCTION

Infrastructure represents one of the main pillars on which the well-being of a State is based (World Economic Forum, 2014). An efficient transport infrastructure enables the circulation of people and goods, stimulating the global economy of the State. Ancient civilizations already recognised the essential role of infrastructures, which drove, for example, ancient Rome to develop an extended network of aqueducts and roads.

Infrastructures have to be repaired after damages appear to ensure their efficiency and long-lasting operation. Visual inspection to detect these damages is often impractical because of the size of the infrastructure, the cost related to the manpower and for safety reasons.

Structural Health Monitoring (SHM) of concrete infrastructures provide new and effective inspection techniques compared to visual inspection. They can offer more reliable and more frequent acquisition of information about the health of a structure. This thesis will focus on SHM of concrete structures.



Millau Viaduct: Millau, Midi-Pyrénées, France (HighestBridges.com, 2015)

I.1 STRUCTURAL HEALTH MONITORING OF CONCRETE STRUCTURES

I.1.1 Motivations for Structural Health Monitoring

The main goal of SHM is the performance assessment of a structure through the identification of potential damages and their impact on deficiencies. The assessment targets both regular aging as well as the consequences of catastrophic events. This introduces the first motivation behind SHM techniques: the rapid access to reliable information about the changes in the health of a structure. The safety of the people benefiting from the structure is increased if the structure itself is constantly under monitoring and an alarm is generated in case of problem.

Secondly, thanks to the quantity and quality of information given by reliable SHM techniques, it is possible to schedule targeted maintenance to repair damages while they are still confined and of small extent. In this case, the interest is economic since the restoration of small damages is easier and cheaper; moreover the lifetime of a structure is extended (Wenzel, 2009).

Thirdly, the access to continuous information on the health of a structure also allows to estimate its lifetime. This can help governments, local communities and infrastructure managers to organize their network of infrastructures by scheduling repair, replacement and programming improvements.

In addition, a strong scientific interest supports the close study of concrete infrastructure in order to better understand their behaviour and improve on future designs.

I.1.2 Requirements for Structural Health Monitoring

There are five keys to a reliable SHM technology (Wenzel, 2009):

- being precise enough to detect either damage or the symptom of an imminent deficiency,
- being able to identify the nature of the damage,
- being able to precisely locate it,
- providing enough information to understand the extent of damage, an essential piece of information for the assessment of a risk,
- The deployment of SHM technologies should not compromise the health and stability of the structure itself.

From these fundamental conditions, we can identify a few secondary requirements of SHM:

- sensing elements should provide information on the totality of the structure,
- the implementation and maintenance of SHM solutions should be less expensive than running regular manual inspection (where these are possible),
- the sensing elements should require little or no maintenance.

The different SHM solutions can be categorised in two main groups: Surface SHM and Volume SHM.

I.1.3 Surface Structural Health Monitoring

Surface SHM technologies are characterized by the use of technologies installed either on the surface of concrete structures or in their proximity. Different techniques are available and they offer different type of information on the health of a structure.

Precise triaxial **accelerometers** can be installed on the surface of concrete structures to study their vibration modes (Colybris, 2011). The shift of the vibrational modes allows the identification of structural deficiencies caused by excessive load.

Strain gauges (both metallic and fibre Bragg grating strain sensors) are very effective in assessing the macroscopic deformations of a structure. Metallic strain gauges change their characteristic resistance in response to strain (Figure I.1.1). Bragg gratings reflect different portions of the light spectrum as a function of the strain applied on them. Such sensors can be used both on concrete and on cables in case of suspension bridges and cable-stayed bridges (Baskar Rao, et al., 2009) (Cheng, et al., 2004). Recent development have ensured wireless capabilities for data communication (Cazeca, et al., 2013).

Thermography was found to be an effective technique to scan the surface of concrete structures and identify damages (FLIR Systems, Inc, 2011). Images taken at different times of the day can identify deficiencies (Figure I.1.1) since the temperature at the surface of concrete is highly influenced by the presence of irregularities (as a consequence of a change in conductivity and diffusivity of heat).

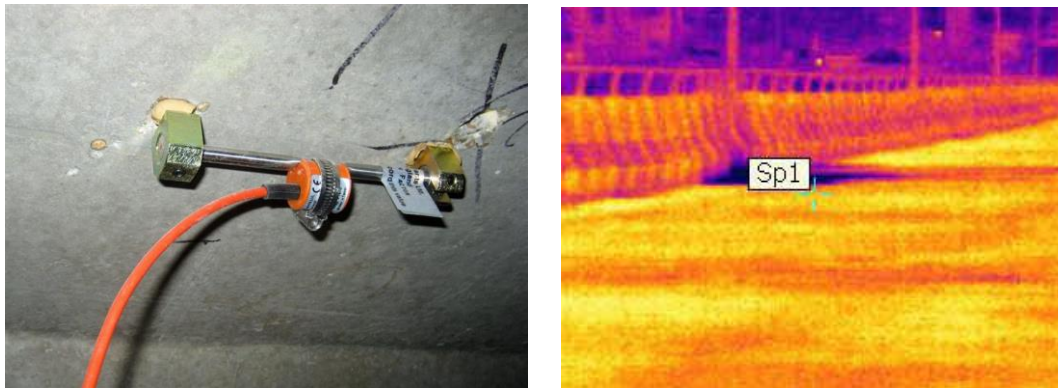


Figure I.1.1 on the left, a strain gauge attached to a concrete structure for the identification of macroscopic deformations (Test Consult, 2015). On the right, a thermal image of an expansion joint identifying penetration of moisture into the deck slab (FLIR Systems, Inc, 2011).

Some instrumentation, despite being installed on the surface, can monitor internal properties of concrete structures. Four main techniques can be implemented on the surface of concrete to study the interior.

First, it is possible to generate waves on the concrete surface and the analysis of their echo is used to study the interior of the material. The excited waves can either be **acoustic or electromagnetic** (Figure I.1.2).

The electromagnetic approach (also called **Ground Penetrating Radar or Surface Penetrating Radar**) uses waves between 500 MHz and 2 GHz and serves to identify air and water gradients for depths ranging between 3 and 50 cm.

Another approach utilises **acoustic waves**, generated by means of lasers, ultrasonic bursts or simply by impact. This technique is used to follow the evolution of drying, the resistance to compression, the Young's modulus, delamination and cracking. Generally, stress waves are used to study gradients of mechanical properties (Aouad, et al., 1993) (Dumoulin, et al., 2012) (Kharkovsky, et al., 2014).

Both techniques allow the evaluation of internal properties at a macro scale. The detection of micrometric information, such as the micro-porosity of the material, is unfeasible because the wavelength used in this type of applications is too long to evaluate parameters with a resolution at the micro scale. Smaller wavelengths are, on the other hand, not viable for two reasons: the excessive cost and complexity of the instrumentation required and the insufficient penetration of the waves at higher frequency (MO & ZHOU, 2009).

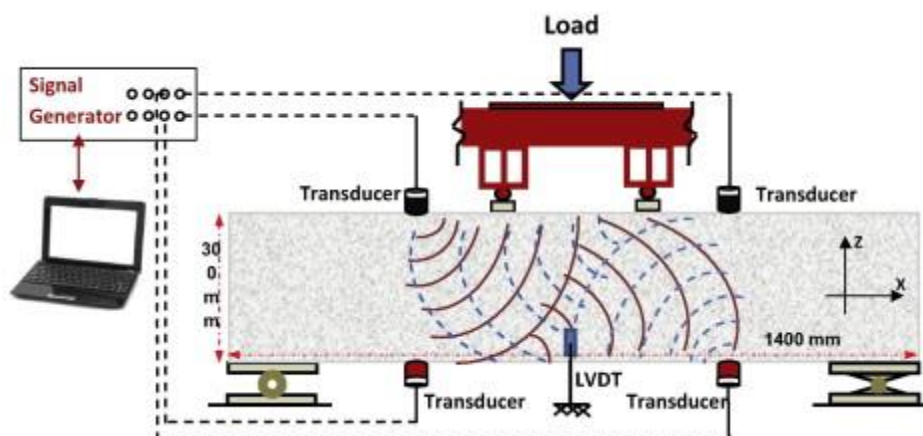


Figure I.1.2 Sketch of the instrumentation for the study of acoustic waves response of concrete slabs for different loading (Moradi-Marani, et al., 2014)

A second technique to evaluate the corrosion of rebars is the **measurement of the impedance** of a section of concrete (John, et al., 1981) (Park, et al., 2006). The study of the impedance can provide information on several parameters symptomatic of high porosity such as water saturation, concentration of chloride and temperature. A recent work describes the relevance of combining the measurement of impedance of concrete with the excitation of acoustic waves (Fursa, et al., 2014) for more precise evaluation of the strength of a structure.

The third technique consists in the study of **acoustic emission** generated and propagating inside the structure (Ohtsu, 1996). Brief acoustic signals that differ from the ambient white noise are associated with crack opening; their duration, amplitude and spectral content can describe the type of cracks generated.

I.1.4 Limitations of Surface Structural health monitoring

It is well established that perturbations of the concrete structure at the micro scale may evolve into structural deficiencies and failures affecting the efficiency and safety of a whole structure. Often, as shown in Figure I.1.3, the micro scale perturbations are generated within the structure itself and expand toward the surface to create visible damages such as spalling or delamination (Cusson, et al., 2011).

The detection of those micro scale perturbations at the core of concrete structures, symptomatic of ongoing ageing, is a major scientific and technological challenge. The techniques presented in the previous paragraph do not allow such low-scale monitoring.

In order to guide the development of new technologies adapted for the detection of perturbations at the micro scale, recent research identified the most indicative parameters to monitor.

One of the main drivers of concrete aging is the presence of micro-fractures inside the structure since it creates paths for faster diffusion of ions and gas from the exterior of the structure to the interior. For example, drying shrinkage leads to early age micro-fractures that increase the porosity of concrete; in turn, a higher porosity facilitates the transport of noxious ions such as chloride from the surface to the reinforcement bar, thus accelerating the oxidation of the reinforcement bars. During oxidation, the size of the rebars increases, producing internal stress in the structure that causes cracking, delamination and ultimately failure (see Figure I.1.3) (Cusson, et al., 2011).

Drying shrinkage, thermal contraction, restraint (external or internal) to shortening, and freeze-thaw cycles can also induce cracks opening and trigger the aging process from a very early stage of the life of a concrete structure.

Another symptom of faster ageing is higher content of SiO_2 . In fact, the redox reaction occurring between aggregates containing SiO_2 and alkaline metals (sodium and potassium) produces a hydrophilic gel that increases in size while absorbing the surrounding humidity. The internal pressure increases, causing eventually mechanical failure (Lukschová, et al., 2007).

In addition, the movement of gas and noxious chemicals through concrete is facilitated by the porosity of the material, but the driving factor is a gradient of pressure, humidity, concentration and temperature (Aïtcin, 2003) (Bentz & Garboczi, 1991). Consequently, the detection of gradients of these parameters is crucial.

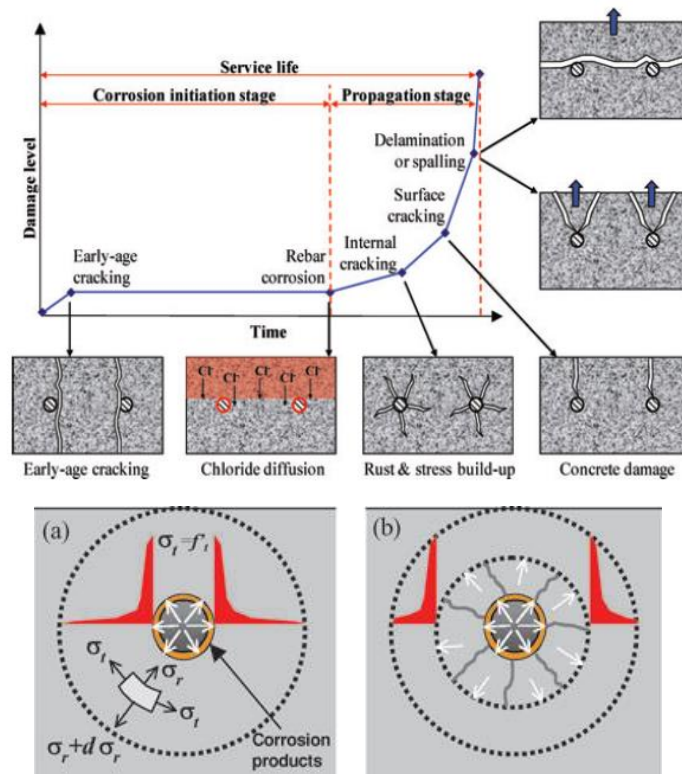


Figure I.1.3 Above, a diagram explaining how micro-cracks can be responsible of macro failures. Below, a model of crack propagation as a consequence of oxidation of rebars (Cusson, et al., 2011)

I.1.5 Volume Structural Health Monitoring

In recent years, new methods for the investigation of concrete properties were developed. All these new techniques exploit sensors buried inside the structure whose goal is to offer a precise and cost effective evaluation of micro scale properties of concrete. We refer to these techniques as Volume SHM.

As seen in I.1.4, the accelerating factors of concrete ageing are opening of micro cracks, porosity, and presence of gradients of humidity, temperature and concentration of chemicals. Consequently, the scientific community oriented its efforts on the development of sensors able to sense these particular parameters.

I.1.5.1 Detection of gradients

Several works demonstrated the feasibility of embedding wireless sensors inside concrete in order to study parameters like humidity, temperature and pH from inside the structure.

Early works focused on **humidity and temperature**, exploiting a combination of research and commercial solutions (Hansen, 2006) (Ong, et al., 2008) (Ogawa & Sato, 2008). Since then, more compact and precise electronic boards were developed, with important improvement such as the capability to manage collisions during communication (Barroca, et al., 2013) (Chang & Hung, 2012).

This capability is extremely important because it allows researchers to embed multiple sensors close to one another in order to have a more detailed analysis of temperature and humidity gradients.



Figure I.1.4 Radio Frequency Integrated Circuit (RFIC) sensor to measure temperature and humidity inside concrete structures (Chang & Hung, 2012)

Recent researches report also on the possibility of embedding wireless **pH** sensors and **chloride detectors** directly into concrete (Dong, et al., 2011) (Bhadra, et al., 2013).

I.1.5.2 Detection of internal stress in concrete structures

Considerable effort was put into the development of systems to study the material properties of concrete.

One technique is to embed piezoelectric transducers and load sensors. They can be exploited in two different ways: firstly, to sense **load distribution** and **internal swelling** (Tawie & Lee, 2010) (Zhu, et al., 2013), as internal sources of stress waves whose propagation will depend on the material properties (Divsholi & Yang, 2014). Secondly, they can detect the **evolution of vibrational modes** of the structure (Dongyu, et al., 2015).

I.1.5.3 Detection of internal deformation in concrete structures

The main technique to **sense internal deformation** is the use of strain gauges. Different approaches are available for embedded strain sensing.

The **Vibrating String** uses a steel wire tensioned between two ends (Figure I.1.5); deformations induce a relative displacement of the two ends, affecting the tension of the wire. By evaluating the evolution of the resonance frequency of the wire it is possible to infer the size of the deformation that occurred. (Sisgeo SRL, 2015) (RTS Instruments Ltd., 2015) (Geokon Inc., 2015) (Rocktest Telemac, 2015). The size of such sensors varies from a minimum of 5 cm to a maximum of 25 cm. Their resolution is normally around 0.4 $\mu\epsilon$. They show long term stability, enhanced by the addition of a thermistor for temperature compensation.

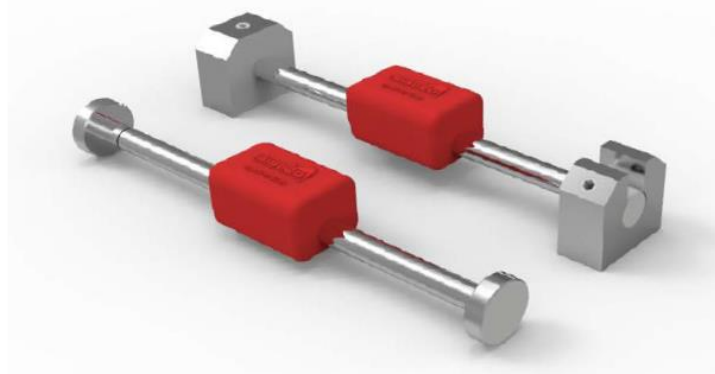


Figure I.1.5 Vibrating wire strain gauges (Sisgeo SRL, 2015)

The **Rebar Strainmeters** (Figure I.1.6) can be used in two ways. Firstly, they can be welded to the rebar cage before pouring concrete in order to measure concrete deformation due to imposed loads. When two devices are installed on either side of the neutral axis of a portion of structure, bending moments can be analysed in addition to axial loads. In addition, rebars strainmeters can detect the swell of the bar, thus detecting ongoing oxidation. This type of device is also coupled with a thermistor for temperature compensation and is relatively unaffected by moisture. The main drawback is that each device has to be tested and calibrated at installation, increasing the total installation cost (Geokon Inc., 2015).



Figure I.1.6 Rebar Strainmeters (RST Instruments Ltd., 2015)

Optical fibres can be exploited for the measurements of both local and distributed strain (Shan, et al., 2014) (Figure I.1.7). Even if the instrumentation is bigger and more expensive, optical fibres are currently the most developed and exploited technique for strain sensing. Their resolution is usually higher than vibrating wire ($0.15 \mu\epsilon$ compared to $0.4 \mu\epsilon$) and they can be used in environments where the use of vibrating wires is not indicated due to space consideration or high level of electrical interferences (Gekon Inc. , 2015).



Figure I.1.7 Fibre Optic Strain Gage (Gekon Inc. , 2015)

Despite being highly performing and precise, optical fibres have two main drawbacks:

-
- a cable (fibre or electrical cable) traverses the external surface, thus creating a channel for aggressive chemicals,
 - the detection of macro deformation is often not enough for a precise assessment of the health of a structure.

I.2 CARBON NANOTUBES: A PROMISING MATERIAL FOR EMBEDDED STRUCTURAL HEALTH MONITORING

I.2.1 Innovative propositions for detection of micro deformation

To go beyond the technologies presented in I.1.5.2 and detect micro cracks, several studies focused on new technologies. Some attempts were based on the **adaptation of commercial strain gauges** for embedded measurement (Pandit, et al., 2013) (Sounthararajan & Sivakumar, 2013), but all the proposed solutions require cables to supply and read the sensor.

Other groups proposed solutions to the problem of using wires. The common idea is to use an antenna coupled to a 3D metallic frame or a 2D resonant loop; when the object is deformed or moved (closer or further away) from the antenna, a **shift in the resonant frequency of the antenna** is detected (Fallah Rad & Shafai, 2009) (Ogawa & Sato, 2008).

The interpretation of the results of this type of sensor is very difficult. In fact, several parameters can be responsible for the frequency shift, among which temperature, humidity or pH changes and the correction of this parasitic parameters can be problematic.

Because of the numerous shortcomings of the technologies based on conventional commercial sensors and conventional architecture, the interest shifted toward innovative materials.

Technologies based on nano materials seem promising candidates in providing low-cost, compact, durable and highly sensitive techniques to study concrete properties at a micrometric scale.

I.2.2 Self-sensing composites with embedded nano fibres

One innovative technique that was investigated is the possibility of **embedding conductive nanoparticles** in concrete in order **to create a self-sensing material** (Reza, et al., 2003) (Yu & Kwon, 2009) (Xiao, et al., 2011) (Azhari & Banthia, 2012) (Baeza, et al., 2013) (Han, et al., 2015). The filler used to create the new composite material is usually highly conductive and the quantity of filler embedded in the concrete mixture is big enough to create a percolating network of the filler inside the concrete matrix. The electrical resistance of the composite changes as it acquires damage. This solution does not require any additional sensors embedded inside the structure because the structure itself has sensing capabilities. Moreover, the right filler embedded in the matrix can strengthen the structure itself. The most promising filler for such application are carbon nanotubes (CNTs) for their high aspect ratio, superior electrical conductivity and excellent strength (Bellucci, 2005) (Sinnotta & Rodney Andrews, 2001). Metal fillers (such as steel fibres and steel shavings) are the second kind of conductive fillers typically used in applications. Several kinds of fillers can be combined to cover several length scales of fillers.

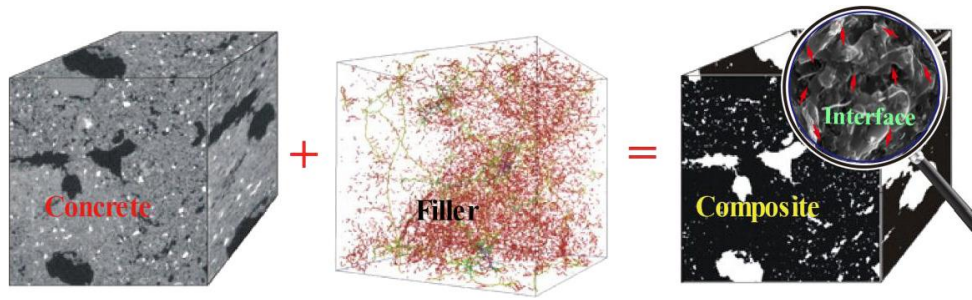


Figure I.2.1 Schematic representation of the fabrication of self-sensing concrete (Han, et al., 2015).

On the other hand, such approach has a few strong drawbacks:

- fabrication costs are quite high since a large amount of filler is usually needed to attain the percolation threshold,
- embedding large quantities of microfibers raises the question of their dispersion in the environment following regular wear and the health threat that this may represent,
- the fabrication of the composite is complicated because of difficulties in mixing uniformly microfibers in concrete and because of sedimentation issues of the filler.

A novel approach to self-sensing composite fabrication was suggested, based on a thin Multi-Walled CNT (MWCNT) piezoresistive layer embedded directly within a matrix to sense compressive and tensile stress (Lebental, et al., 2014) (see Figure I.2.2). Since CNTs are embedded inside the matrix and less CNTs are required, the method solves a few problems of self-sensing composite. However the method was developed for asphalt materials and it is difficult to adapt to concrete since it is in liquid phase while it is poured.

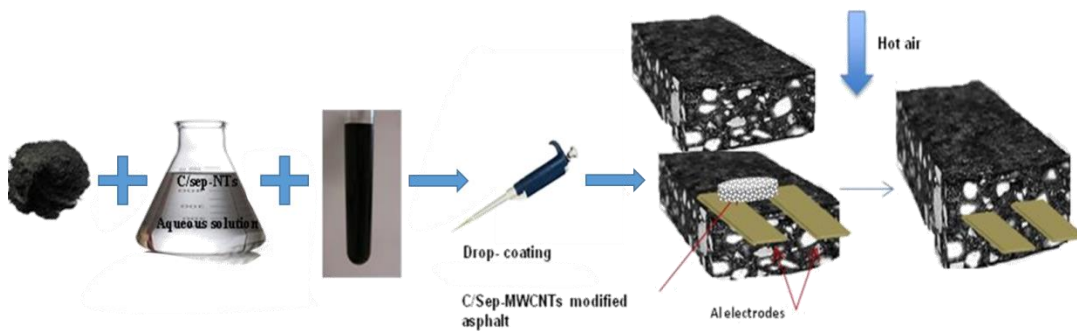


Figure I.2.2 Fabrication process of functionalized asphalt by insertion of a thin film of graphene-on-clay and CNTs (based on (Ghaddab, et al., 2014).

Another approach consists of mixing CNTs in a polymeric matrix for the fabrication of a self-sensing brick, ready to be embedded in concrete (Zhang, et al., 2013) (Srivastava, et al., 2011) (Yin, et al., 2011) (Figure I.2.3). Typically, the resulting sensors show good sensitivity to mechanical deformations and the fabrication process is quite reproducible and cheap. On the other hand, being CNTs embedded in the polymeric matrix, they are not in contact with the concrete

environment, thus impeding any other type of sensing. Moreover, it has limited downscaling capability and is poorly compatible with regular integrated electronics.

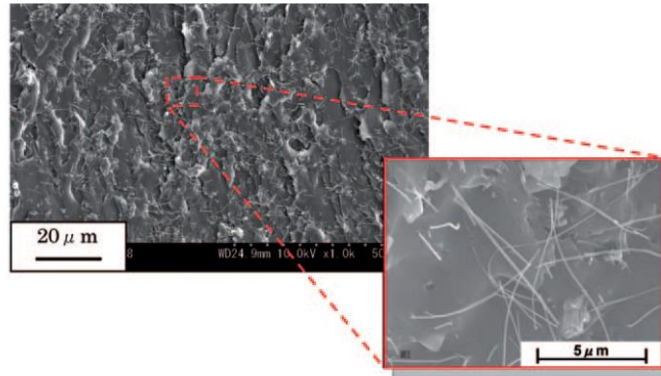


Figure I.2.3 SEM images of MWCNT embedded in epoxy (Yin, et al., 2011).

I.2.3 Multifunctional carbon nanotube sensors

Among the wide selection of nano particles and nano fibres, an increasing interest is oriented toward CNTs. In fact, several studies show that **CNTs can be functionalised to be sensitive to a wide selection of quantities** such as humidity (Han, et al., 2012) (Cao, et al., 2011), chemical species (Wang, 2005) (Kong, et al., 2000), pH (Kaempgen & Roth, 2006) (Gou, et al., 2014) **and**, if properly treated, they can **show excellent selectivity** (Balasubramanian & Burghard, 2005) (Scardaci, et al., 2012). The multifunctionality is an important aspect for SHM; in fact, with minor changes to the fabrication process, it is possible to fabricate sensors that are highly sensitive to different parameters and, if combined, they would be capable of providing detailed and complete information on the health of a structure. The interest is having only one technology instead of a group of technologies that are not always compatible. The research, consequently, moved forward to suggest other method for embedding CNTs in concrete.

Other groups demonstrate the possibility of spinning CNT arrays to create CNT yarns (Zhao, et al., 2010) or to create “fuzzy” CNT fibre by directly growing CNTs on fibre glass (Sebastian, et al., 2014). Despite having produced sensors with high sensitivity, their fabrication process is difficult and expensive, discouraging their use in applications that require a large quantity of sensors to be produced and embedded.

Finally, one approach consists in **depositing a network of CNTs directly on various substrates**. This technique yields planar (2D) devices, highly sensitive to mechanical deformation and with a highly rough surface exposed to the environment. For mechanical sensing applications, this surface can be covered to ensure isolation from the surrounding environment, but it can be also treated to be sensitive to specific chemicals and its high roughness contribute to excellent sensitivity. Consequently, such devices can fulfil the goal of having multifunctional sensors.

In this thesis we will present the fabrication of a novel sensor based on direct deposition of CNTs on polymer, suited for embedded measurement in concrete (Section II). This device shows clear sensitivity to mechanical deformation and early results demonstrate its sensitivity to pH and humidity, a promising start toward multifunctionality.

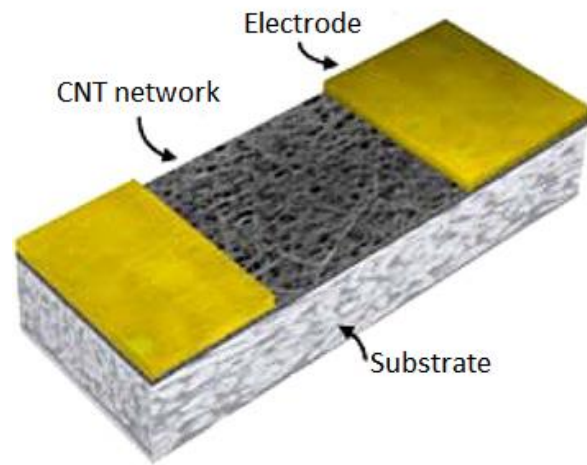


Figure I.2.4 Device fabricated by depositing a network of CNT directly on a substrate (based on (Han, et al., 2015)).

I.3 ELECTRONIC ARCHITECTURES FOR VOLUME STRUCTURAL HEALTH MONITORING

Before continuing in the discussion in the chapter we would like to explicit the terminology used in the present work. The term “sensor” takes two different meanings depending on the research community: either sensing element or sensor node. Here we use the term “sensing element” to identify for the physical device that changes its properties as a function of an external excitation (example are strain gauges, temperature probes, etc). On the other hand, the term “sensor”, in agreement with the past and present literature, is used to indicate the entire embedded element composed of the sensing element, the electronic circuit and the antenna (Paek, et al., 2005) (Kim, et al., 2006) (Hu, et al., 2013) (Ha, et al., 2014) (Cahill, et al., 2014).

As all sensors, SHM sensing elements need to be paired with an electronic circuit for the acquisition of the measurements. The electronic structure of such circuits depends upon the goal of the SHM device. Two main categories can be identified: wired early works and wireless technologies.

I.3.1 Wired technologies for SHM

In early works the different sensors were installed with wires as it simplified the communication and the problem of power supply (Li, et al., 2006) (Hsieh & Hung, 2008). However, for big structures, cabling tasks raise concerns about installation costs (Wenzel, 2009). Wired technology creates a bias and facilitates ion ingress in embedded applications, demonstrating the need of wireless technologies for volume SHM. This thesis will not cover in any detail the proposed options of wired SHM solutions.

I.3.2 Wireless technologies for SHM

Wireless technologies and their circuit architectures vary greatly depending upon the measurand, the acquisition frequency, the power supply, and the goal of the measurement. In this work, we categorised the different architectures according to the type of measurement: surface or volume measurements.

I.3.2.1 Wireless technologies for surface SHM

The first report of a wireless architecture specifically developed for SHM is a patent published in 1998 (Straser, et al., 1998). The proposed system aims at the monitoring the surface of civil structures during structural overloading caused by a natural hazards or extreme events. The system comprises a plurality of sensor units installed at different locations in the structure, and each sensor unit comprises a sensing element, a conditioning circuit, a data acquisition circuit and a digital wireless transmitter. This architecture inspired later work on bridges and was adapted to the installation of accelerometers, strain gauges, inclinometers, temperature sensors and anemometers (Lynch, et al., 2003) (Wang, et al., 2005) (Ko & Ni, 2005). Some solutions are battery powered and others harvest solar and wind energy

The electronic industry commercialised the first proprietary platform for the creation of wireless sensor nodes; among others, the commercial technologies exploited are the Mica Mote by Crossbow Technology (Crossbow Technology Inc., 2005), Imote and Imote2 by Intel (Nachman, et al., 2005) (Intel, 2006) and IRIS Mote by MEMSIC (MEMSIC Inc., s.d.).

Despite not being specifically developed for SHM, these commercial solutions simplified the development of sensor nodes. In fact, providing an easy-to-use platform for signal conditioning, digital acquisition and data transmission, they simplified the fabrication of prototypes based on innovative sensors (Kim, et al., 2007) (Cho, et al., 2008) (Ceriotti, et al., 2009) (Barroca, et al., 2013).

Moreover, these commercial devices boosted the research on finding optimal organizations of wireless networks for SHM applications (Kottapalli, et al., 2003) (Kim, 2005) (Wang, et al., 2005) (Smarsly & Lawb, 2014).

Despite their adaptability, these commercial solutions presented a few drawbacks: their power consumption, the impossibility to modify their circuit to host more sensing elements and a limited range of communication. Consequently, several groups focused on the design and fabrication of more efficient platforms customized for SHM (Lynch & Loh, 2006) (Whelan, et al., 2009) (Le Cam & Martin, 2011) (Bocca, et al., 2011).

Recently, some research reported on the first autonomous wireless devices exploiting a mixture of energy harvesting techniques (namely solar, thermal and wind energy) to ensure power supply (Sazonov, et al., 2009) (Le Cam & Martin, 2011) (Kurata, et al., 2011) (Chae, et al., 2012).

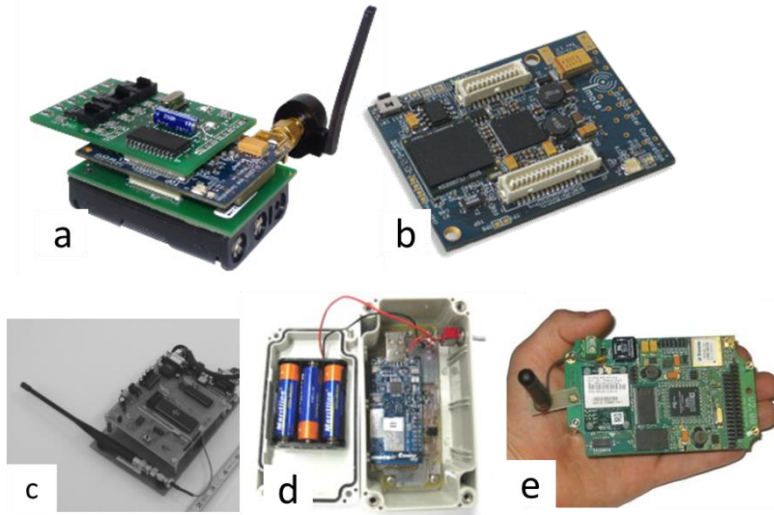


Figure I.3.1 Wireless sensor nodes for surface SHM. In the first line, commercial solutions: a) Mote2 (Crossbow Technology Inc., 2005), b) Imote12 (Intel, 2006). In the second line, the academic solutions: c) (Lynch, et al., 2003), d) (Whelan, et al., 2009) and e) (Le Cam & Martin, 2011).

I.3.2.2 Wireless technologies for volume SHM

The first paper of embedded wireless sensors was published in 2003. Two different groups developed an embedded sensor system to monitor and assess corrosion in concrete (Bernhard, et al., 2003) (Watters, et al., 2003). In (Watters, et al., 2003) we can find already **energy harvesting techniques** that ensure long lifespan in concrete.

Identec Solutions commercialised an embeddable Radio Frequency Identification (RFID) tag for temperature and humidity assessment: the i-Q32T (Identec Solutions, 2006). This device was then improved and substituted by the more recent version i-Q350 (Identec Solutions, 2012) that responds to the demand of devices capable of **communicating through a protocol that manages collisions in a crowded environment**. As seen in 0, several sensing element are needed in order to assess exhaustively the health of a structure. This device was largely used in SHM studies, mainly for the evaluation of concrete hardening (Hansen, 2006) (O'Connor, 2006) (Ogawa & Sato, 2008) (Chang & Hung, 2012).

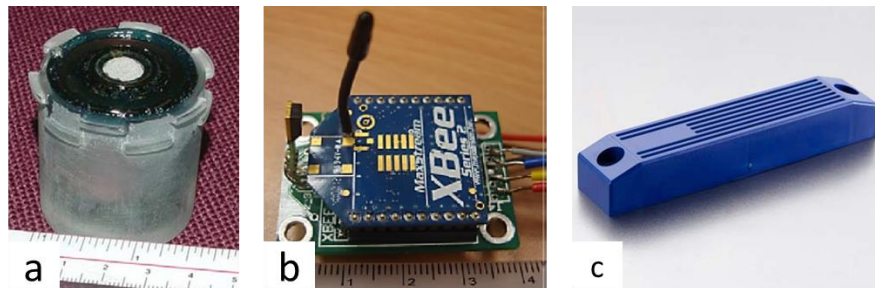


Figure I.3.2 Wireless sensor nodes for volume SHM. Academic solutions: a) Smart-Pebbles™ (Watters, et al., 2003), b) (Chang & Hung, 2012) . Commercial solution: c) iQ350 (Identec Solutions, 2012).

The previously presented solutions have the drawbacks of being quite big and, often, power hungry. Several studies solved these problems by fabricating a wireless device communicating by **shifting its resonant frequency** (Andringa, et al., 2005) (Srinivasan, et al., 2006) (Fallah Rad & Shafai, 2009) (Yu & Caseres, 2010) (Materer, et al., 2011) (Bhadra, et al., 2013) (Perveen, et al., 2014). The resonance frequency of the device (often a RLC circuit) is affected by the changes in the measurand. For example, a change in chloride concentration oxidises the connections of a RLC circuit, changing its conductivity; in turn, the resonant frequency is shifted (Andringa, et al., 2005). Mechanical deformation of the concrete can be sensed as well, since it can deform a resonating loop of an antenna, thus shifting its resonant frequency.

Looking at the evolution of this technology over the years, we can appreciate that it allows the fabrication of increasingly smaller devices that are fully passive, but on the other hand they present some major drawbacks. Firstly, a shift in resonant frequency is difficult to interpret and associate to a unique parameter (see I.2.1.). Secondly, this technique is not suited for crowded environments because the devices do not communicate following a well defined protocol, resulting in the incapacity of handling collisions. Finally, the instrumentation needed to interpret the frequency shifts is very expensive.

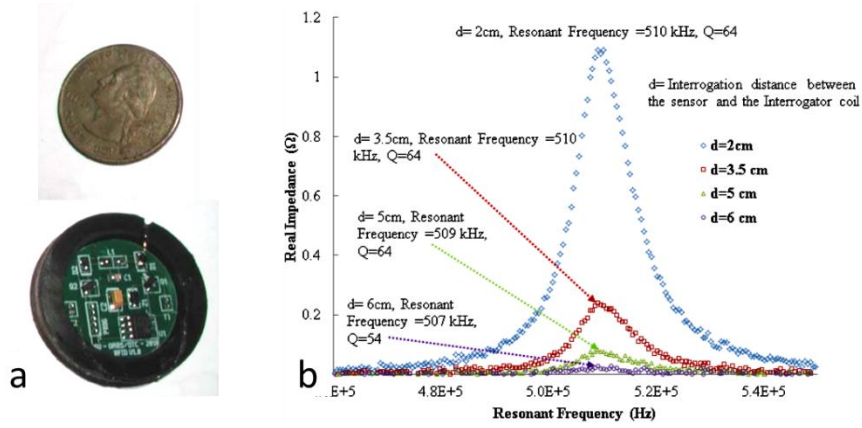


Figure I.3.3 Sensors based on frequency shift a) corrosion sensor (Materer, et al., 2011), b) shifts of the resonance frequency in the spectrum (Perveen, et al., 2014).

As discussed in I.2.3 the possibility of sensing multiple parameters at a time is a remarkable opportunity, but none of the studies published in the literature seem to focus on this.

We propose a novel architecture of a wireless sensor node capable of communicating several parameters at a time. The design of such a system is detailed in Section 0.

I.4 GOAL AND ADDED VALUE OF THE THESIS

A sustainable construction industry requires the extension of the life of structures, achievable through the anticipation of structural deficiencies. Structural deficiencies often originate from micro scale defects at the core of concrete structures and their detection is the key to predict ageing. However, the in-situ, real-time detection of such defects still remains a major scientific and technological challenge and no cost effective technique is currently available.

This work aims at filling this technological gap by proposing the first, fully functional wireless nano sensor node adapted for the detection of micro cracks inside concrete.

The goals of the thesis are built upon three major scientific challenges.

The first scientific challenge is to build a sensing element capable of precisely detecting micro deformations inside concrete. Such sensing element, in order to be cost effective and, thus, being a viable option for real applications, should be produced with low-cost materials and its fabrication process should be reproducible to allow its serial production.

The second scientific challenge is the development of a low-cost, small-size electronic system capable of decoding the output of the sensor element as well as sending the information to the outside of the structure.

The third challenge is the assembly and the fabrication of a robust packaging ensuring protection from the chemical and mechanical attacks to ensure long-lasting operation of the device in concrete.

The results presented in the following chapters demonstrate the accomplishment of these goals, bring embedded wireless monitoring of concrete structures one step closer to reality.

PART II.

FLEXIBLE CARBON NANOTUBE-BASED SENSING ELEMENT

PART II.

FLEXIBLE CARBON NANOTUBE-BASED SENSING ELEMENT

In this section, we primarily focus on the fabrication of a flexible strain gauge; then, we will study the possibility of it to other types of measurement such as pH and humidity.

II.1 INTRODUCTION

Owing to their very large specific surface area (Peigney, et al., 2001), carbon nanotubes (CNTs) have been of utmost interest for sensing applications since the early days of CNT research (Baughman, et al., 2002). Ohmic or transistor devices using CNTs deposited or grown on rigid substrates have demonstrated exceptional sensitivity to their environment, leading to various examples of analytical (humidity, pH, gas, chemical or biological species) (Kong, et al., 2000), mechanical (strain, pressure) (Li, et al., 2006) or radiation (thermal or infrared, UV) (Barone, et al., 2005) sensors. Following the quick rise of CNT-based flexible electronics (Bradley, et al., 2003), a wide range of flexible CNT sensors was proposed (Mabrook, et al., 2009), with the goal of providing the next generation of wearable devices (Yamada, et al., 2011) for human welfare monitoring or wireless sensor networks (Laflamme, et al., 2013) for infrastructure (Loh, et al., 2007) or environmental monitoring (Mauter & Elimelech, 2008). With their mechanical robustness (high Young's modulus, low bending rigidity, low buckling properties, high tensile strength (Baughman, et al., 2002) (Yu, et al., 2000)) flexible CNT sensors are expected to provide long-lasting, reliable devices compatible with industrial requirements.

The active component of these sensors most often consists of wet-processed carbon nanotube networks (CNNs) (Saha, et al., 2014). CNNs are films of randomly or partially organized CNTs and their thickness ranges from a few tens of nanometers to a few tens of micrometers. Their fabrication methods include filtration and extraction of buckypaper (Li & Kröger, 2012), spray coating (Lipomi, et al., 2011), layer-by-layer assembly (Loh, et al., 2007) as well as contact - roll-to-roll (Noh, et al., 2011) or transfer-based (Lau, et al., 2013)) - and non-contact - aerosol (Li, et al., 2014) or inkjet printing techniques (Lesch, et al., 2014). Studies have yielded strain gauges (Li, et al., 2014) (Cohen, et al., 2012), gas sensors (Rigoni, et al., 2014), photodetectors (Gohier, et al., 2011) and chemistors (Mirica, et al., 2013).

A long-standing, acute challenge for industrial applications of flexible CNN sensors lies in their low device-to-device reproducibility (Lee, et al., 2011). Reproducibility specifically addresses two factors, firstly, the standard deviation in initial device resistance, secondly, the standard deviation in device sensitivity.

Device-to-device variability has been discussed repeatedly with regard to CNN-based flexible resistors (Li, et al., 2014) and transistors (Wang, et al., 2012) and various causes have been reported, including liquid-phase dispersion issues of CNTs (Kim, et al., 2012), variability in CNT properties within a batch (semiconducting versus metallic, diameter, length, sidewall defects) (Lee, et al., 2011), quality of the CNT-to-electrode contacts or surface roughness of the flexible substrates (Saha, et al., 2014). In spite of this, most reports on flexible CNN sensors do not provide standard deviation data for resistance or sensitivity. A few papers mention the often wide range (min-max) of resistances covered by their devices (Mirica, et al., 2013). The only results currently available on standard deviation for CNN-based flexible sensors address inkjet-printed devices (Lesch, et al., 2014) (Benchirouf, et al., 2012). In (Lesch, et al., 2014), Lesch et al. report a standard deviation as low as 2.5% in the resistance of CNN electrodes inkjet printed on Polyamide, well beyond typical requirement for industrial devices.

Despite such success, none of the studies investigated the standard deviation on device sensitivity, although this is the most crucial parameter for sensing applications.

II.2 ADDED VALUE OF THE PRODUCED SENSING ELEMENT

In this work, we present the first example of batch-produced CNT-based strain gauges directly inkjet-printed on a flexible substrate, namely rough Ethylene Tetrafluoroethylene (EFTE).

We show the **high reproducibility of the fabrication process**, evaluated as the dispersion of the resistance of the strain gauge after fabrication.

We investigate the piezoresistive response of the sensor to demonstrate its linearity up to 600 $\mu\epsilon$ with an estimated Gauge Factor (GF) of 0.90. We present the **first quantitative evaluation of the variability of the gauge factor** for batch-produced CNT-based strain gauges. Moreover, we present a numerical model to better interpret the physical behaviour of the piezoresistive response of our sensor.

For implementation in real-life applications, we investigate the cyclability of the sensor and the possibility of compensating thermal sensitivity.

This work proves the relevance of inkjet printing for the batch fabrication of reproducible and reliable CNT-based strain gauges.

In conclusion, we demonstrate the sensitivity of such device to other physical quantities of interest, such as pH and humidity. Early results suggest the possibility of utilizing such device for the multifunctional sensing in concrete.

II.3 METHODS

II.3.1 Fabrication

In this section we present the standing fabrication protocol of the device. This protocol is the result of extensive tests and characterization, reported in Appendix I.

II.3.1.1 Materials

MWCNTs Graphistrenth C100 are purchased from Arkema. The solvents 1,2-Dichlorobenzene (Dichlorobenzene hereafter), Acetone and Methanol and the surfactant Sodium Dodecyl Benzene Sulphonate (SDBS) are purchased from Sigma-Aldrich. The substrates is a 0.125 mm thick, 30 cm by 30 cm foil of Ethylene Tetrafluoroethylene (ETFE) with 90 nm roughness (calculated as in (DeGarmo, et al., 2003)) supplied by Goodfellow.

II.3.1.2 Carbon nanotube ink preparation

The MWCNTs are dispersed in dichlorobenzene at 0.02 wt.% using an ultrasonic probe (Bioblock Scientific VibraCell 75043) operated at 150 W for 20 min followed by centrifugation at 10 kG for 4 h. In order to increase ink-wettability on ETFE and improve homogeneity of the deposition, SDBS at 0.3 wt.% is added to the supernatant using a 20 min sonication bath (see details in Appendix I) (Saha, et al., 2014). The resulting dispersion, called ink in the rest of the manuscript, is stable for over 3 months.

II.3.1.3 Device fabrication

The device structure is shown in Figure II.3.1a and b. The ETFE foils are first cleaned with acetone and dried under compressed air flow. Pairs of 100 nm thin, 5 mm x 5 mm gold electrodes spaced by 7 mm are deposited using thermal evaporation under vacuum (10^{-7} mbar). The MWCNTs are then deposited by inkjet printing using the customizable Dimatix Material Inkjet Printer 2800 with DMP-11601 cartridges. The cartridge is kept at room temperature during printing and the substrate is heated to 55 °C. The printing pattern is a 17 mm x 5 mm rectangle positioned to fully cover both electrodes of each device, in order to ensure proper electrical contact. Several layers can be printed successively depending on the properties targeted for the devices. Residual dichlorobenzene and surfactant are rinsed away by immersion and slight agitation in methanol and acetone for 8s each, followed by drying under compressed air flow.

The number of layers and the frequency of rinsing strongly impact the final device resistance. We optimized these parameters in order to reach device resistances below 1 M Ω (threshold value required for compatibility with commercial acquisition cards; see next section) while keeping the fabrication time manageable. Devices presented here are obtained from 20 printed layers rinsed every two layers. They are produced by batches of either 8 or 144 sensors on ETFE foils

(Figure II.3.1c). The time required for the production of 8 or 144 devices with 20 layers and rinsing every 2 layers is 3 and 5 days respectively.

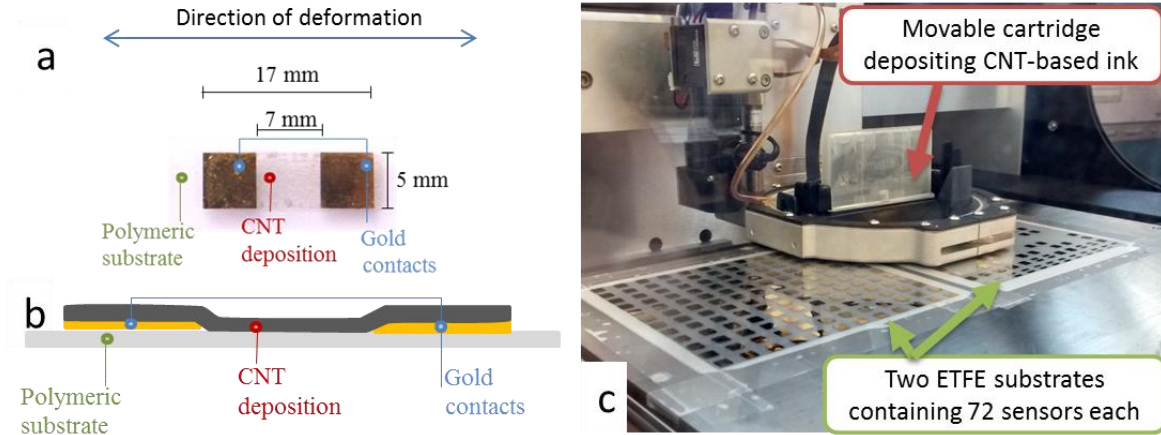


Figure II.3.1 a) Image of a CNT-based device printed on ETFE (top view) with device size and direction of deformation. b) Cross-sectional diagram of the device. c) Ink-jet printing of a 144-device batch on side-by-side ETFE foils. Each substrate contains 72 sensors.

II.3.1.4 Final device

After inkjet printing, the serial fabrication of the sensors is completed. Figure II.3.2 shows a batch of 72 sensors.

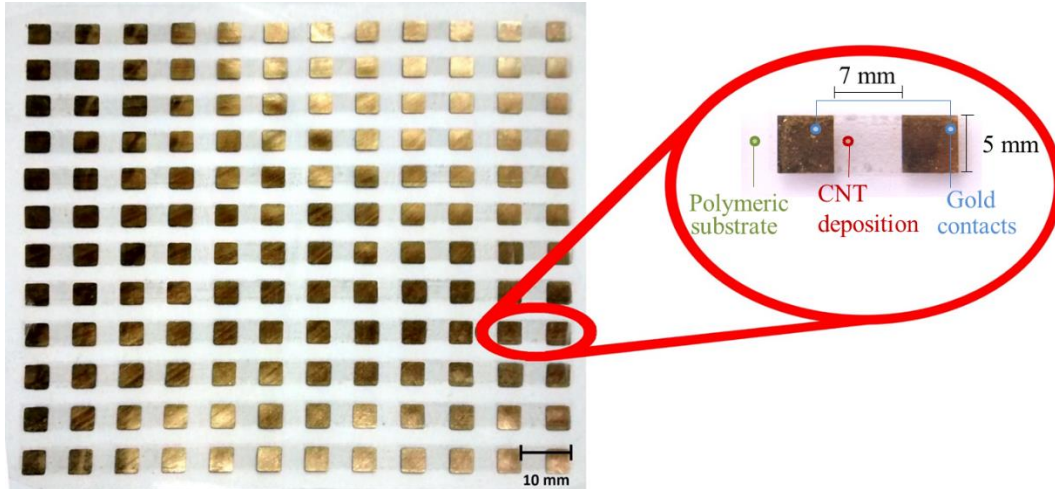


Figure II.3.2 The result of a batch fabrication of 72 sensors on the same polymeric substrate. In the circle, a schematic indicating the different parts of which the device is composed.

II.3.2 Physical and electrical characterizations

The devices are observed via optical and scanning electron microscopy SEM (Hitachi S 4800). The deposition thickness is measured via profilometry (Dektak 150). For resistance measurements, electrical contacting is achieved by gluing thin copper wires to the gold electrodes with silver paste. The resistance is measured in a 4-probe configuration to limit the impact of contact resistances: a Keithley 2612 source measurement unit imposes a constant, continuous current in the μA range

(from 4 to 7 μA) while a National Instrument NI9212 acquisition card measures the output voltage at a frequency of 6.7 Hz. All electrical characterizations are performed within aluminum shielding serving as Faraday cage providing electromagnetic shielding.

II.3.2.1 Strain sensing

To characterize the devices as strain gauges, variations in resistance are measured while applying longitudinal deformations to the substrate (deformations applied along the main axis, see Figure II.3.1a). Deformations are applied by gluing the two opposite sides of a substrate to two clamps mounted on force-controlled motors (Figure II.3.3). Forces up to 8N are applied. The force is measured using Althen ALF328 10N load cells. A CCD camera is used to determine the resulting deformation of the substrate: the displacement of surface patterns is tracked during deformation and then converted into Eulerian strain. Strain levels reach up to 2500 $\mu\epsilon$.

Devices are characterized either separately or by series of 4 sensors on the same substrate. During characterization of the piezoresistive response, the temperature is not controlled but is monitored by a thermocouple.

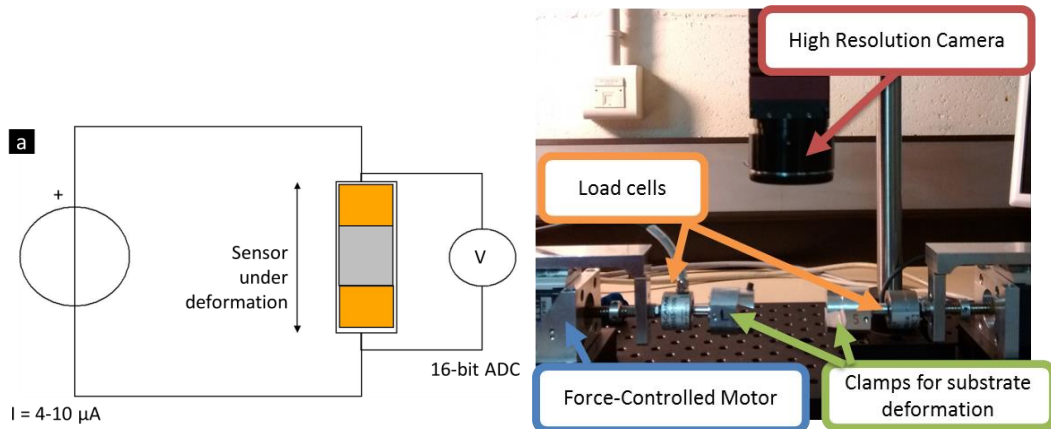


Figure II.3.3 a) Schematic of the electric circuit used to characterize the electrical response of the sensor. b) Image of the mechanical bench used to impose a deformation on the substrate.

II.3.2.2 Temperature sensitivity

The temperature sensitivity of the resistance is also measured. The devices are placed on a hot plate controlled by the Thermoelectric Temperature Controller LFI 3751 by Wavelength Electronics. The resistance is measured with a Keithley S4200 using a 4-probe configuration. During temperature characterization, the samples are positioned in a shielded environment under nitrogen flow to ensure that relative humidity remains constant at 0.8 % during the duration of the measurement.

II.3.2.3 pH sensing

The device is glued to a rigid glass substrate that prevents any mechanical deformation of the device (see Figure II.3.4). Two long strips of copper scotch

tape are used to deport the contacts. Silver ink is used to ensure the connection between the gold electrodes of the device and the two copper strips. Two wires are soldered to the copper strips to connect the device to an ohmmeter in a 2-wire configuration (a twisted-pair cable is used to decrease noise). In particular, we apply a current and we measure the voltage generated across the device.

A layer of epoxy resin (SU8) to ensure electrical isolation covers all the contact area; the only section left uncovered is the CNT network. The device is then plunged in a buffer solution with stable pH (see Figure II.3.5). We study the response of the device for different pH. The layer of SU8 deposited on the contacts isolates them from the solution, thus we attribute the observed changes solely to the modifications inside the CNT network.

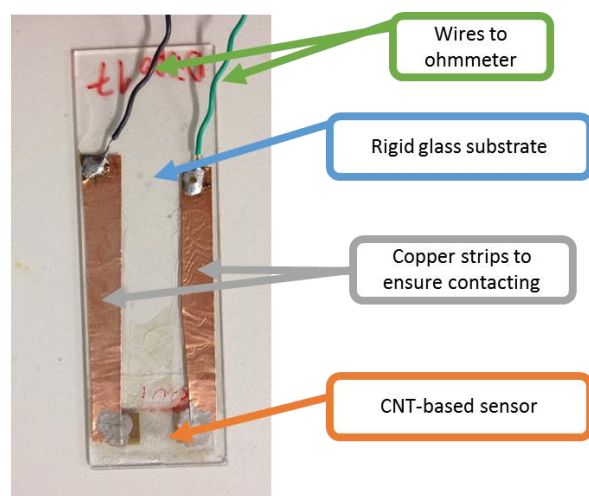


Figure II.3.4 CNT-based sensor used for pH sensing. The sensor is glued to a rigid glass substrate. Electrical contacting is ensured by two copper strips. The contacts are covered by insulating epoxy resin (SU8) to avoid contact with the solution.

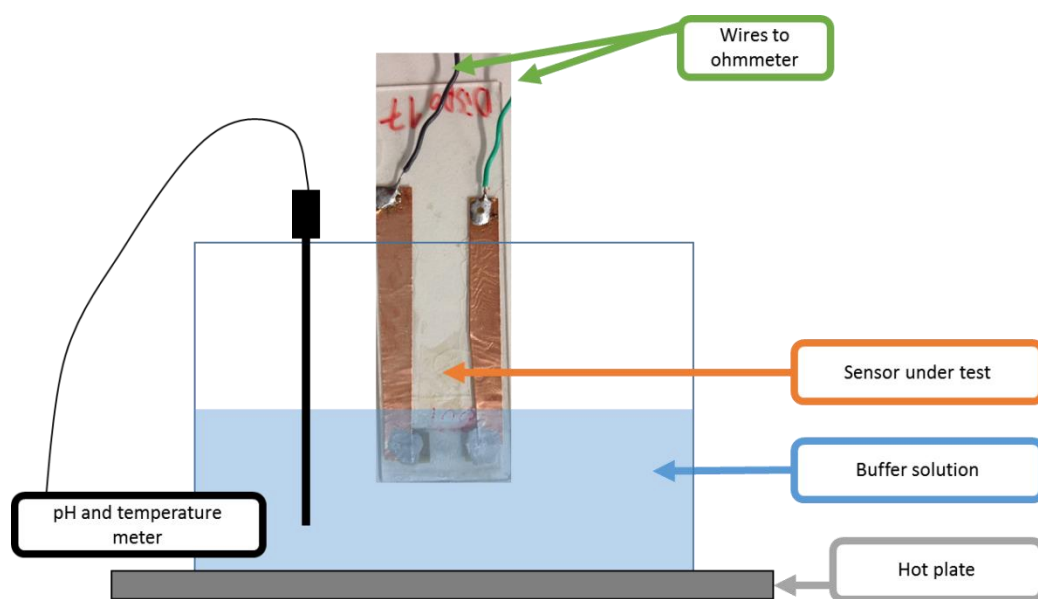


Figure II.3.5 Schematic of the setup used for the tests.

II.3.2.4 Humidity sensing

To characterize this phenomenon, we used a temperature-controlled humidity chamber. The device were dried for 20 minutes under nitrogen flow and kept at constant temperature; the resistance was measured in 4-wire configuration. We tested the devices for increasing Relative Humidity (RH).

II.4 CHARACTERIZATION OF DEPOSITION

II.4.1 Morphology of the carbon nanotube network

Since the device is fabricated by the superposition of several layers, we study the morphology of a single deposited layer and the morphology of the final device.

II.4.1.1 Single deposited layer

SEM images of a single layer deposition (Figure II.4.1a) show that CNTs are spread randomly on the surface, with a surface density of approximately 240 CNTs/ μm^2 (manual counting). Micrometric holes can still be observed on SEM images (Figure II.4.2a). These holes are attributed to loss of material during rinsing.

This image was processed with ImageJ (Windows version 1.48) software to identify the surface coverage of CNTs as follows:

- the option Noise-Dispeckle was used to decrease noise in the image,
- the contrast of the image was increased to better separate the uniform background from the CNTs,
- the image was converted into binary applying a threshold; the level was set to 165/255 (bit depth of 8-bit),
- a second Noise-Dispeckle filter was applied to eliminate those pixels in the background that were interpreted as CNTs during the binary conversion.

The resulting image is shown in Figure II.4.1b. Finally, the surface coverage was calculated as:

$$coverage = \frac{\text{Number of white pixels}}{\text{Total number of pixels}}$$

Two images are evaluated and the calculated coverage is, respectively, 40 % and 46 %. The average of the measurement is 43 %.

In this evaluation, we assume that the SEM imaging renders the true CNT diameter and there are no effects of diffraction or shadowing.

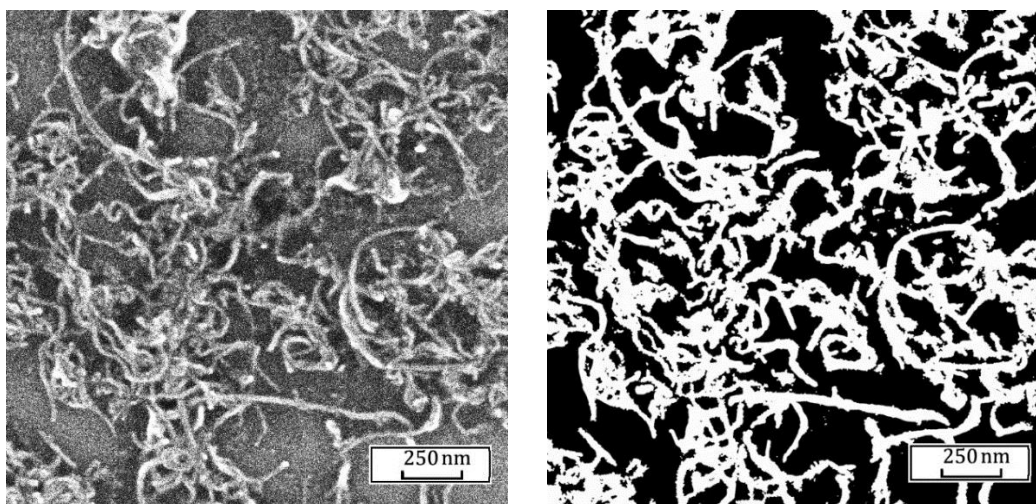


Figure II.4.1 SEM image of 1-layer deposition. Micrometric holes are observed in the layer; they are attributed to loss of matter during rinsing. a) SEM image b) Image processed with ImageJ to determine surface coverage.

II.4.1.2 Multiple deposited layers

When increasing the number of layers, the homogeneity of the deposition improves and the surface coverage increases. At 20 depositions, the surface is entirely covered (Figure II.4.2b and c).

Up to 20 layers, the thickness of the deposition increases averagely by 54 nm for each additional layer, as estimated by a linear fit of the data (Figure II.4.2d). The thickness reaches 1100 nm for a 20-layer deposition. As expected from the SEM images, the film surface is very rough. The roughness increases with the number of layers, from 110 nm for 3 layers up to 720 nm for 20 layers. The substrate itself contributes to the overall roughness by only 90 nm. Despite the fact that the absolute value of the roughness increases, the relative roughness (calculated as the ratio of roughness to thickness) decreases from 0.85 to 0.66 between 3 and 20 layers (Figure II.4.2e), suggesting that the deposition surface becomes slightly more homogeneous when the number of layers is increased.

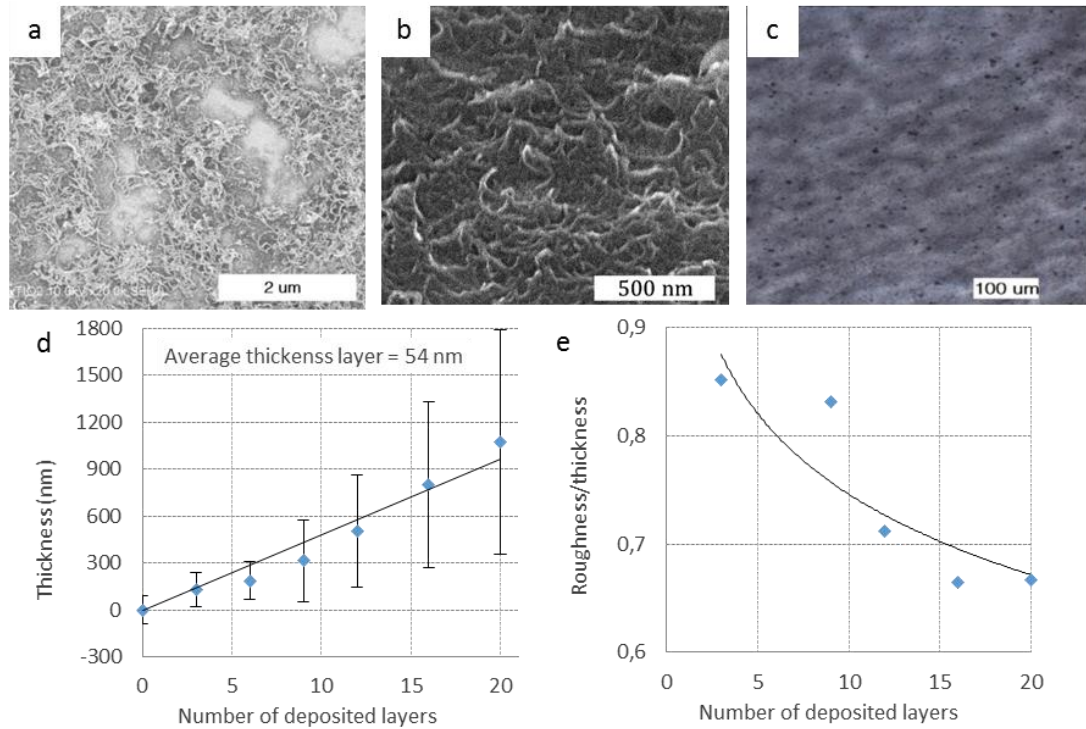


Figure II.4.2 a) SEM image of 1-layer deposition. Micrometric holes are observed in the layer; they are attributed to loss of matter during rinsing. b) SEM image of 20-layer deposition. A uniform coverage can be observed. c) Optical microscopy image of a 20-layer deposition, showing homogeneity and uniformity at a micro scale. d) Thickness of the deposition with respect to number of layers. The rise is roughly linear with a slope of 54 nm by layer. The error bars represent the surface roughness. e) The relative roughness (calculated as the ratio of roughness to thickness) with respect to number of layers. The decreases from 0.85 to 0.66 suggests that the deposition surface becomes slightly more homogeneous when the number of layers is increased.

II.4.2 Device resistance

A single layer has a resistance in the G Ω range, too high for sensing applications. As expected, the resistance decreases as the number of layers increases, in accordance with the literature on CNTs percolated networks (Slobodian, et al., 2011). It reaches the 1 M Ω range at 15 layers, the 150 k Ω range at 20 layers and the 100 k Ω range at 30 layers (Figure II.4.3). The lowest resistance reached is 104 k Ω (87 k Ω /sq) for a 30-layer deposition. This range of magnitude of resistance, though quite high compared to CNN-based inkjet-printed flexible transparent conducting layers (Kwon, et al., 2013), is fully compatible with sensing applications.

The decrease of resistance as a function of the thickness is much faster than for homogeneous thin films (see for instance Fuchs model (Cottey, 1938)). It is attributed to a combination of two effects (Hoffmann & Vancea, 1981): the high roughness-to-thickness ratio of the film (usually accounted for using Namba method) and the densification of the percolating network.

From the 20th layer, the resistance decrease is much lower. Since the roughness-to-thickness ratio of the film decreases (as observed in Figure II.4.2e), we believe that

the CNN is dense and consequently the total resistance is mainly dominated by the geometry of the device ($R = \rho \frac{L}{S}$), the resistance of the single CNTs and the contact resistance between them.

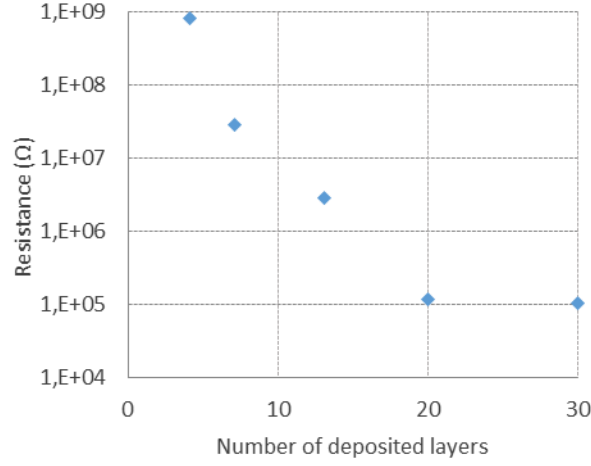


Figure II.4.3 Resistance of the deposition with respect to number of layers.

II.4.3 Reproducibility of the fabrication process

The standard deviations of the resistance of the devices fabricated in different batches ranges from 8.4 % to 18 %. In the rest of the thesis, we discuss a 20-layer, 8-sensor batch with average resistance 156 kΩ and 15 % (23 kΩ) standard deviation.

The result obtained on the standard deviation, measure of the reproducibility of the fabrication process, is comparable with the 7.3 % standard deviation over 3 devices reported in (Benchirouf, et al., 2012).

In order to improve the current result, we could work on two main parameters of fabrication. On the one hand, the rinsing process is, currently, a manual agitation of the substrate in acetone and methanol. As shown in Appendix I, the rinsing process strongly influences the resistance of the network. Consequently, an automatic rinsing process performed by a robotic arm would guarantee a much more reproducible rinsing process and, in turn, a lower dispersion of the resistive values.

Moreover, the substrate currently used in the fabrication is 0.125 mm thick. During the deposition and the rinsing process, some local deformations are introduced on the substrate. These morphological changes introduce a change in resistance of the devices. A thicker substrate could limit this phenomenon, thus reducing the dispersion of the resistances of the final devices.

II.5 PIEZORESISTIVITY OF THE DEVICE - CHARACTERIZATION

The sensor was tested for its piezoresistivity and its ability to sense micrometric deformations. In this chapter, we present this property of the device. We report on experimental data on the response of the sensor under different tests.

II.5.1 Piezoresistive behaviour for large deformations

The piezoresistive behaviour of the device was tested under a force as high as 8 N and 4000 $\mu\epsilon$ (1 $\mu\epsilon$ strain corresponds to an extension dL of a device with length L for which $dL=10^{-6}L$). The sample was tested for 5 cycles of elongation and relaxation of the substrate over a period of 30 minutes. The response is nonlinear and irreversible (Figure II.5.1). The nonlinearity of the response for large deformations is in accordance with the literature (Hu, et al., 2010) and the irreversibility can probably be attributed both to the plastic deformation of the substrate and irreversible changes in the carbon nanotube network.

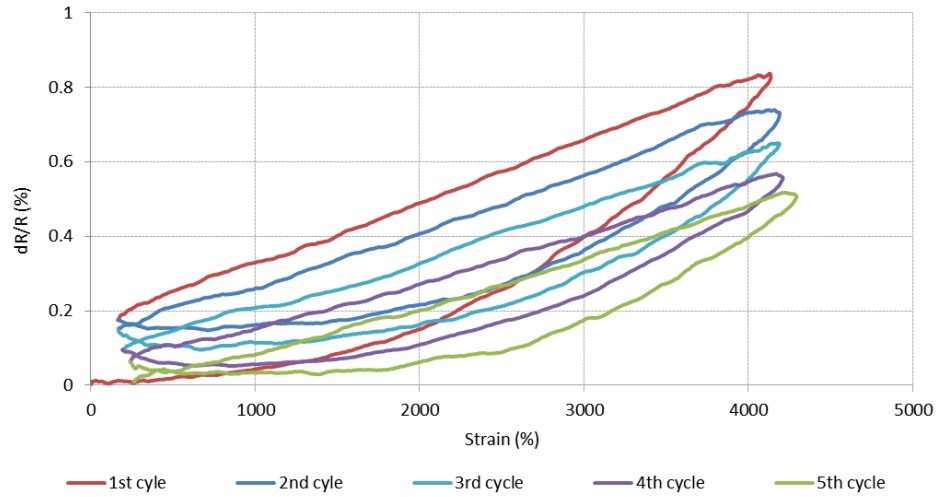


Figure II.5.1 Piezoresistive response to cyclical large deformations.

II.5.1.1 Piezoresistivity of electrodes

In order to exclude the possibility that the piezoresistivity is due to the gold electrodes, their piezoresistivity is tested; the variation of the electrode resistance is lower than 10 Ω up to 4000 $\mu\epsilon$. The observed global resistance change of the devices is more than 70 times bigger for a comparable deformation (ΔR for a 4000 $\mu\epsilon$ deformation is over 700 Ω). Consequently, we will attribute the following piezoresistive behaviour to the CNT network.

II.5.2 Linearity and repeatability of the piezoresistive behaviour for small deformations

The piezoresistive response for large deformations is roughly quadratic, in accordance with (Baeza, et al., 2013). It is possible to identify a linear regime for small deformations (Figure II.5.2). All devices feature a linear behaviour in the

small strain regime. The linear regime reaches up to 700 $\mu\epsilon$ for 75 % of the devices, with extremes as low as 400 $\mu\epsilon$ and as high as 1000 $\mu\epsilon$.

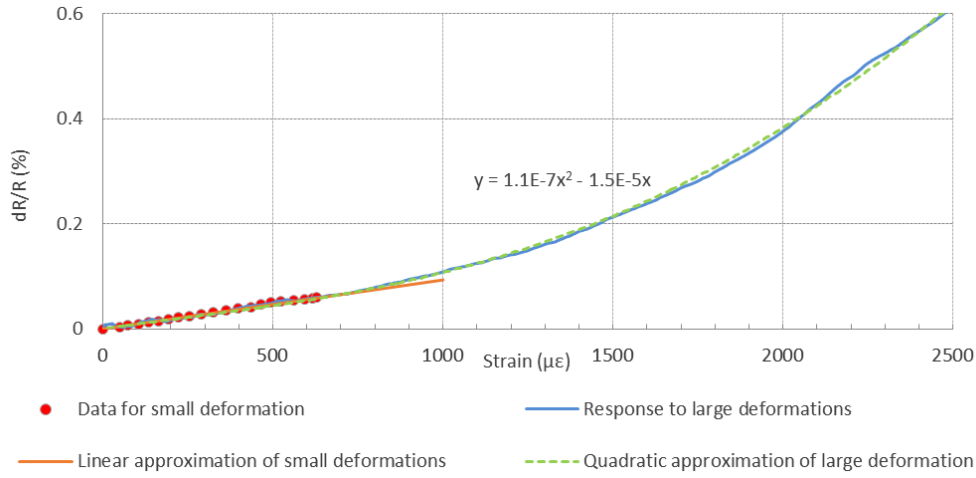


Figure II.5.2 Linear range of the piezoresistive behaviour. The linear regime reaches up to 700 $\mu\epsilon$ for 75 % of the devices, with extremes as low as 400 $\mu\epsilon$ and as high as 1000 $\mu\epsilon$.

In the linear range, it is possible to calculate the gauge factor (defined as $\frac{dR}{R} / \frac{dL}{L} = \frac{dR}{R} / \epsilon$) in order to compare the device under study with the commercial and scientific literature in the domain.

The GF is found to be 0.90 ± 0.14 for an 8-device batch. This GF value is comparable to the performance of commercial strain gauges available on the market (Li, et al., 2014) (Engineering, s.d.) (Ltd, 2011) as well as comparable to the only reported GF (GF ~ 3) for printed CNT strain gauge (Kim, et al., 2012) and the results reported on non-printed CNT networks well above percolation threshold (GF ranging from 1.45 to 7).

Much higher values (GF ranging from 15 to 60) have been reported for CNT-based devices operating closer to the percolation threshold (Zhang, et al., 2013) (Srivastava, et al., 2011) (Li, et al., 2014). Operating close to percolation threshold is beneficial for having higher sensitivity, but it has a detrimental impact on the device-to-device reproducibility (Li, et al., 2014). In fact, the fabrication process is less reproducible and, secondly, the variability of sensitivity across devices is very high. Both drawbacks are solid arguments against the development of such technologies for commercialization because the cost associated to the characterization of each individual sensor would be too high.

The low variability of the sensitivity (GF) across our devices is a key point to justify the interest in the inkjet printing of CNTs for the fabrication of innovative strain gauges (Siegel, et al., 2007) (Markman, et al., 2008).

The variability of the gauge factor of our sensors, evaluated as the ratio between the standard deviation and the mean, is 16 %. This is the first quantitative evaluation of the variability in sensitivity for batch-produced CNT-based flexible sensors.

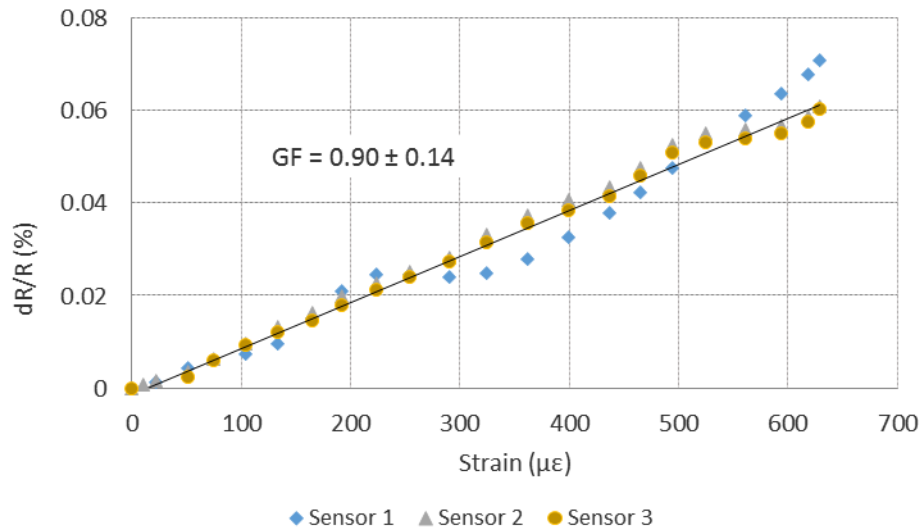


Figure II.5.3 Repeatability in the linear regime.

II.5.3 Response time

We assessed the device response time, defined here as the time to reach 95 % of the expected value once the target strain is reached (Figure II.5.4a and b). The strain is increased linearly over 5 s to reach its target (see Figure II.5.4a). The response time was found to be 3.6 s for a 500 $\mu\epsilon$ strain (within the linear regime of the device). This suggests that the devices should preferably be used for static or quasi-static applications (frequencies well below 0.3 Hz/period well over 3.6 s).

Outside the linear range, the response time is much higher. For a 1600 $\mu\epsilon$ strain, the response time is as high as 19 s; it appears that from about 1200 $\mu\epsilon$, the device cannot follow the increase in strain, thus suggesting the onset of plastic effects in the substrate.

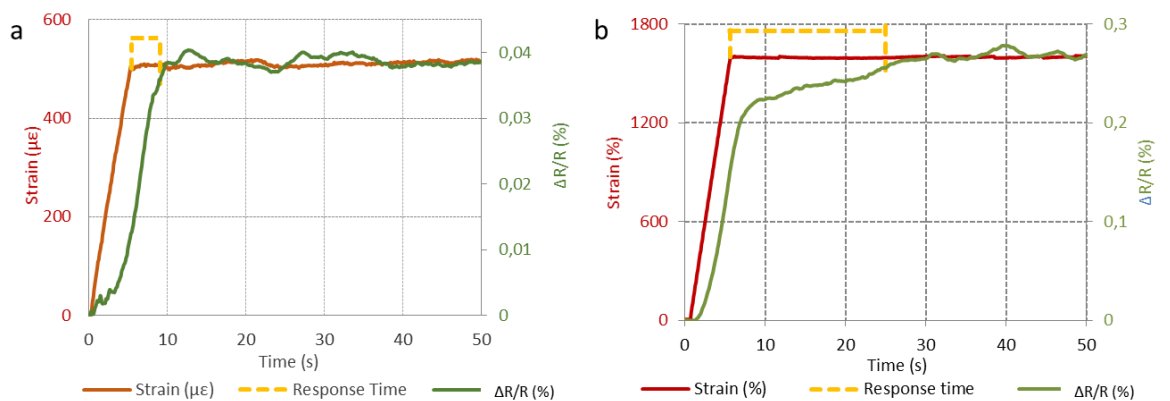


Figure II.5.4 Response times of the devices to a) under small strains and b) under large strains.

II.5.4 Quasi-static cyclability and hysteresis-free operation in quasi-static mode

We evaluated the quasi-static cyclability of the devices in the linear regime. The devices are submitted to cyclic loadings (20 cycles over 3 hours) in the linear regime (800 $\mu\epsilon$) with 9 minutes periodicity (2 mHz, well below the frequency limit defined using the response time). The device response is acquired at 6.7 Hz (3600 measurements per period). As expected in quasi-static mode, no phase shift is observed between strain and resistance curves (Figure II.5.6). The discrepancy between the gauge factor measured during loading and the one measured during unloading is only 2.7 %, which underlines the high reversibility of the devices compared to the state of the art (Zhang, et al., 2013) (Srivastava, et al., 2011). The standard deviation observed on the maximum resistance values reaches only 4.7 % over 20 cycles, which can be easily explained by the temperature sensitivity of the device (0.5 °C variation in temperature would suffice, which can easily happen even in temperature-controlled environment).

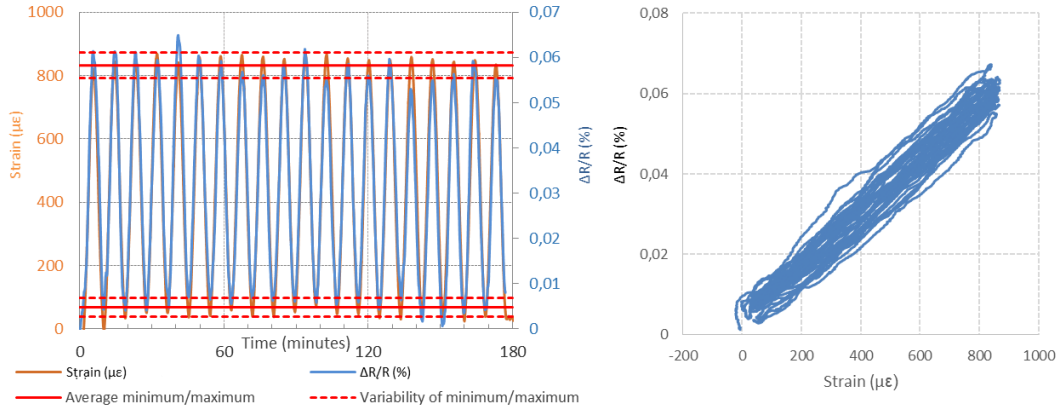


Figure II.5.5 Quasi static response of the devices to cyclic loadings (20 cycles).

For longer tests, the devices show an upward drift of the plot in Figure II.5.6. This phenomenon may be caused by a variety of factors, including plastic deformation of the substrate and irreversible reorganization of the micrometric structure of the CNT network. Additional tests are needed to understand and correct or compensate this phenomenon.

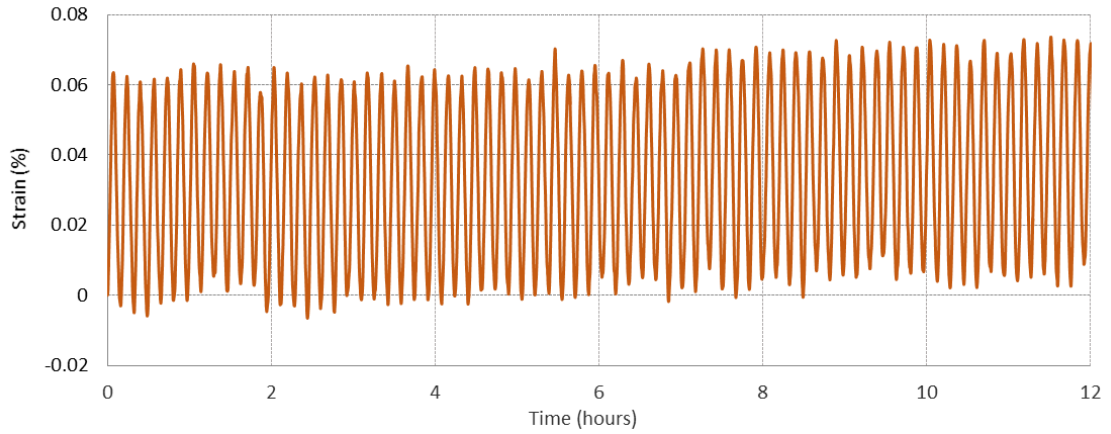


Figure II.5.6 Response of the devices to extensive cyclic loadings (72 cycles).

II.5.5 Temperature compensation

Temperature is known to strongly influence CNT conductivity (Dehghani, et al., 2012) and polymer mechanical response (Fisher | Moore, 1999). Thus, we studied the devices dependence on temperature (Figure II.5.7). The results show that the resistance decreases linearly with temperature, in accordance with other studies (Bao, et al., 2012) (Dehghani, et al., 2012). The temperature sensitivity coefficient, defined as the slope of the dR/R versus temperature curve, is equal to $-1.0 \times 10^{-3} \text{ } ^\circ\text{C}^{-1}$. This coefficient is comparable to the $-4 \times 10^{-3} \text{ } ^\circ\text{C}^{-1}$ published in (Dehghani, et al., 2012) for CNT devices fabricated on silicon. Interestingly, the variability on the temperature sensitivity is as low as 8 % over seven devices, significantly lower than the resistance and piezoresistivity variability. This is very promising either to use the device as temperature sensor, or to implement temperature compensation strategies for strain gauges applications.

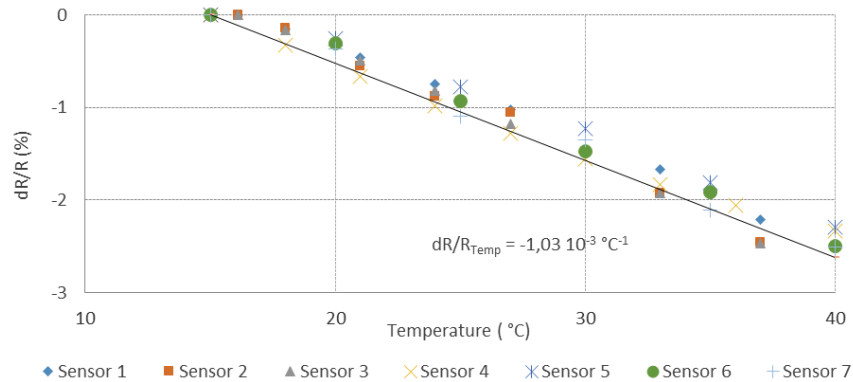


Figure II.5.7 Dependence of resistivity of the devices on temperature.

II.5.6 Relevance of the device for crack detection in concrete

In the characterization presented here, the CNT strain gauge is linear up to a deformation of $600 \text{ } \mu\epsilon$. This deformation is equivalent to an elongation of the substrate of $10.2 \text{ } \mu\text{m}$. The size of concrete micro-cracks responsible for chloride

permeability have an average size of 10 μm (Shi & Shi, 2008) (Zheng, et al., 2009).

The repeatability of the measurement over multiple cycles of loading and unloading suggests the possibility of withstand the cyclic deformations introduced on a structure by the temperature cycles (seasonal and daily fluctuations), basic requirement for the longevity of the sensor in a concrete structure.

In addition, the possibility of correcting the readings for temperature changes is another essential requirement for the employability of this solution in concrete structures.

All these results lead us to believe that such sensor is adapted for the detection of micrometric deformation inside concrete.

II.5.7 Conclusion

We provided the first study on performances and variability of batch-fabricated strain gauges based on CNT network directly inkjet-printed on soft polymer substrate. The variability of the resistance of these devices was as low as 14 %. The reported sensitivities to strain ($GF=0.9$) and temperature are comparable to previous literature results on batch-fabricated CNT network-based strain gauges. Additionally, we provide the first assessment of the variability of the gauge factor of CNT-based strain gauges, evaluated at 16 %. These results support that inkjet printing is a highly promising technique for batch fabrication of reproducible CNT-based strain gauges.

Future work on the device will focus on four main directions. Firstly, different shapes and size should be considered. We recently developed a mask to fabricate different sensors and investigate the dependence of size and aim at reducing the size of the final device.

Secondly, the temperature characterization set-up should be modified to characterize a wider range of temperatures.

Thirdly, a different type of CNT should be tested with the aim of decreasing the nominal resistance of the sensor. The average value reported (156 $\text{k}\Omega$) is a considerably high value compared to the commercial offer of strain gauges (commercial strain gauge can usually be found in the range 100-300 Ω). Decreasing the resistance value would increase the signal to noise ratio during electrical measurements.

Finally, different substrates could be investigated in order to increase the linearity range of the device. Among others, a very resistant polymer fully compatible with the concrete environment would be Kapton. A wider range on linearity would allow us to target a wider range of applications where higher deformations are involved.

II.6 PIEZORESISTIVITY OF THE DEVICE – MODEL AND INTERPRETATION

We propose a numerical model of the CNT network to better interpret the piezoresistive behaviour of the device.

II.6.1 State of the art

According to the literature, three types of behaviours are expected to contribute to a piezoresistive characteristic of a carbon nanotube network: the piezoresistive behaviour of isolated CNT (Hierold, et al., 2007) (Chang, et al., 2008) (Grow, et al., 2005) (Maune & Bockrath, 2006), the irreversible reorganization of the CNT network as a consequence of mechanical strain (Hecht, et al., 2006) and the reversible change of intertube distance in response to strain (Hu, et al., 2010) (Lin, et al., 2010) (Stadermann, et al., 2004).

It is unlikely that the obtained results can be associated with the piezoresistive behaviour of isolated CNTs since the sensitivity reported for devices exploiting this mechanism is usually much higher (Grow, et al., 2005) (Maune & Bockrath, 2006).

It is equally unlikely that the irreversible reorganization of the CNTs is responsible for the overall observed behaviour. One may concede that some initial irreversible reorganization of the CNTs occurs, as observed in Figure II.5.6 where the gage factor does not return to 0 after the first cycle of loading. However this effect is minimal and vanishes after the first cycle, then leaving place to a completely reversible piezoresistive effect in the observed range of deformation over multiple loading cycles.

Hence, we attribute the observed piezoresistive behaviour to the change of intertube distance in response to strain. Additional studies conducted in the team (Lavric, et al., 2015) show that for the concentration of CNTs used in the simulation, the conduction between CNTs due to tunnel effect is negligible respect to the conduction between CNTs actually in contact because we are far above percolation.

Consequently, we believe that the piezoresistive effect can be explained by a reduction of the number of intertube contacts between adjacent CNT. In fact, the strain imposed on the system reduces the number of intertube contacts between adjacent CNT, thus decreasing the number of possible conduction paths. This phenomenon is reversible and the tubes go back to their original positions when the strain is released (past the initial network small irreversible reorganization observed in the first cycle).

(Kirkpatrick, 1973), (Geiger & E., 1982) and (Balberg & Binenbaum, 1985) demonstrated a linear relationship between the total number of contacts between conductive fillers in a nonconductive medium and the resistance of the resulting composite (for composite above percolation threshold). They did so by modelling the conductive filler as equipotential conductors and the contacts between adjacent

fillers as unit resistor. This approximation can hold for the presented CNT network because of the known high conductivity of MWCNTs.

If the total number of contacts and the resistance are linked by a linear law, the piezoresistive effect of the CNT network is equal to the change in number of contacts between adjacent CNTs as expressed by the following formula:

$$\text{if } R = \alpha N_c \quad \text{then} \quad \frac{dR}{R} = \frac{dN_c}{N_c}$$

Consequently, the piezoresistive effect can be analysed by looking at the evolution of the total number of contacts between CNT for different values of strain.

In the current version of the model, we evaluate the relationship of the number of contacts in response to strain. In future development of the model, we will implement the evaluation of the resistance, based on an iterative procedure (see Figure II.6.1):

- above percolation threshold, it is possible to find at least one conductive path intersecting opposite sides of the modelled composite (the very definition of the percolation threshold),
- it is possible to identify the multiple path parallel to contributing to conduction. Such model can be represented and solved with the theory of resistor networks.

The previous models of percolated networks are based either on 2D or 3D representations of the conductive fillers (Kumar, et al., 2005) (Berhan & Sastry, 2007) (Lin, et al., 2010) (Hu, et al., 2010). Our approach is the superposition of several 2D planes to better represent our fabrication process and our SEM observations.

Two different models were developed. In the first one, CNTs are modelled as straight rigid sticks. With the second one, we investigate the role of the waviness of CNTs on the sensitivity of the device.

II.6.1 Outline of the simulation

In the model, CNTs are treated as linear “soft-core” objects (Berhan & Sastry, 2007), allowing penetration between adjacent CNTs.

CNTs are defined as rigid tubes dispersed in a plane with an iterative function that allows to randomize their orientation and position in the plane, similarly to (Balberg & Binenbaum, 1985).

The mechanical deformation of the substrate is simulated by shifting the centre of CNTs along the x-axis (see Figure II.6.2). The shift is a linear gradient from 0 to max displacement at the end of the cell corresponding to the nominal applied strain. CNTs are treated as solid objects that do not deform during the shifting process. After the deformation, some of the contacts between adjacent CNTs are lost, thus reducing the total number of contacts.

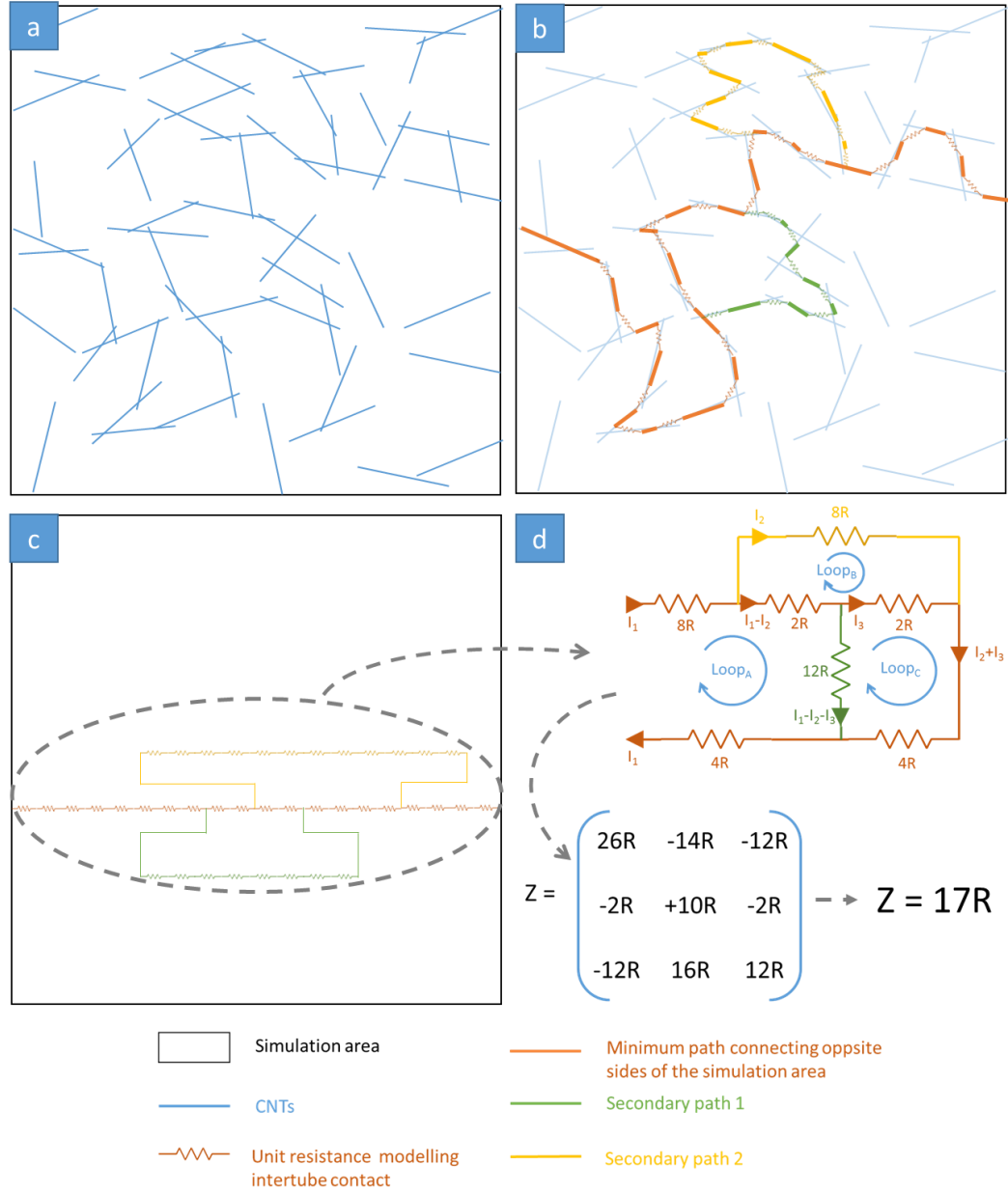


Figure II.6.1 Calculation of the resistance in a percolated network of conductive filler in an insulating medium. The fillers (CNTs in our study) are modelled as equipotential conductors and the contacts between adjacent CNTs are modelled as resistances. To determine the total resistance of a percolated network (a), the paths contributing to conduction between opposite sides should be determined (b). From this information it is possible to build the conduction diagram (c). From the conduction diagram, it is possible to apply the Kirchhoff laws and extract the matrix of impedances for the considered loops and, eventually, the impedance of the total conduction path.

Considering the relatively high Poisson's ratio of the ETFE (0.43), we simulate the Poisson effect as well (see Figure II.6.2). The shift is a linear contraction gradient from 0 to max displacement at the end of the cell corresponding to the Poisson's reduction in width. While the CNTs are shifted horizontally to simulate the strain applied, they are shifted on the vertical direction to simulate the Poisson effect. With this movement (we remind that that the shape of the CNT is not altered

during the shift), some new contacts between CNTs are created, thus compensating in part the reduction of number of contacts caused by the elongation.

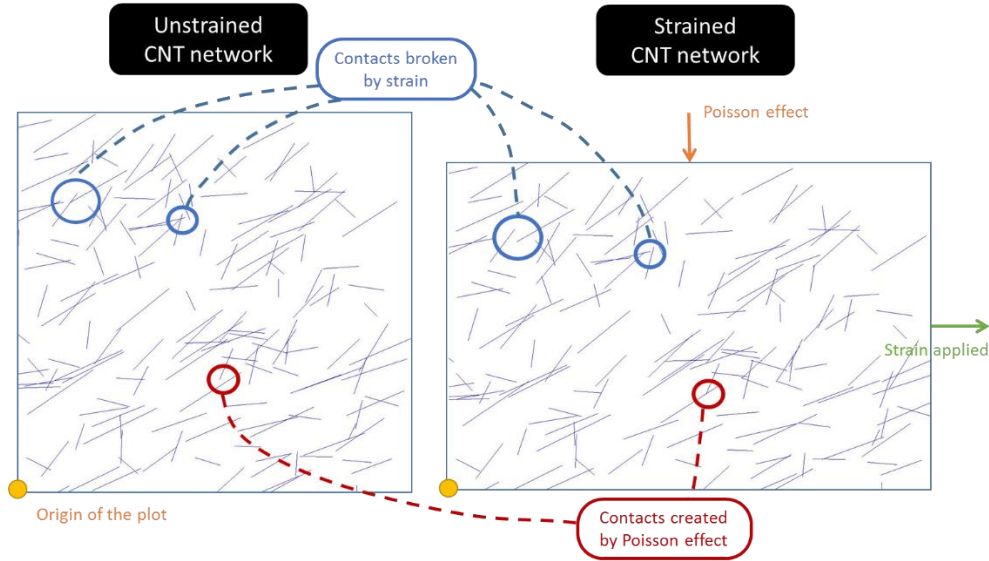


Figure II.6.2 Schematic of the CNT network under elongation. On the left, the simulated network unstretched. On the right, the simulated network elongated along the horizontal direction and consequently shrunk in the vertical direction due to the Poisson's effect. We want to emphasize that the density of the CNTs in this image is not representative of the real density used during the simulations. The density has been lowered for clarity of the picture.

We study the evolution of the total number of contacts (N_c) between adjacent CNTs in a same plane and between CNTs belonging to contiguous layers. We consider that the electrical contact between two adjacent CNTs is functional only if there is a physical contact.

II.6.2 CNTs modelled as straight rigid sticks

This model is built to study an elementary cell of square shape, whose size is 2000 nm x 2000 nm. This size was selected to ensure that the average length of a CNT is much smaller than the size of the cell to decrease the effects of borders in the simulation.

II.6.2.1 Comparison between the morphology observed experimentally and the morphology generated by the linear model

CNTs are defined as rigid tubes dispersed in a plane with an iterative function that allows to randomize their orientation and position in the plane. The CNT length is normally distributed around 300 nm with standard deviation 50 nm (values extracted from the SEM images presented in II.4.1); the radius of CNTs is set to 12 nm according to the datasheet (Arkema, 2008). 20 parallel planes of randomly distributed CNTs are stacked on top of each other in order to obtain a structure similar to the experimental device.

Following the procedure described in II.6.1 to organize CNTs within space, we obtained the structure shown in Figure II.6.3. We can see that the distribution of the modelled CNTs on the single plane reflects the patchy distribution of the real CNTs observed in the SEM Figure II.4.1, with highly dense areas next to almost empty areas. The percolation of the network is achieved by superposition of several layers.

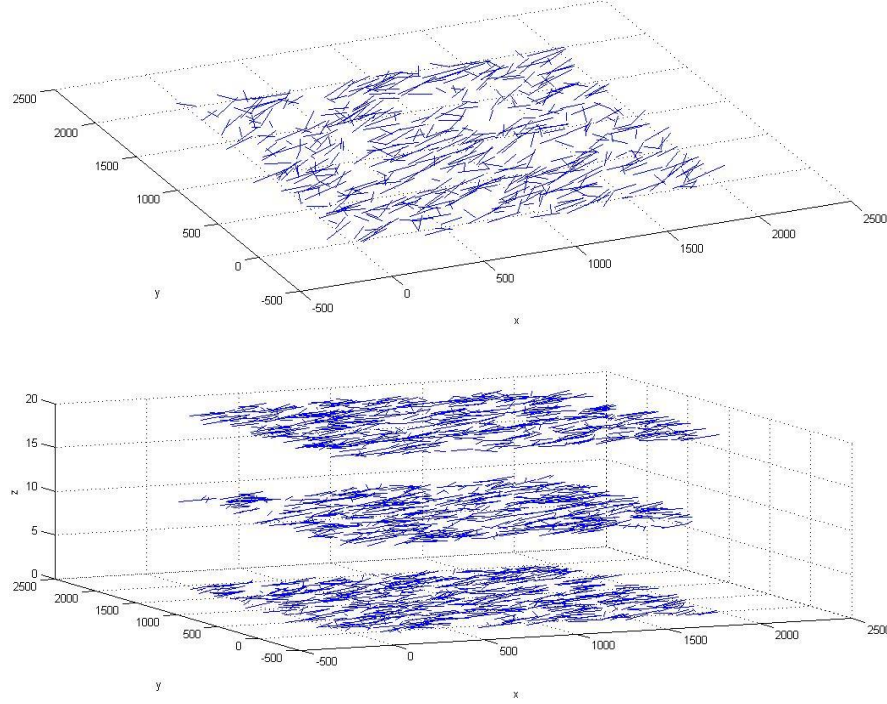


Figure II.6.3 Above, the image of a single deposited layer. CNTs are treated as rigid sticks whose length is normally distributed around an average length of 300 nm (standard deviation 50 nm). Below, a representation of the superposition of 3 layers of CNTs. In this image, the different layers are represented further apart to facilitate the comprehension of the image. During simulations, contiguous layers are in contact.

II.6.2.2 Results of the simulation

Firstly, **the percolation threshold is identified**. By sweeping the density from 1 CNT/ μm^2 to 300 CNT/ μm^2 , we can see that the number of contacts (N_c) rises significantly after the density of 100 CNT/ μm^2 is reached (Figure II.6.4).

In several papers reporting on CNT networks (Slobodian, et al., 2011) (Lin, et al., 2010), we observe a significant drop in the resistance of the network after the percolation threshold is reached. This phenomenon is caused by a sudden increase in the number of connection paths created.

With this analogy in mind, we define the percolation threshold for this model as the density at which the number of contacts starts increasing significantly. From the dashed-line approximation shown in Figure II.6.4, we identify this threshold at 120 CNT/ μm^2 .

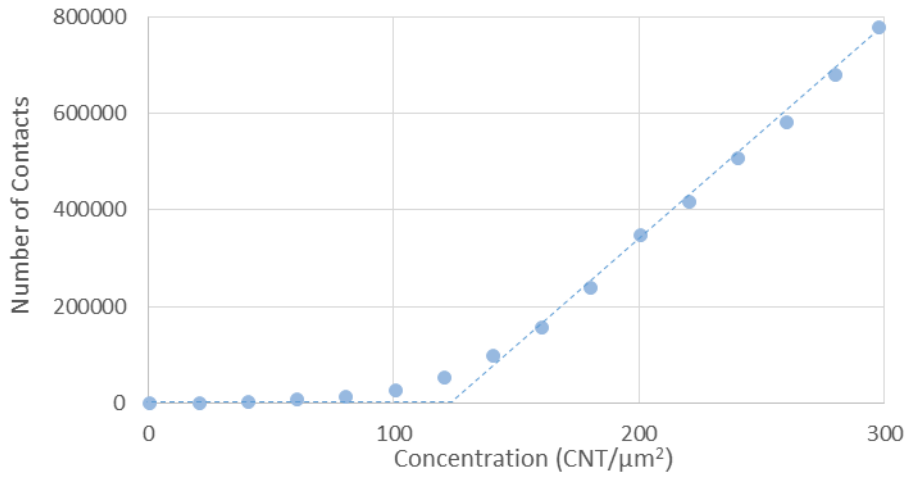


Figure II.6.4 Number of contacts between CNTs evaluated in the model as a function of the density of CNTs imposed. The dashed line represents the approximation taken to identify the percolation threshold.

Secondly, **the piezoresistive effect is studied**. After application of a deformation and consequent shift of CNTs, some of the contacts between adjacent CNTs are lost, causing a decrease in the total number of contacts.

As reported in Figure II.6.4, the rate of decrease in number of contacts as a function of strain is highly dependent on the density of CNTs in the plane. In fact, for a density of $60 \text{ CNT}/\mu\text{m}^2$ (half of the percolation threshold identified earlier), the rate of decrease in number of contacts with applied strain is relatively high. On the other hand, when imposing a density of $240 \text{ CNT}/\mu\text{m}^2$, (double of the percolation threshold identified earlier and equal to the density observed experimentally), the rate of decrease in number of contacts with applied strain is much lower. We define the sensitivity of the variation of number of contacts (dN_c/N_c) to strain as the coefficient of the best-fitting line approximating the data.

Moreover, in the first case, the results obtained are not repeatable; in fact, launching the same code, with the same parameters of simulation, the results vary vastly between two successive iterations of the code (see series 60_X of Figure II.6.5). On the other hand, when imposing a density of $240 \text{ CNT}/\mu\text{m}^2$, the results are more repeatable (see series 240_X of Figure II.6.5). We define the variability of the result as the standard deviation of the distribution of the sensitivity when the same simulation is repeated several times.

Figure II.6.6 shows how the sensitivity and its variability are affected by the density of CNTs imposed. 10 simulations are performed for density of CNTs ranging from $20 \text{ CNT}/\mu\text{m}^2$ to $300 \text{ CNT}/\mu\text{m}^2$. The average sensitivity for each CNT density is represented as a blue point in the plot. The variability (standard deviation of the 10 simulations performed for each value of density) is expressed by the vertical error bars.

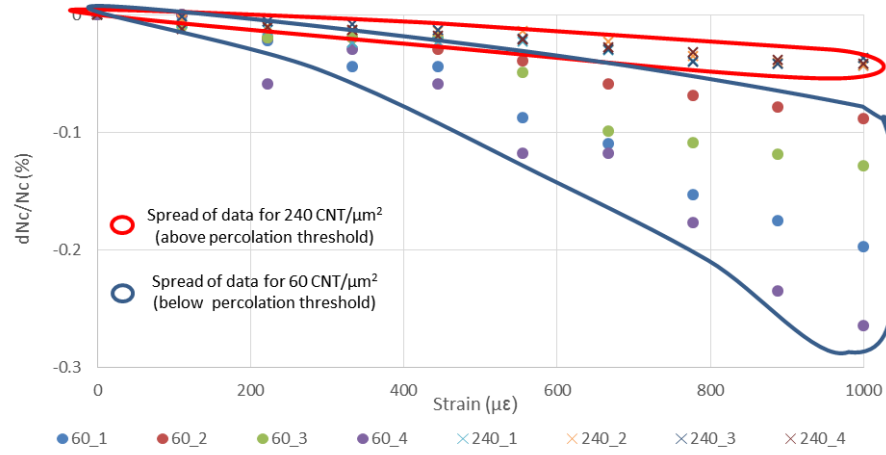


Figure II.6.5 Simulation results showing the relationship between variation of number of contacts (dN_c/N_c) and applied strain for different densities of CNTs in the plane. For a density below the percolation threshold ($60 \text{ CNT}/\mu\text{m}^2$), the results vary vastly between different iterations of the code. For a density higher than the percolation threshold ($240 \text{ CNT}/\mu\text{m}^2$), the results are much more repeatable, with the drawback of a smaller sensitivity. It is worth noticing that the linear behaviour continues even for greater values of strain.

For a simpler comparison between results above and under the percolation threshold, we represent here the sensitivity (and its standard deviation) normalised to the sensitivity observed at the percolation density of $120 \text{ CNT}/\mu\text{m}^2$ (represented in red in Figure II.6.6).

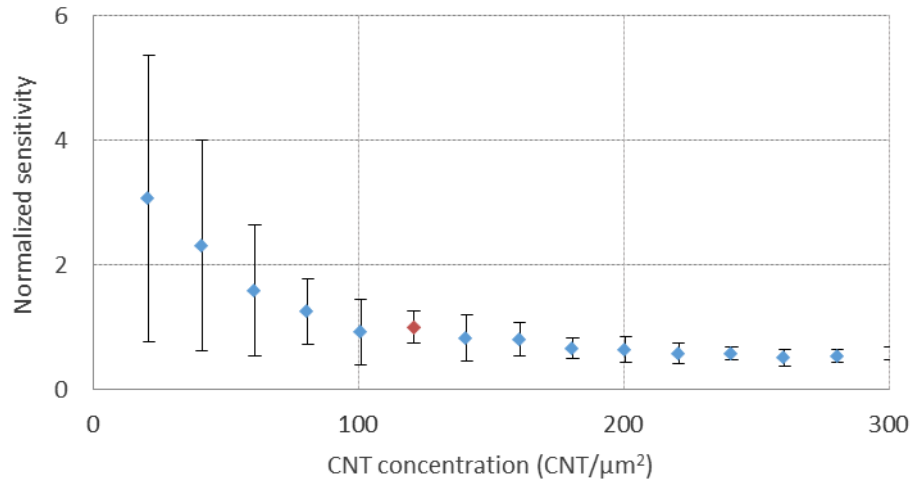


Figure II.6.6 The dependence of sensitivity and its variability on the density of CNTs imposed on the simulation. The error bars represent the standard deviation of the 10 simulations performed for each of the imposed values of density. The sensitivity is normalised to the sensitivity observed for a density of $120 \text{ CNT}/\mu\text{m}^2$ (represented in red).

The variability for a density of $240 \text{ CNT}/\mu\text{m}^2$ (equal to the density observed experimentally) is 10%, a value close to the variability observed experimentally (ranging from 8.4 % to 18 %). This result suggests that the variability observed experimentally might be inherited by the variability on the micrometric organization of the CNTs.

The CNT density is not the only parameter that affect the percolation threshold. A similar effect can be observed by changing the average CNT length. For a fixed density of $60 \text{ CNT}/\mu\text{m}^2$, we vary the CNT length from 300 nm to 700 nm (keeping the same standard deviation of 50 nm) (Figure II.6.7). For shorter CNT length, we can observe higher sensitivity and higher variability, whereas, for longer CNT length, the results exhibit lower sensitivity but are reproducible. Consequently, we can infer that the percolation threshold is lowered by longer CNTs, in agreement to (Balberg & Binenbaum, 1985) and (Berhan & Sastry, 2007).

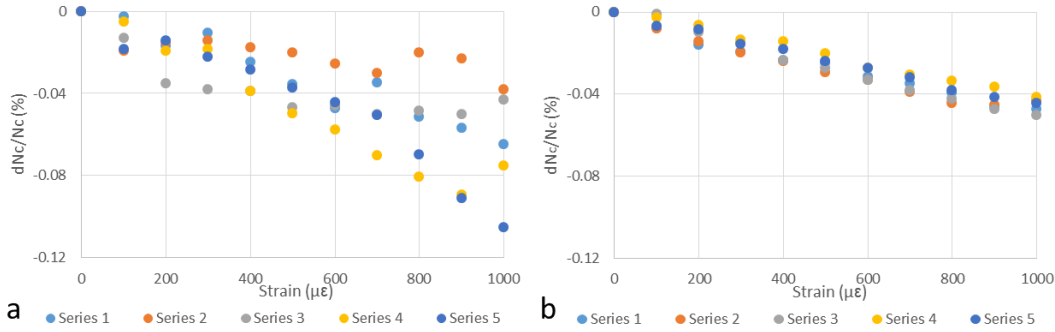


Figure II.6.7 Simulation results showing the relationship between variation of number of contacts (dN_c/N_c) and applied strain for different CNT length for a constant density of $60 \text{ CNT}/\mu\text{m}^2$. a) shows the results of 5 iterations of the simulation for a CNT length of 400 nm. b) shows the results for a CNT length of 700 nm. We can see that the CNT length affects vastly the percolation threshold, in agreement with (Hu, et al., 2010)

II.6.2.3 Interpretation of the simulation results

These results can be attributed to the mechanisms of conduction in networks close to percolation threshold. For networks close to percolation threshold, the number of contacts between CNTs is relatively low compared to networks well above percolation threshold. Consequently, a small reduction in the number of contacts caused by the deformation of the network has greater impact in a network close to percolation.

In electrical terms, in a network close to percolation threshold, the conduction paths extending from one side of the simulation cell to the other side are relatively few (Li, et al., 2008), consequently the reduction of contacts between CNT due to deformation impacts vastly the resistance of the network.

Moreover, the great variability of the results for networks close to percolation can be attributed to different organizations of the CNT network and the consequent creation of a different number of conduction paths from one side of the cell to the other. For higher density, the variability is less important because the CNT coverage of the substrate is much higher, consequently the variation of conduction paths created is relatively low.

These results are in good agreement with our experimental data that show much higher sensitivities for network close to percolation threshold, with the drawback of having a poorly reproducible fabrication process (Zhang, et al., 2013) (Srivastava, et al., 2011) (Li, et al., 2014).

Moreover, Figure II.6.6 and Figure II.6.7 show that the decrease in N_c is not monotonous. As stated previously, the Poisson effect can create new contacts that were not previously there. In the portions of the plot in which N_c increases slightly with respect to the previous data, the increment in N_c due to Poisson effect could be dominant with respect to the decrease in N_c due to the strain.

II.6.2.4 Comparison to experimental data

In II.4.1 we evaluated the surface density of CNTs to be $240 \text{ CTN}/\mu\text{m}^2$ and the effective CNT length to be 300 nm (where the effective CNT length is calculated as the length of the straight line connecting the two ends of a bent CNT). Imposing these values in the simulation, we obtained a reproducible result, indicative of a network above percolation threshold.

We remind that in section II.5.2 we evaluated the Gauge Factor (defined as $\frac{dR}{R} / \frac{dL}{L} = \frac{dR}{R} / \varepsilon$) to be 0.90. In Figure II.6.8, we represent experimental data for a $600 \mu\text{e}$ compared to the average result of 10 simulations.

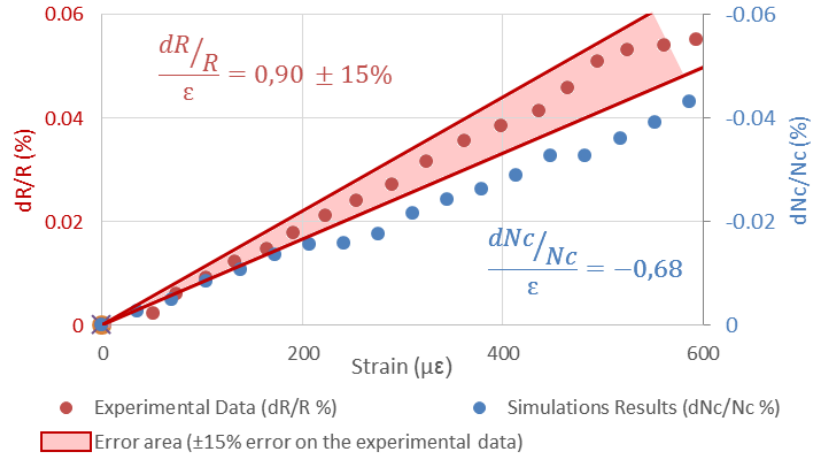


Figure II.6.8 Comparison between model and experimental data in the linear regime. The experimental data show the relationship between variation of resistance and strain. The data from the model show the relationship between variation of number of contacts (dN_c/N_c) and applied strain; they are the result of the average of 10 simulations performed imposing a density of $240 \text{ CNT}/\mu\text{m}^2$ and a CNT length of 300 nm.

The results of the model seem to describe well the piezoresistive behaviour of the CNT network. Though this simulation allows us to interpret the linear behaviour of the piezoresistive effect, it does not allow us to understand the causes of a quadratic behaviour for larger deformations. For this purpose a more complete model has been created.

II.6.3 CNTs modelled as sinusoidal rigid tubes

Some works suggested, by means of simulations, that CNT waviness is a factor strongly impacting the piezoresistive behaviour of CNT networks (Li, et al., 2008) (Yu, et al., 2013). Different approaches (see Figure II.6.9) have been investigated to model the waviness of CNTs: splines and polygons (Li & Chou, 2008) (Dalmas,

et al., 2004), double-hinged three-segment objects capped by hemispheres (Yu, et al., 2013), helical and spring shapes (Shi, et al., 2004). In our case, a sinusoidal approximation (Fisher, et al., 2003) better describes the CNTs observed on the substrate (see Figure II.6.10).

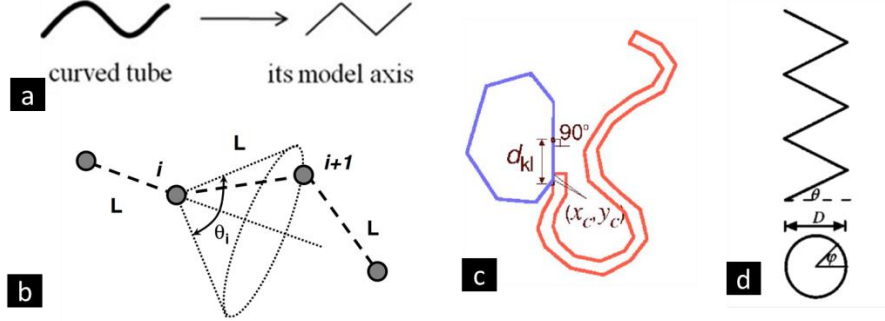


Figure II.6.9 Mathematical shapes used in different contributions simulating CNT networks. a) Double-hinged three-segment objects capped by hemispheres by (Li & Chou, 2008), b) polygons by (Dalmás, et al., 2004), c) spline by (Li & Chou, 2008) and d) spring shape by (Shi, et al., 2004).

II.6.3.1 Extraction of the parameter of simulation

The three parameters needed to simulate CNTs as sine waves are:

- the average effective length of the CNTs,
- the amplitude of the bends,
- the average number of periods that are contained in a deposited CNT.

Figure II.6.10 shows the analysis on 18 sample CNTs (analysis performed using ImageJ). Only CNTs that could be clearly identified are used in this evaluation. CNTs that merge in bundles cannot be clearly identified, and consequently they are not considered.

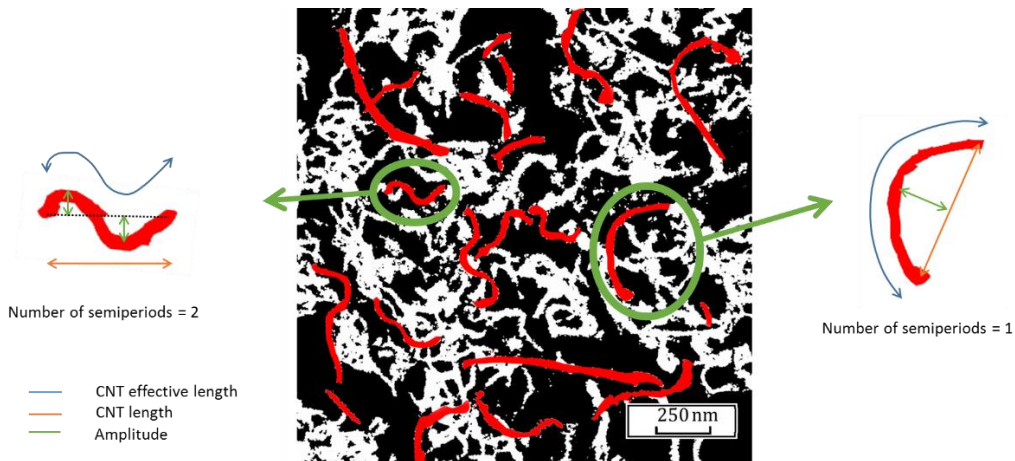


Figure II.6.10 Picture analysis to extract average CNT effective length, amplitude of the curvature and number of the semiperiods of deposited CNT.

This analysis highlights a great variability of the parameters of interest. Consequently, we opted for rendering this variability in our model. First, we extract the distribution of the three parameters from the image (see Figure II.6.11).

Second, we approximated the observed distribution by appropriate mathematical distributions (see Figure II.6.12). The effective CNT length is approximated by a normal distribution centred in 300 nm and standard deviation 100 nm; the amplitude is approximated by a uniform distribution between 0 and 150 nm and the number of semiperiods by a uniform distribution between 0 and 3.

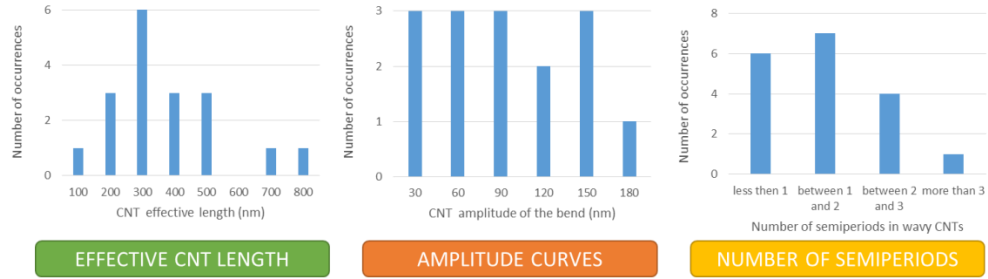


Figure II.6.11 Distribution of the CNT effective length, amplitude and number of semiperiods extracted by analysis of a SEM image of a deposition.

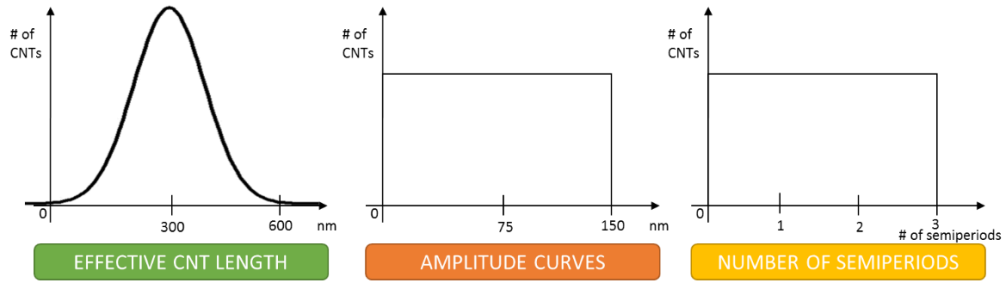


Figure II.6.12 Approximated distribution of CNT effective length, amplitude and number of semiperiods to simulate CNT in the model. The normal distribution on the effective CNT length approximates well the lengths up to 600 nm, but it neglects the longer CNTs. In the interest of having a simple function that randomizes the length of the CNTs, we use the normal distribution.

II.6.3.2 Methodology of simulation

Defining sinusoidal functions to represent each CNT, keeping them in memory and perform calculations on them to find crossings (contacts) is a daunting task, especially if we want to simulate the behaviour on a relatively big surface to minimize the effect errors introduced by the edges (size>2000px).

Consequently, an alternative method has to be used. Since we deal with deposition of CNTs on flat surfaces, we assume that the deposition can be approximated to be 2D. We propose to represent the nanotubes on a Boolean matrix in which each cell represents a pixel of an image. We use the 1 to represent a nanotube and 0 to represent the substrate still uncovered (see Figure II.6.13). The shape of a CNT is consequently defined pixel by pixel instead of a mathematical function as in the previous model. The use of Boolean variables allows us to save on the memory used to represent the different matrices and consequently we can perform the simulation of larger areas, to better model the reality. We assign an arbitrary length of 1 nm to each pixel. We perform a simulation on a matrix whose size is 4290px x 6000px. We chose this ratio (5/7) between the dimensions on the matrix to take into account the non-square shape of the device (see Figure II.3.2). The total size is

the maximum size allowable to store efficiently all the matrixes on a computer with 12 GB RAM memory running Matlab R2013.

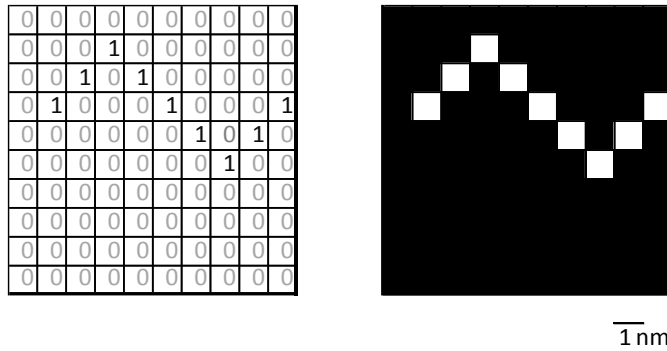


Figure II.6.13 Representation of CNTs on a Boolean matrix.

CNTs are generated one by one with an iterative function based on 5 fundamental steps (see Figure II.6.14):

1. An instance of a new CNT is generated. An effective length is assigned to it according to a normal distribution (see previous paragraph for more details).
2. A periodicity is assigned to the CNT. The value of the periodicity is such to create between 0 and 3 semiperiods in the length of the nanotube.
3. The amplitude of the wave is assigned to a random value between 0 and 120 nm.
4. The CNT is thickened to represent the diameter size of the CNT.
5. The CNT is placed on a matrix allocated to the representation of a single CNT. The CNT is placed in random location of the matrix with a random orientation.

During the all simulation, only four matrices of the same size are used:

- one matrix to represent one single nanotube (since the method is iterative, a matrix is used to generate a new CNT at each step),
- one matrix to represent all the previous nanotubes on a specific layer,
- one matrix to represent the precedent layer,
- one matrix to keep track of the number of crossings between CNTs.

The simulation follows an iterative method represented in Figure II.6.15. Here are the main steps for each iteration:

1. A nanotube is generated and represented on a first matrix.
2. The matrix of the previous CNTs is loaded (such matrix is empty when a new layer is initiated).
3. A Boolean AND function is performed between the current CNT and the previous CNTs. The AND function identifies crossings (contacts) between nanotubes. The resulting matrix is added to the matrix used to keep track of the contacts between CNTs. The operation of sum is important to count more than once the contacts between three or more CNTs in one spot.

4. A Boolean OR function is performed between the current CNT and the previous CNTs. The OR function is used to merge the current CNT to the matrix of the previous CNTs. The resulting merged matrix is used as input of the following iteration.
5. This iteration is performed on each CNT on a layer until we attain the desired surface density (240 CNT/ μm^2).
6. When a layer is finished, a Boolean AND function is performed between the matrix of all the CNTs on the current layer and the matrix of the previous layer (since two consecutive layers are in contact, CNT crossings have to be checked between consecutive layers).
7. A new iteration starts on a new layer until 20 layers are reached.

To make the function more efficient, not all the image is processed with Boolean functions. Only the rectangular area that contains the current CNT is checked (as shown by the blue frame represented on the matrixes of Figure II.6.15).

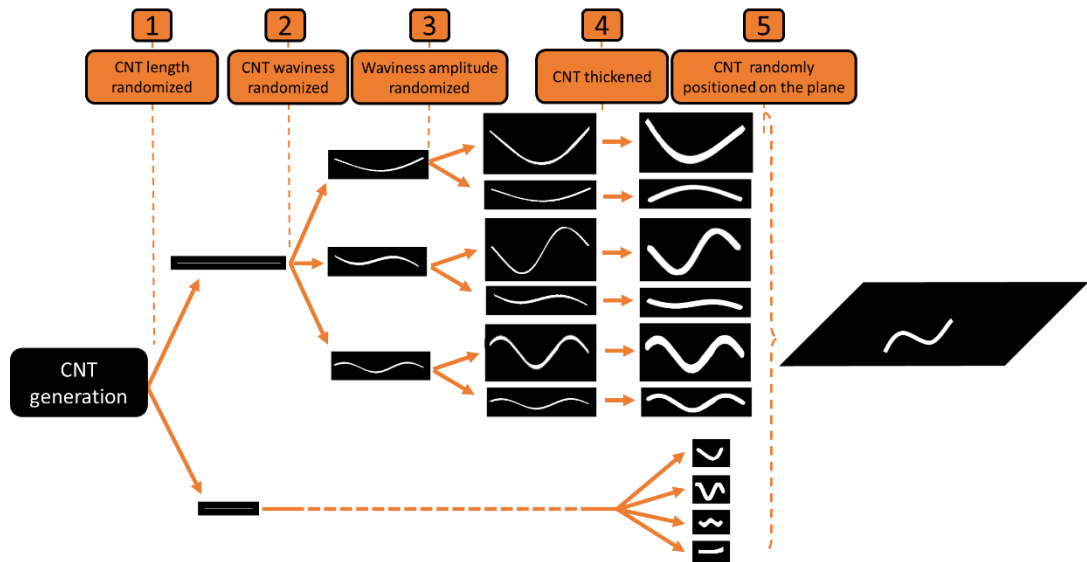


Figure II.6.14 Flowchart of CNT generation and placement on the substrate.

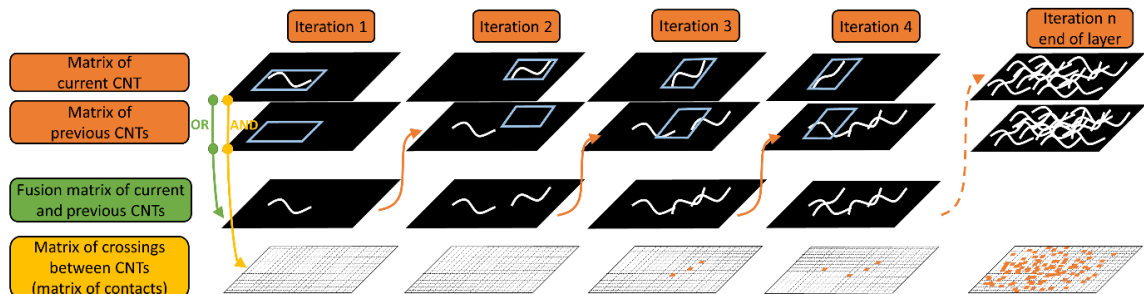


Figure II.6.15 Iterative method of construction of the CNT matrix.

Similarly, to the previous model, the mechanical deformation of the substrate is simulated by shifting the CNTs on the x-axis by their centre. For simplicity, they are treated as solid objects that do not deform during the shift process. Consequently, waviness and length are conserved in the process. The Poisson effect is taken into account as well.

It is worth noticing that the current method allows us to have a quantitative evaluation of the size of the contact. Since the CNT is defined pixel by pixel, we can evaluate the superposition of two nanotubes in terms of the number of pixel in common, as shown in Figure II.6.16.

We evaluate the total number of contacts as the sum of all contacting pixels, defined as Ncp (Number of Contacting Pixels).

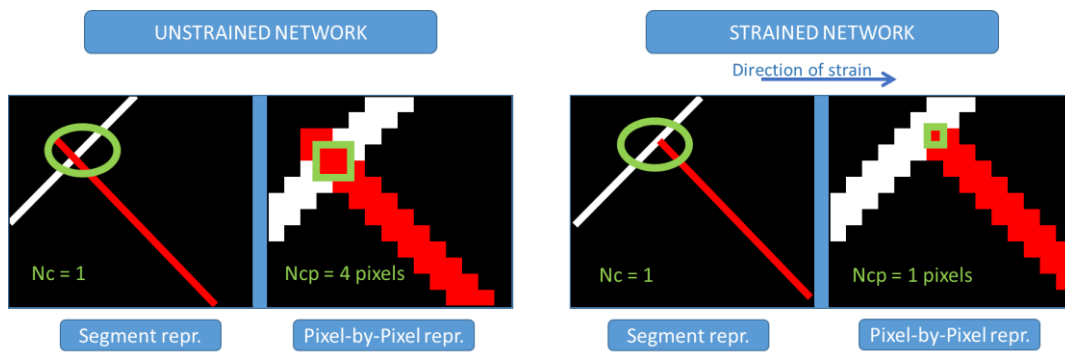


Figure II.6.16 Comparison between the two models in determining the contacts between two adjacent CNTs. N_c represents the Number of Contacts of the segment-based model and N_{cp} represents the Number of Contacting Pixels of the pixel-by-pixel model.

II.6.3.3 Comparison between the morphology observed experimentally and the morphology generated by the sinusoidal model

The image below shows the numerically generated image of a CNT layer (Figure II.6.17).

We can compare the SEM image of the real deposition of one layer of CNTs with the simulation result (see Figure II.6.18).

This simulation better represents the deposition compared to the previous model (see Figure II.6.3). The simulation still models the patchy distribution of CNTs, but there are other similarities:

- Imposing a diameter to the representation of CNTs, we can easily measure the surface coverage. For the SEM image, the surface coverage was evaluated to be 43% and the surface coverage of the model is 48%.
- The random distribution of length, waviness and periodicity of the CNTs better fits the great variety of CNT shapes found in the SEM image.

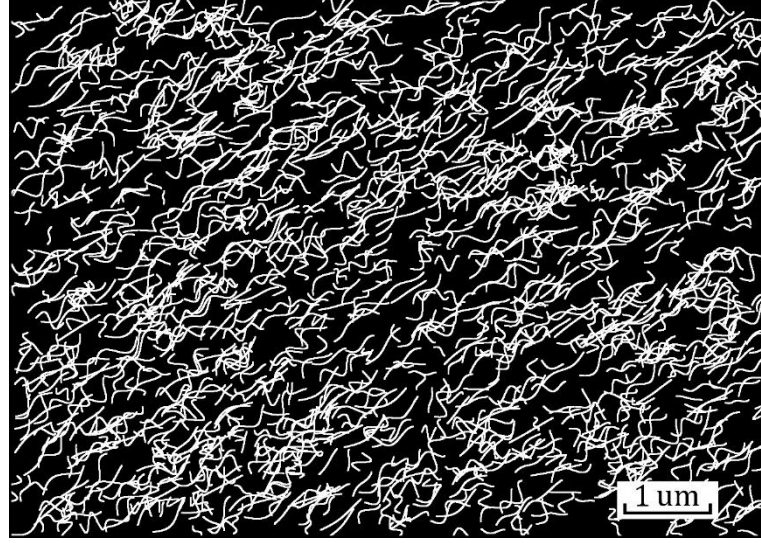


Figure II.6.17 Image of one deposited layer generated by the model. The surface density is set to 240 CNT/ μm^2 .

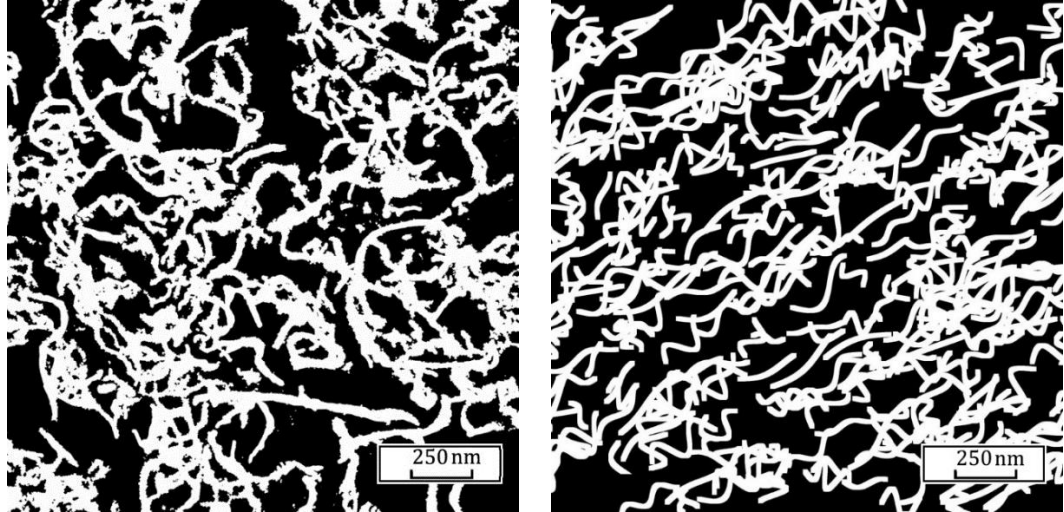


Figure II.6.18 Comparison between SEM image of the CNT network (on the left) and the morphology generated by the model (on the right). Both images represent one single layer out of the 20 the device is made of.

II.6.3.4 Result of simulation: piezoresistivity

We investigated the dependence of the piezoresistive behaviour on the curvature of the CNTs. The parameter of interest to mathematically describe the curvature of CNTs is the curl ratio, described as:

$$\text{curl ratio} = \frac{\text{CNT length}}{\text{effective CNT length}} \quad (\text{Li \& Chou, 2008}),$$

By increasing the periodicity of the amplitude of the sinusoidal waves that model the CNTs, the curl ratio increases.

For a curl ratio equal to 1 (a curl ratio of 1 identifies straight objects) the variation of number of contacts is fully linear, similarly to II.6.2.

For curl ratios different from 1, the variation of the number of contacts seems to depend quadratically on the strain applied.

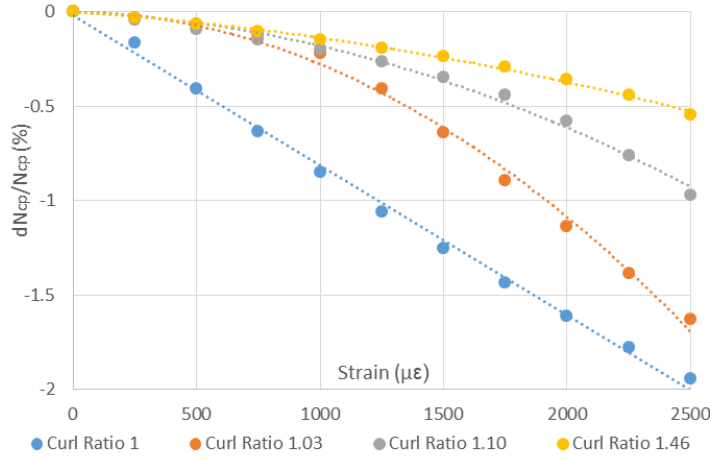


Figure II.6.19 Simulation results showing the relationship between variation of number of contacts (dN_{cp}/N_{cp}) and applied strain for different curl ratios.

From the analysis of Figure II.6.19, we found an average curl ratio of 1.30. Imposing this average value to the simulation, we obtain the characteristic shown in Figure II.6.20. We can appreciate that for a small number of layers, the sensitivity is higher and, as the number of layers increases, the sensitivity decreases and reaches a stable value above 10 layers. This result is in good agreement with the previous model and experimental data, as discussed in II.6.2.2.

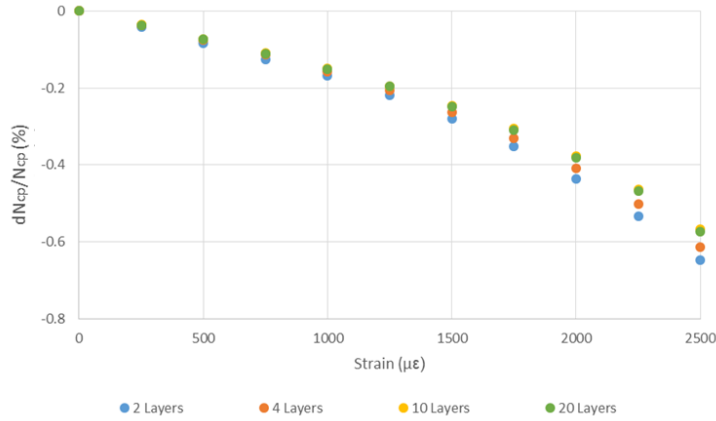


Figure II.6.20 Simulation results showing the relationship between variation of number of contacts (dN_{cp}/N_{cp}) and applied strain for different numbers of deposited layers.

II.6.3.5 Comparison to experimental data

We compared the result of the simulation (expressed as the variation of the number of contacts as a function of the applied strain) to the experimental data describing the piezoresistive behaviour for large strain (2500 με).

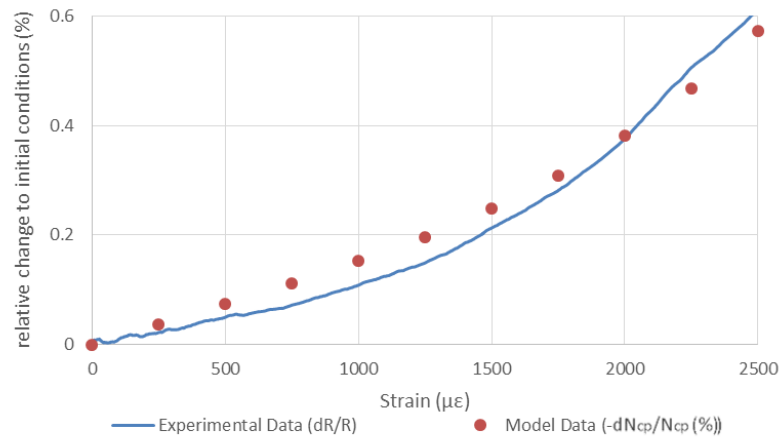


Figure II.6.21 Comparison between model and experimental data for large deformation (2500 µε).

In the linear regime, the result is shown in Figure II.6.22.

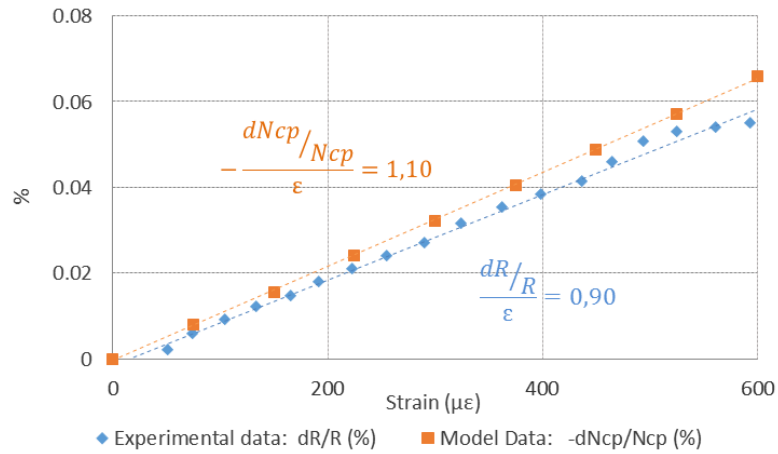


Figure II.6.22 Linearization of the model for small deformations (600 µε).

II.6.3.6 Discussion on the modelling of the piezoresistive behaviour

The similarity between the experimental curves and the numerical results are a strong argument in favour of our thesis that the piezoresistive behaviour is driven by the reduction of the number of contacts at the micro scale in the CNT network.

The second model suggests that the quadratic behaviour observed in the experimental data could be attributed to the waviness of the CNTs.

Nevertheless, a few improvements can be identified for future versions of the model.

Firstly, a future development of the model will include an iterative procedure for the calculation of the resistance from the number of contacts, as suggested by (Kirkpatrick, 1973) (Balberg & Binenbaum, 1985) (Lavric, et al., 2015).

Secondly, the range waviness chosen for the simulation may not reflect the real waviness of the CNTs in the real devices. A systematic study of several SEM images can provide more statistically significant information on the actual value and distribution of this parameter.

Thirdly, the fact that CNTs are treated as rigid objects that do not deform may introduce errors in the evaluation of the number of contacts, especially at larger strains where the CNTs are more likely to deform and untangle.

In addition, the rigid representation of CNTs on a 2D surface causes some errors in the count of the global number of contacts because it impedes the evaluation of the contacts between non-adjacent layers. As shown in Figure II.6.23, when the CNTs are modelled as rigid 2D objects deposited on a horizontal plane, the CNTs on the third layer are not in contact with the CNTs on the first layer even if the second layer has a gap. This condition is not uncommon, looking at the morphology of both experimental images and numerical representations. We believe that modelling this kind of contact would not only increase the accuracy of our model for the piezoresistive effect, but also it would represent a powerful tool to evaluate the densification of the network for an increasing number of layers.

Moreover, the CNTs are modelled as soft-core objects and the study of the hard-core behaviour could provide additional insight to better understand the phenomena occurring at the nano scale in the CNT network.

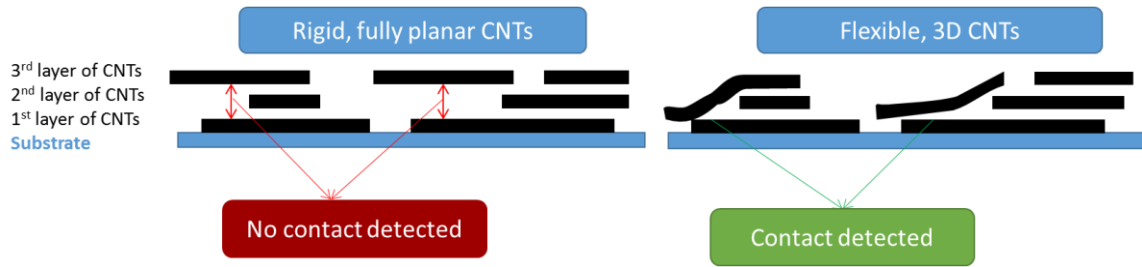


Figure II.6.23 Rigid vs. flexible representation of CNTs for the identification of contacts between CNTs of non-adjacent layers.

II.7 SENSITIVITY TO OTHER PARAMETERS

In 0, we discussed the importance of having a multifunctional device sensitive to different parameters in order to have a comprehensive information about the health of a structure. In this section, we investigate the sensitivity of our device to two other parameters of interest in SHM applications: pH and humidity.

II.7.1 Sensitivity to pH

This work has been carried out with the help of the intern Benjamin Caduc during his 4-months internship in our laboratories. More detailed information can be found in his master thesis (Caduc, 2014).

II.7.1.1 Results of characterization

We studied the response of the device to electrical stimulation for different levels of pH (Figure II.7.1). The plot shows a strong dependence of the resistance over the pH. Nevertheless, since the curve is not monotonous, the measurement for high pH can be ambiguous.

For its linearity between pH 1 and pH 9, this device can find applications in fields requiring a limited range, such as the water quality measurement (Storey, et al., 2011).

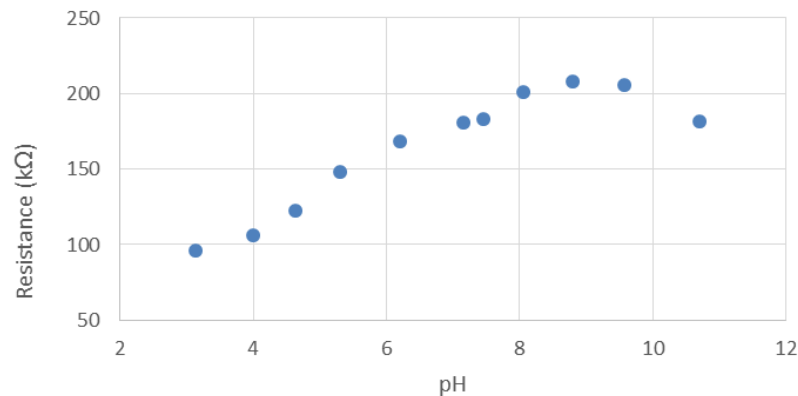


Figure II.7.1 Dependence of resistance over pH.

Two types of reaction may be occurring at the interface between the CNT network and the ionic solution: Redox reactions (Luo, et al., 2001) and acid-bas reactions (Gou, et al., 2014) (Back & Shim, 2006). We believe that a combination of these effects might explain the phenomena observed during the characterization.

We proved that the device could be used as a pH sensor, but we will not explore this phenomenon further as it lies outside the main goal of this thesis.

II.7.2 Humidity sensitivity

The resistance of the device showed strong dependence over humidity. Figure II.7.2 summarises the results (the curves are terminated at values less then 100%

RH because for higher humidity values, the behaviour of the devices is no longer purely resistive).

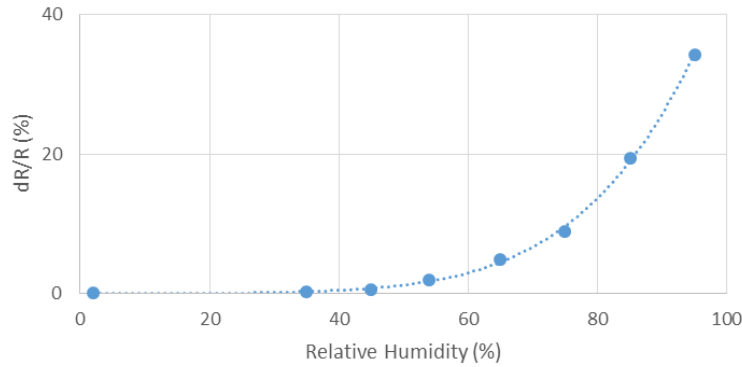


Figure II.7.2 Dependence of the resistance over relative humidity. Three types of rinsing frequencies are taken into consideration.

We demonstrated that the device can be used as a humidity sensor and it can be tuned to be sensitive to particular ranges of RH. However, we will not explore this phenomenon further as it lies outside the main goal of this thesis.

II.7.3 Passivation

In order to use this sensor in real applications, a passivation is needed to isolate the piezoresistive behaviour from the sensitivity to pH and humidity.

Experimental results demonstrate that the deposition of a thin layer of epoxy resin (SU8) is sufficient to isolate the CNT network from the surrounding environment. Moreover, this flexible epoxy resin does not affect the piezoresistivity of the device.

We would like to stress the point that the deposition of a thin epoxy layer on the CNT network can be easily integrated in the serial fabrication process described in the previous sections. We believe that this is an important point considering the goal of providing a low cost CNT-based strain sensor.

II.8 CONCLUSION : A FLEXIBLE, MULTIFUNCTIONAL CNT-BASED SENSING ELEMENT

In this chapter, we have presented the fabrication of a CNT-based strain sensor with a sensitivity and a precision adapted to the detection of micro cracks in concrete.

For the first time in the scientific literature, the variability of the sensitivity of CNN-based flexible ohmic sensors is evaluated.

The use of inkjet printing produces highly reproducible devices with low variability in resistance (8.4 % standard deviation), gauge factor (16 % standard deviation), and temperature sensitivity (8 % standard deviation). Compared to the state of the art of CNN strain gauges, the devices demonstrate remarkable cyclability and hysteresis-free operation.

The possibility of batch producing the sensor and the use of low-cost materials, ensure the cost effectiveness of the sensing element.

Moreover, the sensing element demonstrates good sensitivity and selectivity to other parameters such as pH, temperature and humidity, a clue that motivates us to think that the device can provide a customizable base for the production of a multipurpose sensing element.

These promising results motivate our optimism in the use of such sensors in real-life applications demonstrated in the following chapters.

PART III.

WIRELESS ELECTRONIC PLATFORM FOR DATA ACQUISITION AND COMMUNICATION

PART III.

WIRELESS ELECTRONIC PLATFORM FOR DATA ACQUISITION AND COMMUNICATION

In the previous section we presented the design, fabrication and characterization of a sensing element able to detect micrometric deformations and showcasing promising sensitivity to humidity and pH. We believe that such sensing element could be of great interest in SHM applications. An electronic circuit is needed to perform the signal conditioning, digitalization of the information, wireless communication of the reading through concrete. In this section we present our work on the design, development and fabrication of the electronic board used.

III.1 ARCHITECTURE OF THE WIRELESS SENSOR NODE

We present the design and fabrication of the first multifunctional wireless sensor node for volume SHM in concrete structures.

The system is organised as shown in Figure III.1.1.

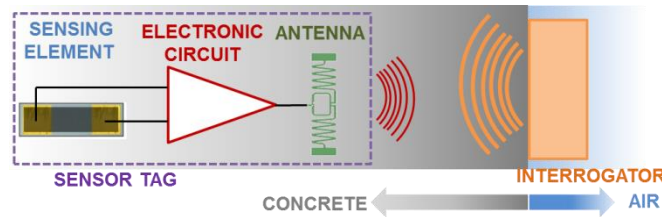


Figure III.1.1 Structure and terminology used in the system.

The sensing element is the CNT-based strain gauge described in Section II.

The electronic circuit represents the signal conditioning stage and the Analog to Digital Converter (ADC). The signal conditioning circuit manipulates the signal coming from the sensing element to prepare it for its digitization.

The antenna is specifically designed for the transmission through concrete and optimized to reduce its size.

We power the current version of the system with a 3 V button cell battery (CR1225) offering a good compromise between the capacity of the battery and its size.

A protective shield is fabricated in order to protect the system when embedded in concrete and to improve the antenna efficiency.

The system is read by a commercial RFID reader (the AMS AS3993-QF RADON) linked to a commercial patch antenna with a gain of (6.4 ± 0.1) dBi at 865-868 MHz (European UHF RFID slot).

III.2 SIGNAL CONDITIONING ELECTRONICS

In this chapter, we present the circuit for signal conditioning. We start by defining the objectives and the constraints applicable to the design of such circuit. Secondly, we describe the design of the circuit and its fabrication; we finish by the characterization of the designed circuit and the identification of possible improvements.

This section of the work is developed in cooperation with Fadi Zaki, during his Master's internship.

III.2.1 Goals and constrains

The constraints imposed on the system are multiple. They can be imposed by the application, the sensing element, the energy source(s), the protocol of communication, the harsh environment of concrete, etc. In order to organise the constraints, we will divide them in two categories: external and internal constraints.

III.2.1.1 External constraints

As previously discussed (see I.3.2), the data communication between **the sensor buried in concrete** and the external world **has to be wireless**. For this constraint, another limitation applies: the **power source has a limited capacity**. The buried sensor cannot rely on the external power supply and consequently two options are available: internal battery and energy harvesting. Both solutions can provide only a limited amount of energy and consequently the **power consumption of the final device has to be minimized**. In this thesis the sensor is powered by cell battery since it can ensure years of operation with satisfying capacity. In future development, the power supply may be ensured by an electromagnetic energy harvester that exploits the existing antenna to receive and store the power received by the interrogator outside the structure. In order to develop a signal-conditioning circuit adapted to this future energy source, an estimate of the available energy is needed. Several works suggest the possibility of harvesting around 1 μW of power in non-ideal conditions like ours (Shams & Ali, 2007) (Sample & Smith, 2009) (Nishimoto, et al., 2010) (Jiang, 2011) (Nintanavongsa, et al., 2012) (Ishida & Furukawa, 2014). Since the processes to be measured in concrete structures are slow, a low sampling frequency is required. Consequently, it is possible to increase the harvesting time between measurements for a higher amount of harvested energy. Supposing a measurement every 15 minutes, it would allow the acquisition of roughly 100 measurements a day: a quantity of data sufficient to track long and slow processes.

At a rate of 1 μW , the total energy harvested in 15 minutes is roughly 1 mJ. To perform the measurement, the sensor is likely to stay awake for 1s to stabilise the measurement and to average several acquisitions. Consequently, the power consumption of the circuitry has to be lower than 1 mW.

Secondly, being this device supposed to provide information on the ageing, stability and health of a structure, it is unreasonable to embed a sensor whose size is big enough to weaken the structure itself. Hence, **the size of the device has to be minimized.**

Thirdly, the device will be subject to great temperature fluctuations, known to affect the sensors' behaviour. Consequently, **an internal correction for temperature fluctuation has to be developed.**

III.2.1.2 Internal constraints

As seen in Section I, the output of the sensing element is always expressed as dR/R , that is the variation of the resistance normalized for the nominal value. Consequently, **the conditioning circuit has to be able to provide normalised measurements.**

Moreover, the circuit has to be easily adapted to accommodate for the variability on the nominal value of the resistances. In fact this variability can be bigger than the variations due to a measurand. Consequently, in this initial stage of development, it is of utmost importance that **the conditioning circuit is easily tuneable for each of the single sensing element used.**

Moreover, **the signal will need to be highly amplified** since the variation of resistances is quite limited (less than 1 %). At the same time, the noise should be kept at the minimum possible level.

III.2.2 Inadequacy of the traditional Wheatstone bridge

The most used conditioning circuit for resistive sensors is the Wheatstone bridge. The common architecture is composed of two resistor branches connected in parallel, where the first branch is composed of a series of fixed resistors that provide a voltage reference and the second branch comprises a fixed resistor and the resistive sensor. The unbalance generated at the midpoint is detected as the output voltage and is a function of the variation of the sensor's resistance (see Figure III.2.1).

Because our sensing element shows a strong dependence on the temperature, the output of the bridge is highly affected by temperature changes (see Figure III.2.1). The output variation due to temperature can be much greater than the output due to mechanical deformation, thus impeding a correct reading.

One solution to this is to place a second sensing element in the first branch of the circuit, as shown in Figure III.2.2. This second sensing element should be conditioned in such a way that it is not subject to mechanical deformation (for example by gluing it to a rigid substrate).

In this configuration, the temperature sensitivity is partially corrected as shown in Figure III.2.2. The simulation results show that an increase in temperature changes the slope of the output characteristic of the bridge. Comparing the slopes of the output characteristic at different temperatures, we can infer that a variation of 1 °C introduces a relative error on the strain measurement of 0.1 %. Since in real life

applications it is possible to encounter temperature variations of more than 30 °C, the error introduced on the measurement of the strain would be higher than 3 %. We would like to stress the point that these values are the best-case scenario and we believe that in real applications the performance will be further degraded. Consequently, we believe that this compensation is not sufficient for our application. For this reason the Wheatstone bridge configuration was discarded.

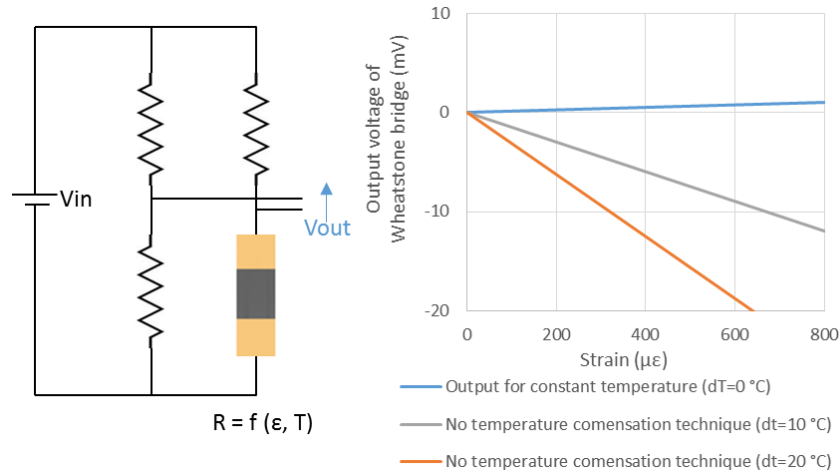


Figure III.2.1 Classical configuration of the Wheatstone bridge. On the left, the schematic of the circuit. On the right, the output of the circuit when the temperature is changed. We can see that the output voltage is highly dependent on the temperature.

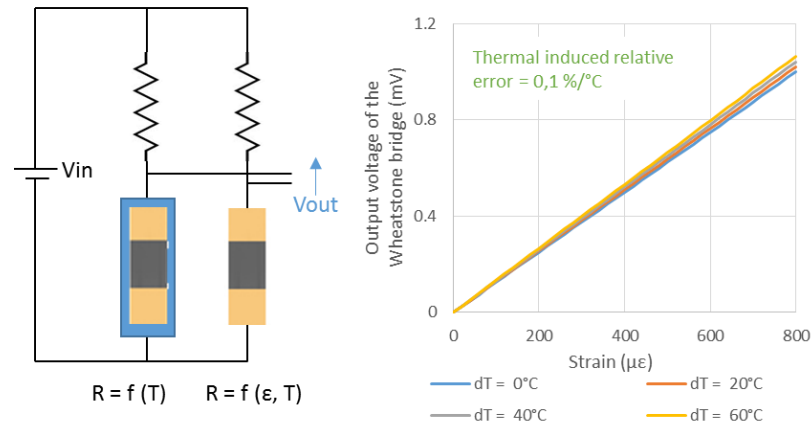


Figure III.2.2 Modified configuration of the Wheatstone bridge for temperature compensation. On the left, the schematic of the circuit. On the right, the output of the circuit when the temperature is changed. We can see that the output voltage is much less dependent on the temperature.

III.2.3 Proposed architecture for signal conditioning

For the development of a condition circuit, we make three main assumptions, supported by the section I.1:

- for small strains (lower than 600 $\mu\epsilon$), the response of the device is fully linear (in formulas: $\left. \frac{dR}{R} \right|_{\epsilon} = GF * \epsilon$ where ϵ is the strain applied and GF is the Gauge Factor)
- for small temperature variations (in the range 15 °C – 40 °C, the response of the device is fully linear (in formulas: $\left. \frac{dR}{R} \right|_T = \alpha_T * dT$ where dT is the temperature variation and α_T is the sensitivity to the temperature)
- the sensitivities to strain and temperature are independent to changes in, respectively, temperature and deformation. Consequently we assume that the total output of the sensor can be divided in separate and independent contributions (in formulas: $\frac{dR}{R} = GF * \epsilon + \alpha_T * dT$). Despite this assumption is not completely demonstrated by our dataset, we believe that it is reasonable enough to base the first version of the circuit on.

III.2.3.1 First stage – conversion of the variation of the resistance into a signal

According to the assumptions stated before, both temperature variations and strain can be inferred by evaluating the variations of the ratio dR/R . The circuit that allows us to compute the ratio of two resistive values is the non-inverting amplifier (see Figure III.2.3).

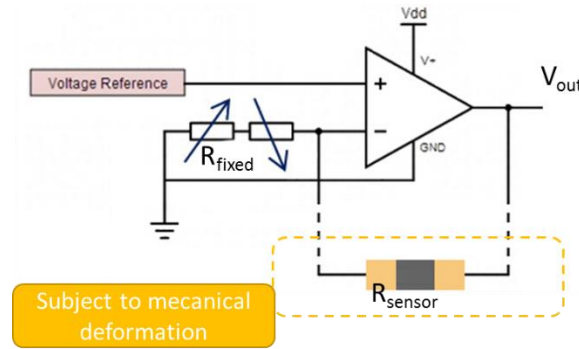


Figure III.2.3 First stage of the conditioning circuit. The normalization of the resistance is achieved with a non-inverting amplifier. The resistance R_{fixed} can be obtained by combining two different resistors in with opposite thermal coefficients to achieve high temperature stability (Hayasaka, 1976).

With this circuit, if R_{fixed} is set to be equal to the initial resistance of the sensor $R_{sensor0}$, the output is linearly dependent on the strain and temperature variation applied, as shown by the formula:

$$\begin{aligned}
 V_{out} &= V_{ref} \cdot \left(1 + \frac{R_{sensor}}{R_{fixed}}\right) = V_{ref} \cdot \left(1 + \frac{R_{sensor_0} + dR_{sensor}}{R_{fixed}}\right) \\
 &= V_{ref} \cdot \left(1 + \frac{R_{sensor_0}}{R_{fixed}} + \frac{dR_{sensor}}{R_{fixed}}\right) = V_{ref} \cdot \left(1 + 1 + \frac{dR_{sensor}}{R_{fixed}}\right) \\
 &= V_{ref} \left(2 + \frac{dR_{sensor}}{R_{sensor}}\right) = V_{ref} [2 + (GF * \varepsilon + \alpha_T * dT)] = \\
 &= 2V_{ref} + V_{ref} \cdot (GF * \varepsilon + \alpha_T * dT)
 \end{aligned}$$

The resistance R_{fixed} can be obtained by combining two different resistors in series. If these resistors are chosen to have opposite thermal coefficients, it is possible to achieve high temperature stability (Hayasaka, 1976). This technique reduces the thermal sensitivity of the circuit.

The choice of the operational amplifier was driven by three parameters:

- low quiescent current (17 μ A);
- single supply, rail-to-rail operation to exploit all the 3 V dynamic provided by the power supply;
- low offset (10 μ V) and low noise (1 μ Vpp equivalent to less than 0.01% of the output signal of the circuit).

The OPA333 was eventually selected (Texas Instruments, 2013).

III.2.3.2 Temperature compensation and amplification

We can develop a circuit that fully compensates for the linear part of the temperature sensitivity.

Two elementary cells described in the previous paragraph are needed.

- In the first one, the resistive sensing element should be installed in its working environment (for example concrete). This sensing element should be coated by a protective layer of SU8 to decrease its sensitivity to humidity and pH (see II.7.3). Consequently the sensor is sensitive predominantly to strain and temperature.
- The sensing element of the second elementary cell should be coated with the protective SU8 layer and attached to a rigid substrate in the proximities of the first one. Being attached to a rigid substrate, this sensing element is predominantly sensitive only to temperature.

By means of an instrumentation amplifier (INA) (Figure III.2.4), it is possible to subtract the two contributions and compensate for the temperature sensitivity

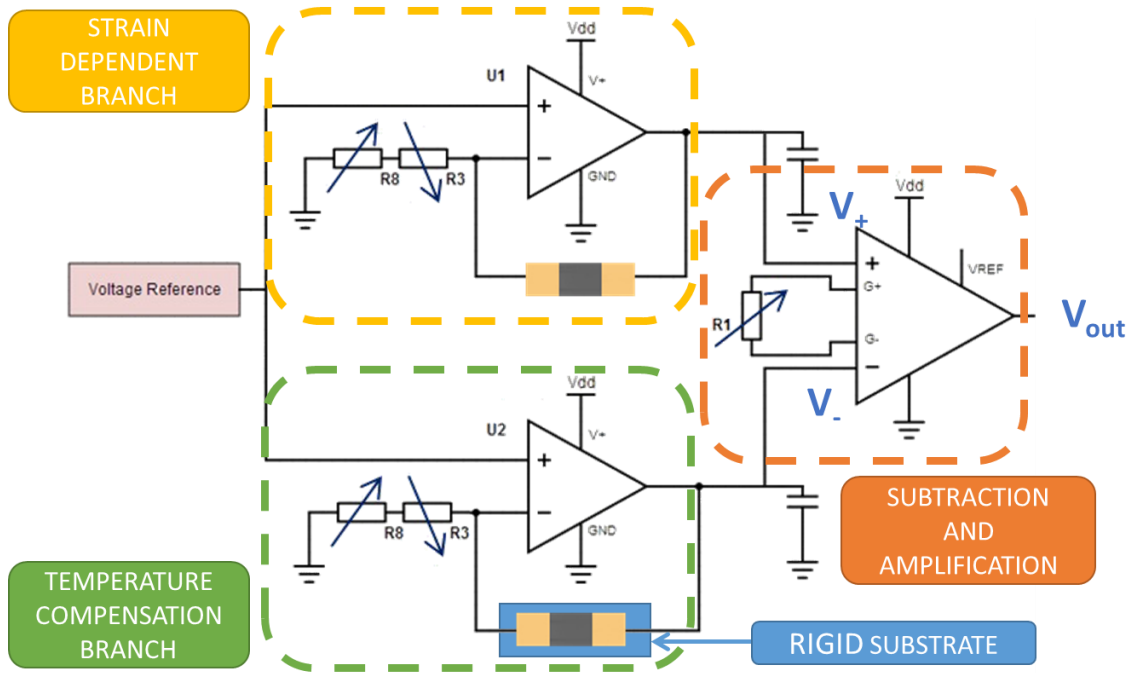


Figure III.2.4 Temperature compensation and amplification by means of a differential instrumentation amplifier. R1 is the resistor used to fix the gain of the differential amplifier.

The following calculations demonstrate the feasibility of the compensation:

$$\begin{aligned}
 V_+ &= 2V_{ref} + V_{ref} \cdot (GF \cdot \varepsilon + \alpha_T \cdot dT) \\
 V_- &= 2V_{ref} + V_{ref} \cdot (\alpha_T \cdot dT) \\
 V_{out} &= Gain \cdot V_{in} = Gain \cdot (V_+ - V_-) \\
 &= Gain \\
 &\quad \cdot V_{ref} [(GF \cdot \varepsilon + \alpha_T \cdot dT)_- - (\alpha_T \cdot dT)_+] \\
 &= Gain \cdot V_{ref} (GF \cdot \varepsilon)
 \end{aligned}$$

Similarly to the choice of the operational amplifier, the instrumental amplifier was selected on the basis of:

- low quiescent current (25 μ A);
- single supply, rail-to-rail operation to exploit all the 3 V dynamic provided by the power supply;
- low drift (0.1 μ V/ $^{\circ}$ C), low offset (10 μ V) and low noise (1 μ Vpp equivalent to less than 0.01% of the output signal of the circuit)).

The INA333 was selected as optimal candidate (Texas Instruments, 2008).

The choice of the component influences the choice of the voltage reference. In fact, in order to exploit the component for its rail-to-rail operation and the great range of possible gains, the input common mode should be around 1.5 V (as shown in Figure III.2.5). We remind that the input common mode is the fixed part of the signals V_- and V_+ of Figure III.2.4 due to the amplification of the input voltage reference.

In each of the elementary cells, the ratio between the resistance of the sensing element and the fixed resistors is roughly 1 and, consequently, the input common mode in the instrumental amplifier is roughly double the voltage reference (see the previous equations). As a consequence, the optimal voltage reference is 0.75 V.

The Voltage Reference pin of the SL900A, specifically designed for external circuits, provides this voltage.

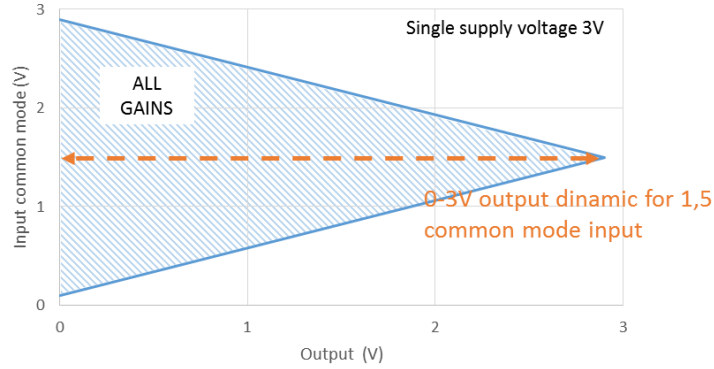


Figure III.2.5 Typical common mode range vs. output dynamic for the INA333 powered by a single supply voltage set at 3 V (Texas Instruments, 2008). In order to have a full rail to rail output dynamic, the input common mode should be 1.5 V.

The resistance R_1 connected to the instrumentation amplifier determines the gain on the amplifier, according to the equation:

$$Gain_{INA} = 1 + \frac{100k\Omega}{R_1}$$

III.2.3.3 Filtering

In II.5.3 we demonstrated how the sensing element is adapted to measurement in the static regime or for slow deformations much slower than 1 Hz. Consequently we can filter out any output frequency higher than this value, thus reducing the noise of the measurement. Keeping in mind the constraints on the power consumption and the size of the circuit, we opted for one main active filtering stage after the instrumentation amplifier and two capacitors between the output of the elementary cells and input of the instrumentation amplifier. The active circuit selected of the filtering stage is a second-order low-pass filter in the Sallen-Key configuration (Figure III.2.6).

The Sallen-Key filter offers the possibility of introducing an additional amplification stage without additional operational amplifiers. The resistances R_3 and R_4 are responsible for the total gain according to this equation: $Gain_{filter} = \frac{R_4}{R_3}$.

The total gain is expressed by: $Gain = Gain_{INA} * Gain_{filter}$

The combination of the first amplification with the instrumentation amplifier and the second amplification with the Sallen-Key affects the maximum detectable strain. Figure III.2.7 shows the relationship between amplification and the maximum detectable strain.

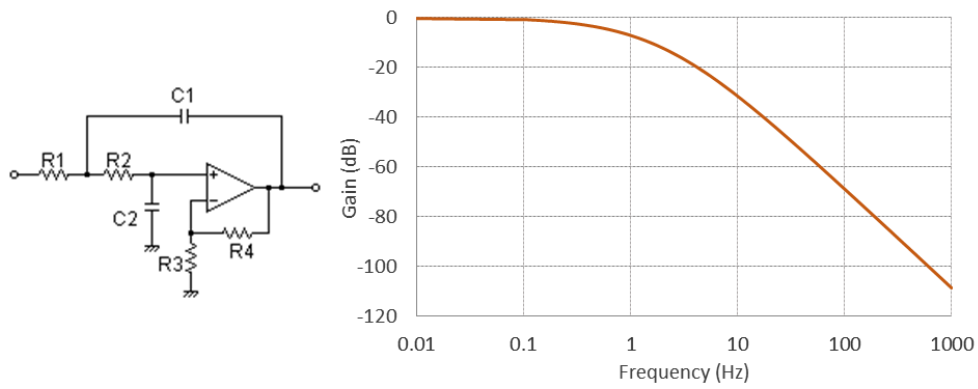


Figure III.2.6 Sallen-Key filtering stage to reduce noise. On the left, the schematic of the circuit: on the right, the transfer function.

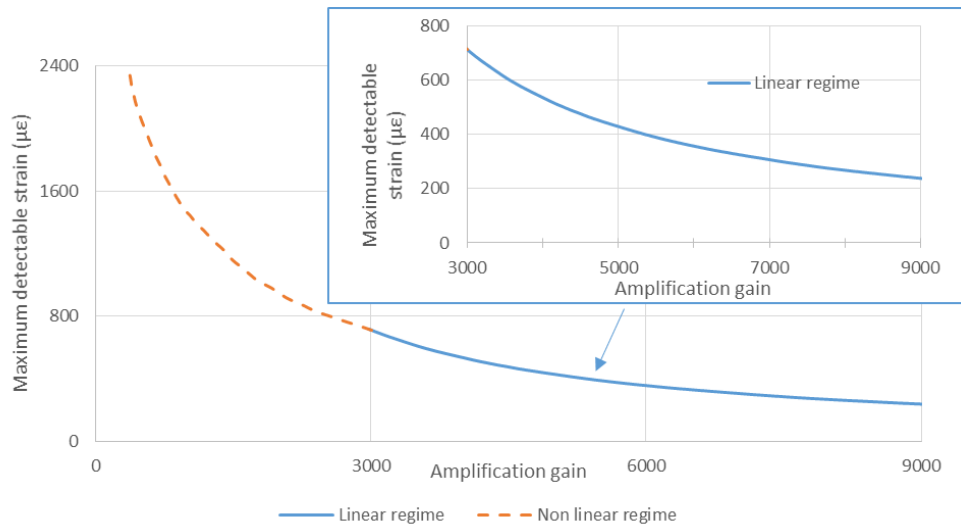


Figure III.2.7 The maximum detectable strain as a function of the imposed amplification gain. Simulation result using NGSPICE (v 26) to simulate the circuit.

III.2.3.4 Total circuit

Figure III.2.10 shows the global circuit. The supply voltage of this circuit is a 3 V DC signal.

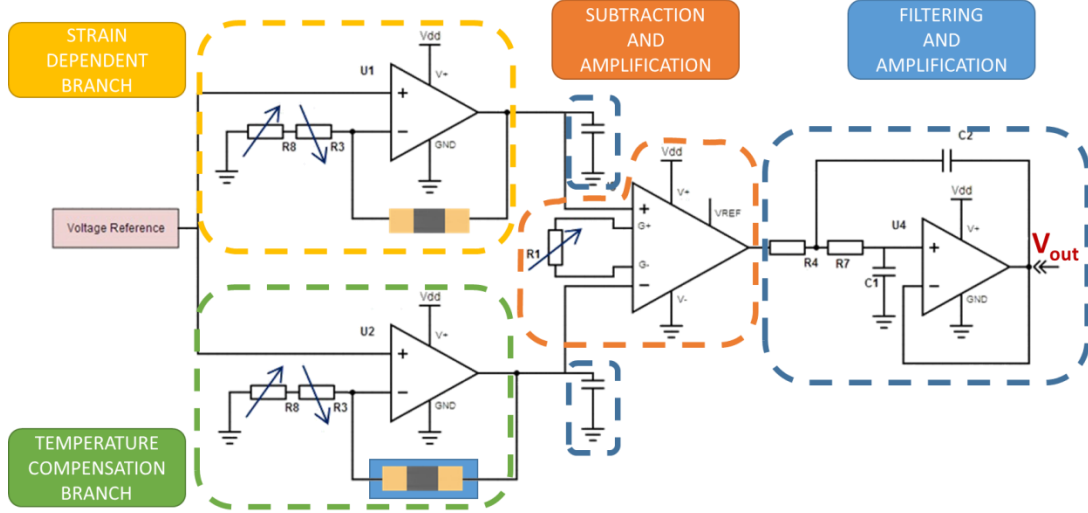


Figure III.2.8 Total circuit with its four main building blocks.

III.2.4 Simulation of the circuit

The simulation of the circuit was carried out with NG Spice v.26 (NG Spice, 2014). The sensing element are modelled as resistors with a nominal value of 150 kΩ and a dependence on strain and temperature as described by the equation:

$$R_{sensitive\ element} = R_{sensor_0} (GF * \varepsilon + \alpha_T * dT)$$

Several simulations were carried out to validate the behaviour of the circuit under mechanical deformations with temperature fluctuations. The sensitivity to noise was also analysed.

III.2.4.1 Mechanical deformation

Imposing a gain of 2500, the maximum strain detectable before the saturation of the instrumentation amplifier is 800 με. The simulation confirms this result and shows a linear voltage output for such deformation (see Figure III.2.9).

The rail-to-rail operation of the selected amplifiers ensures an ample dynamic of the output signal in the 0-3 V range.

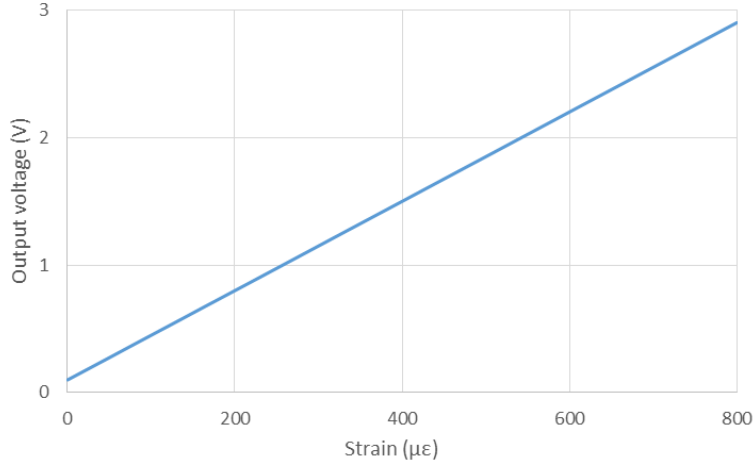


Figure III.2.9 Result of the circuit simulation showing the voltage output for an input deformation of up to 800 μϵ. The gain is set to 2500.

III.2.4.2 Noise performance

We study the noise generated by the circuit itself. The simulator allows us to predict the Poisson noise (also known as shot noise), the Johnson–Nyquist noise (also known as thermal noise), white and the pink noise (also known as flicker noise). Figure III.2.10 shows the spectral density of the thermal noise generated by the circuit.

From the noise spectral density we can calculate the root mean square of the noise as $V_{RMS} = \sqrt{\int (\text{noise spectral density})^2}$

Because of its simplicity and the small number of components, the Root Mean Square (RMS) of the noise generated by the circuit is around only 200 μV (the noise spectral density was integrated in the frequency range 0-10⁸ Hz).

The ADC used in the current prototype version works on 10 bits (see Section I.1 for further details), thus dividing the 0-3 V input dynamic range on 2¹⁰=1024 levels of 2.93 mV. Consequently, the introduced noise is negligible compared to the quantization noise.

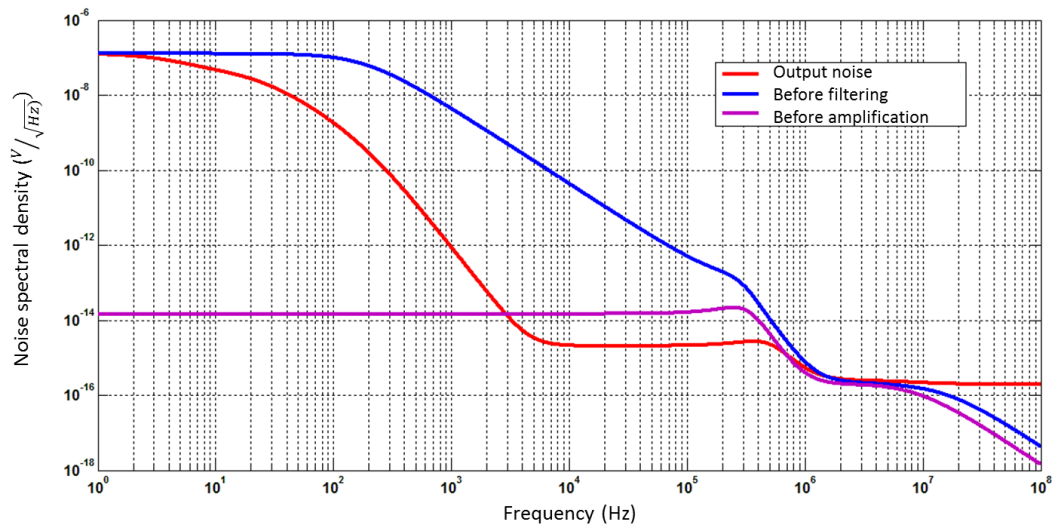


Figure III.2.10 Noise performance of the circuit at different frequencies. The curve “before amplification” describe the noise on the circuit shown in Figure III.2.3, “before filtering” the noise of the circuit in Figure III.2.4 and “output noise” is the noise of the total circuit shown in Figure III.2.8.

III.2.5 Circuit Fabrication

III.2.5.1 Routing

We routed the circuit with the software Eagle v6.6 for the fabrication of the final printed circuit board (PCB). Figure III.2.11 shows the final layout. In routing the circuit, we had to minimize the length of the wires of the circuit for two reasons:

- Decrease the total size of the device, thus minimising its impact when casted into concrete structures.
- Decrease the length of the different path on the PCB to minimize electromagnetic coupling with the antenna. In fact, the antenna will be placed close to the circuit and any electromagnetic coupling between the antenna and the circuit would both increase the noise into the circuit and decrease the antenna efficiency.

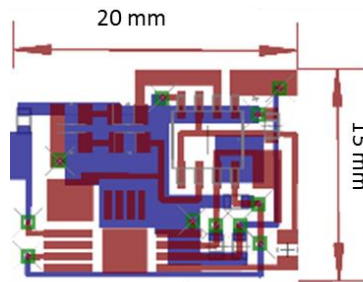


Figure III.2.11 Image of the layout of the circuit.

III.2.5.2 Engraving and soldering

The circuit is fabricated on a double-layered FR4 board. The PCB is engraved with the LPKF ProtoMat 100 and the soldering is done manually. All the selected

components are surface mounted devices (SMD) to minimize the size and the number of vias on the PCB.

III.2.6 Characterization of the circuit

The circuit was characterized by connecting it to one of our CNT-based sensing elements, deformed by the same apparatus described in II.5. The circuit was powered by a battery, according to its design, whereas the voltage reference was provided by a regulated power supply. The digitalization of the output voltage was achieved by the National Instrument NI9212 acquisition system.

III.2.6.1 Deformation

The sensing element was deformed up to $700 \mu\epsilon$, the limit of the linear regime of the sensor. The gain was set at 2500, thus expecting a maximum detectable strain of $800 \mu\epsilon$. Figure III.2.12 shows the result of this characterization and compares it to the simulation results. We can see that the experimental results fit well the simulation results, but the slope of the two curves differs slightly. The two angular coefficients differ of 8.3 %. This can be attributed to a combination of factors and we believe that the predominant causes are the variability of the GF of the sensing element (as described in II.5.2) and the variability of the resistance values that set the gain of the circuit (due to the tolerance of fabrication).

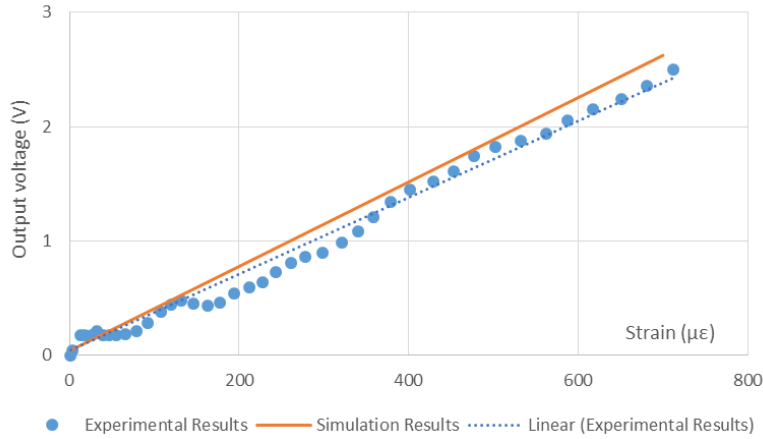


Figure III.2.12 Comparison between experimental and simulation results on a single loading.

Figure III.2.13 shows the characterization for a cyclic deformation. We can see that we can track deformation cycles.

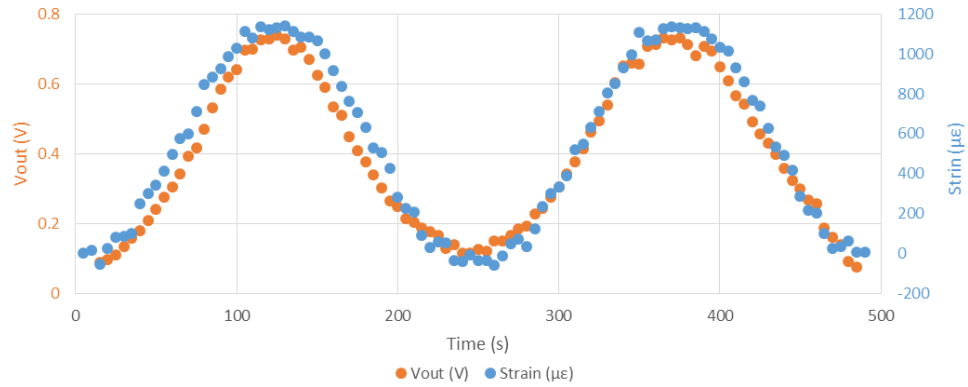


Figure III.2.13 Circuit output compared to input strain.

III.2.6.2 Temperature compensation

We characterized the efficiency in compensating for temperature fluctuations. Our setup, described in II.5.5, allow us to characterize only between 25 and 45 °C. Figure III.2.14 shows the result. We can see that in this 20 °C temperature range, the error introduced on the strain measurement is 2.4 % only. The error introduced by the temperature averages out as 0.12 %/°C, a lesser error compared to the theoretical best result achievable using a Wheatstone bridge-based circuit (see III.2.2). This result demonstrates the validity and the efficiency of this circuit in compensating temperature variations.

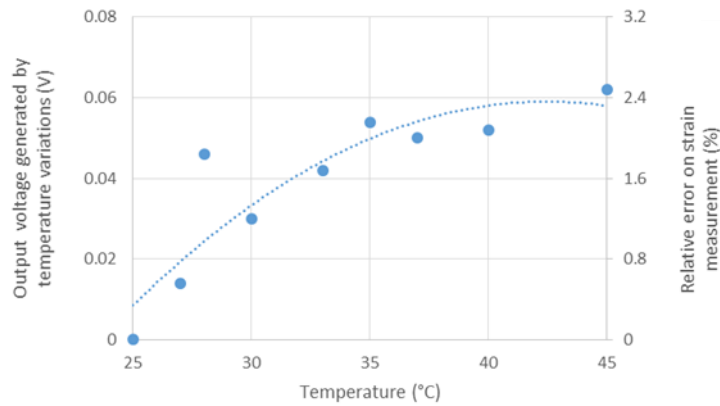


Figure III.2.14 Compensation of the temperature variation between 25 and 45 °C.

III.2.6.3 Power consumption

Since the power consumption of the system is a strong limiting factor in the design of the system, we measured it. The total power consumption of the circuit, including the branch for temperature compensation is $(400 \pm 50) \mu\text{W}$. The power consumption is evaluated by multiplying the power supply voltage by the current injected in the circuit. The ADC is not taken into account in this evaluation since

its power is directly supplied by power harvested by the RFID tag during the communication with the external interrogator.

Compared to the commercial more flexible and tuneable MAX1452 (Maxim Integrated, 2011), our power consumption is more than 200 times smaller.

III.2.7 Perspectives

III.2.7.1 Strong dependence of the output on the voltage reference used as input

As expressed by the formulas in II.6.2 ($V_{out} = Gain \cdot V_{ref}(GF * \varepsilon)$), the output is linearly dependent on the reference voltage.

From this derives the need of a very stable voltage reference. One of the future studies on the circuit will be the comparison of the stability of the SL900A voltage reference pin and a dedicated component.

III.2.7.2 Substitution of the circuit with an ASIC

The use of discrete components in the fabrication is a relatively cheap and versatile option particularly suited for the development phase. For future uses and the commercialization of the product, the option of converting the circuit into an Application Specific Integrated Circuit (ASIC) is interesting for two main reasons.

First, the resulting circuit would be several times smaller, with benefits for both the total size of the device and the interference with the antenna. Smaller size translates into a much smaller coupling between the two parts of the circuit.

Moreover, the power consumption of an ASIC is usually smaller, thus reducing the size of the energy source (a battery or capacitor associated to an energy harvester)

III.3 ANALOG-TO-DIGITAL CONVERSION AND MANAGEMENT OF THE WIRELESS COMMUNICATION PROTOCOL

In the industrial domain, a growing demand of RFID-enabled sensors (Vena, et al., 2014) (Manzari, et al., 2012) (Bhattacharyya, et al., 2011) has motivated the development of integrated circuits that autonomously manage the RFID communication protocol and perform the Analog-to-Digital conversion (ADC) of external sensors.

We chose the SL900A by AMS (AMS, 2013) (see Figure III.3.1), an RFID tag chip with sensor functionalities that can harvest some of the RF field received and powered by batteries for further reading range. The chip has a fully integrated temperature sensor and its external sensor interface provides a way of adding additional sensors to the system and supports up to 2 external sensors (AMS, 2013).

The choice was driven by the versatility of the device; in fact it is the only commercial solution capable of performing the acquisition of two external sensors and a third internal (temperature) sensor. The external sensor front-end can allow us to connect our sensor sensitive to different parameters, such as deformation, humidity and pH.

The ADC is a linear 10-bit converter with selectable voltage references and gains. This allows us to have a measure either of the entire 0-3 V range (the full dynamic being limited by the power supply) with a resolution of roughly 3 mV or a portion of it with a higher resolution.

Moreover, the internal microcontroller can perform multiple measurements and store them in the internal EEPROM memory. This procedure can be used to keep a log of measurements and communicate them only when interrogated by a reader, thus providing more options for duty cycle optimization.

The SPI port may be used in future versions to allow the communication with other digital devices (for example additional ADCs or multiplexers for a greater number of acquisition channels, as well as additional memory banks for higher capacity of data logging).

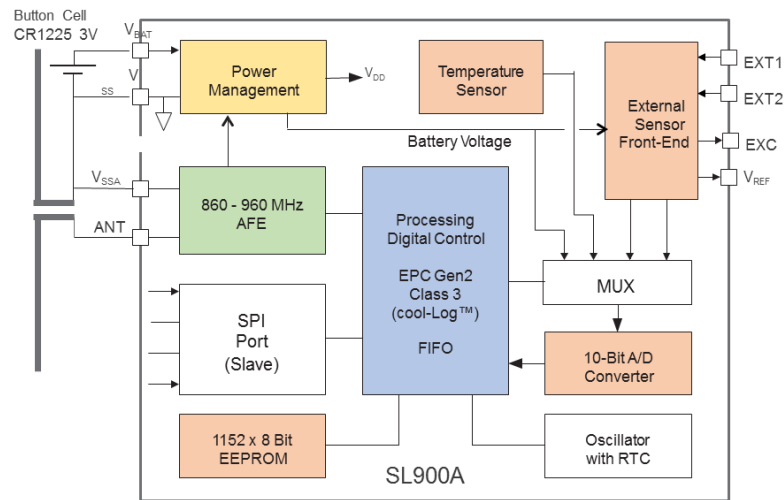


Figure III.3.1 Schematic of the SL900A (adapted from (AMS, 2013)).

III.4 ANTENNA

In this section we briefly describe the development of an antenna specifically designed for the communication through concrete. The conception and the fabrication of this antenna is the result of a fruitful collaboration with Prof Laheurte of ESYCOM – Université Paris-Est and the interns Aladdin Kabalan Houssam Retima.

III.4.1 Goals and constraints

Recent researches demonstrated the feasibility of retrieving information with RFID-enables sensory tags embedded in challenging environment such as soil and concrete (Shams & Ali, 2007) (Jiang, 2011) (Ishida & Furukawa, 2014) (Bauer-Reich, et al., 2014). From these examples and our specific applicative requirements, a few constraints were taken into account in the design of the antenna.

III.4.1.1 Environment of operation

The device is designed to be operative in concrete structures. Concrete has varying electromagnetic properties during the different phases of its life. Because of a varying water content until full maturation, its permittivity and conductivity changes drastically over time (Figure III.4.1). These shifts in conductivity and permittivity modify how the antenna radiates. In particular, it is possible to associate a shift of the resonant frequency of the antenna to the change in permittivity. A modification in conductivity of the medium affects as well the efficiency of the antenna.

III.4.1.2 Size

The size is a key parameter in our application since the smaller the device, the less it introduces discontinuities and fragilities in the concrete structure in which it is embedded. As an indication of the maximum final size of the device, we consider the maximum size of the aggregate normally used in the construction industry. The biggest aggregate used is 1.5 inches (~ 4 cm) (America's Cement Manufacturers, 2015) (University of California - Berkeley, 2015), consequently we assume a maximum size of around 4 cm.

III.4.1.3 Frequency and Bandwidth

The frequency imposed on the communication system affects both the reading range and the size of the system. In fact, for lower frequencies the penetration in concrete is higher and, consequently, we would be able to embed our device at greater depth. On the other hand, the size of the antenna is directly linked to the wavelength of the waves. The communication on the UHF band is a good compromise between the wavelength (and consequently the size of the antenna) and the penetration of waves in concrete (Gopu, 2012). The European Telecommunications Standards Institute (ETSI) EN 302 208 standard, specifies the European RFID UHF range to be 865.6 to 867.6 MHz.

Moreover, from the condition on the permittivity of concrete, the antenna should be relatively wide band to allow for changes in the permittivity and conductivity of concrete that would shift the resonance of the antenna (for instance during drying).

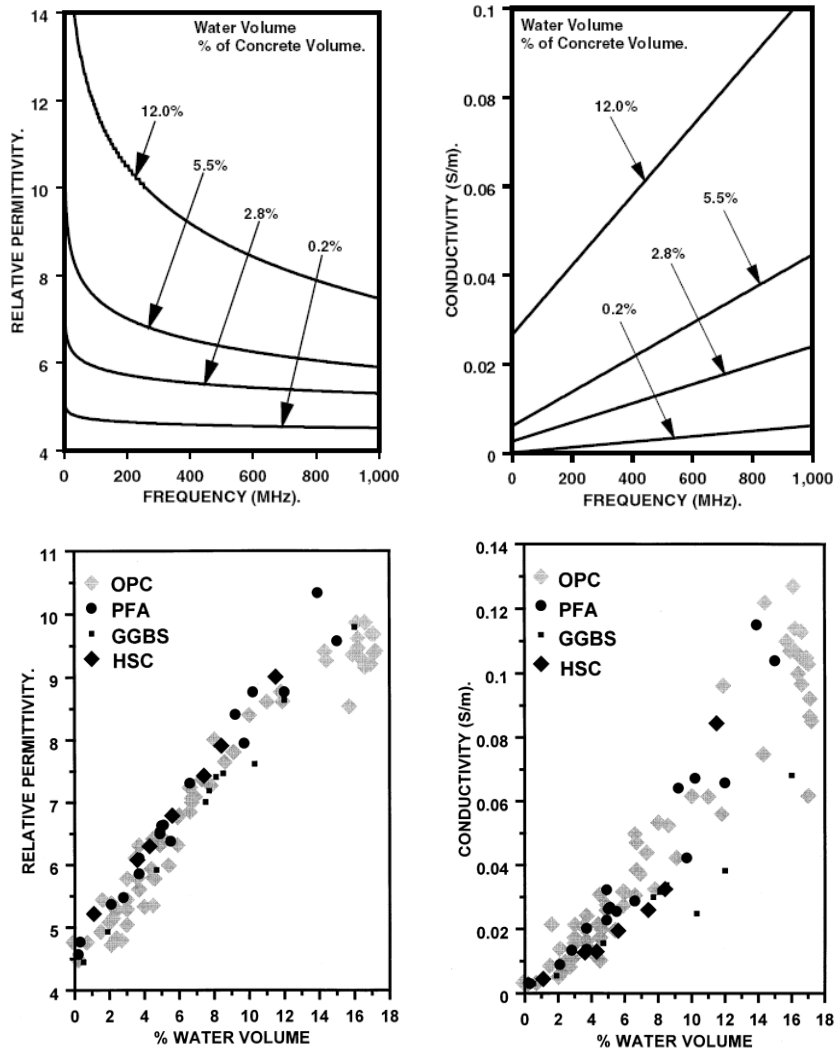


Figure III.4.1 Typical variation of the permittivity and conductivity of concrete. Above, the plots represent the two variables as a function of the frequency and the plots below as a function of the water volume of concrete at 500 MHz (from (Soutsos, et al., 2001))

III.4.1.4 Impedance matching of the antenna with the SL900A

The signal is fed by the integrated circuit SL900A that has an internal complex impedance of $(31 - j320) \Omega$.

In order to deliver the maximum power to the antenna, the reflection coefficient Γ has to be minimized. We know that:

$$\Gamma = \frac{Z_A - Z_S^*}{Z_A + Z_S}$$

where Z_A and Z_S are, respectively, the complex impedance of the antenna and the complex impedance of the source. This expression is minimised for $Z_A = Z_S^*$ (where * indicates the complex conjugate).

This means that the antenna has to be designed to match the real part of the impedance of the SL900A (31Ω) and to show an inductance $L\omega = +320 \Omega$, capable of compensating the equivalent capacitance (imaginary part) of the SL900A.

III.4.1.5 Materials for the fabrication of the antenna

The signal for the antenna is fed by the SL900A, designed to be soldered on a PCB, and the conditioning circuit for the sensors is fabricated on a PCB. Consequently, the most convenient option is to design the antenna on the same circuit board to avoid any out-of-plane connections between different circuit boards.

In this development phase, we decided to develop the system on a dual-sided PCB with copper metallization $35 \mu\text{m}$ thick and FR4 dielectric. This material was easily accessible in ESYCOM laboratories and compatible with engraver LPKF ProtoMat 100. We believe that for future real applications, the FR4 substrate could be substituted with another one with higher permittivity (such as the RO4000® Laminates), thus further reducing the size of the antenna.

III.4.1.6 Short circuits prevention on the SL900A

The SL900A does not provide protection against DC short circuits between the antenna pads. The accumulation of charges between these pads impedes the correct operation of the device. Consequently, any short circuit between the antenna pads should be avoided during design. In particular, the adapter for impedance matching should not be terminated with a short circuit, but with an open one.

III.4.1.7 Insulation of the antenna from the concrete environment

The antenna should be protected from the environment for two main reasons. Firstly, concrete is an aggressive environment that can accelerate the oxidization of the conductive lines of the antenna, thus reducing its performance and functionality. Secondly, the concrete is slightly conductive, as shown by the conductivity plot in Figure III.4.1. A conductive surrounding environment increases the losses of the antenna by generating currents (and consequently heat) in the surrounding of the antenna. Moreover, changes in conductivity of the

surrounding medium can shift the resonant frequency, detuning the designed antenna.

From these considerations, we can conclude that a protective box should be fabricated (see Figure III.4.2). The protective box should not impede the radiation of the antenna, be strong enough to withstand the load applied to the concrete structure and be compatible with concrete. For this prototype Teflon® was selected as the optimal choice for its high resistance to high pH and its relatively high strength.

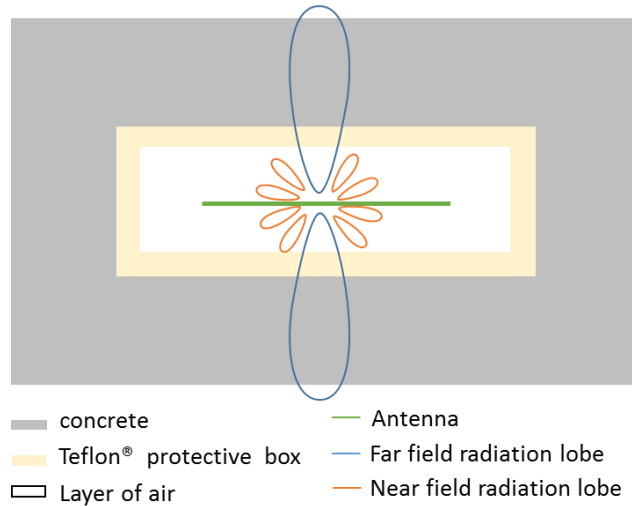


Figure III.4.2 Cross section of the device embedded in concrete.

The Teflon box and the layer of air within the box should introduce a spatial separation between the antenna and the concrete environment large enough to minimise the parasitic currents generated in concrete by the near-field side lobes. Moreover, a physical separation of the antenna from the medium can decrease the sensitivity of the resonant frequency of the antenna over the changes of conductivity of concrete.

For this project, a separation of 5 mm between the antenna and the protective box was selected. The thickness of the box was imposed to be 2 mm to preserve mechanical strength. Further studies are required to optimise optimize these values.

III.4.2 Design of the antenna

III.4.2.1 Antenna configuration

From the discussion in the previous paragraph about the maximum size and the interest in developing the antenna on the same PCB than the circuit, the meander line antenna (MLA) (Figure III.4.3) is the optimal choice. In fact, this type of antenna, widely used in the field of RFID tags, does not require any additional ground plane and allows us to reduce considerably the size of the final antenna compared to classical dipole antennas.

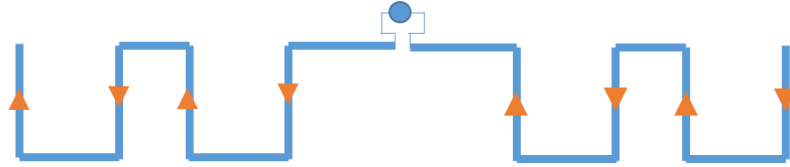


Figure III.4.3 Schematic of a meander line antenna (MLA). The orange arrows show the orientation of the current in the antenna.

In MLAs, a classic dipole is folded back and forth several times on its characteristic length. The action of folding helps decreasing the size, but it reduces the antenna performance. Without diving into the details of MLA design, which is outside the scope of this chapter, it is important to remind the main parameters and physical constraints taken into account during the design of our antenna to better understand the choices that led to the current layout.

Firstly, in MLA, the sections of the antenna actively participating in the radiations are the horizontal ones of Figure III.4.3. In fact, from the orange arrows representing the current orientation in the antenna, we can see that the vertical parts on the meanders are in opposition, thus cancelling each other. From this consideration, the only contribution to the radiation resistance is given solely by the horizontal segments, while the vertical ones contribute to the losses of the antenna. This affects the efficiency of the antenna (defined as the ratio of the received power that is actually radiated), whose formulation is $\eta = \frac{R_{\text{radiation}}}{R_{\text{radiation}} + R_{\text{losses}}}$. If only the horizontal segments participate to the radiation (and consequently they represent the sole contributions to $R_{\text{radiation}}$), we can see that we have to **compromise between the size reduction and the efficiency of the antenna**.

Secondly, **the size reduction of the antenna decreases its bandwidth**. In fact, the vertical segments introduce an inductive component to the antenna. Some inductance is needed to minimize the reflection coefficient Γ previously introduced. On the other hand, if the size of the antenna is reduced excessively, the inductance introduced is too big to be cancelled out by the internal capacitance of the SL900A. A high reactance stores a great amount of the energy received instead of radiating it. This retention of energy increases the Quality factor (Q) defined as:

$Q = 2\pi \frac{\text{Energy stored}}{\text{Energy radiated}}$. In turn, the bandwidth (BW) is inversely proportional to Q ($B \sim 1/Q$). Consequently, we can see that we have to compromise between the size

of the antenna and its bandwidth. Thus, in the selection of the appropriate size of the antenna, we have to take into account our constraint on the bandwidth to be large enough to allow changes in the permittivity of concrete.

III.4.2.2 Proposed design

In Figure III.4.4 we show the proposed design. The spatial distribution of the meanders is the result of an iterative algorithm implemented in HFSS aimed at finding the optimal configuration in the area assigned for the antenna.

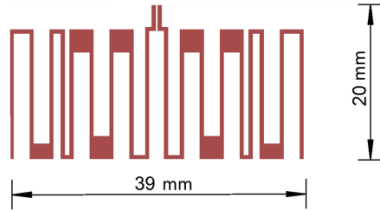


Figure III.4.4 Schematic of the proposed design of the antenna.

The software HFSS simulates the antenna to extract its efficiency over a specified frequency range. Since the relative permittivity of concrete varies between 5 and 8, several simulations are performed to check that the BW of the antenna is sufficiently wide to still be able to communicate. Figure III.4.5 shows the shift of the resonant frequency for different values of permittivity. From the efficiency of the antenna, the mismatch of impedances between the tag and the antenna, and the radiation pattern (function of the frequency), the reading range is evaluated by HFSS simulations. We can see that the antenna is well tuned and sufficiently wide band to accommodate the modifications to the resonance condition introduced by the change in permittivity of concrete (the values of permittivity used are the ones provided by (Soutsos, et al., 2001)). We clarify that the reading range is the maximum distance from the surface of the concrete at which the interrogator can be put without breaking the wireless connection with the tag, embedded in concrete at a depth of 4 cm.

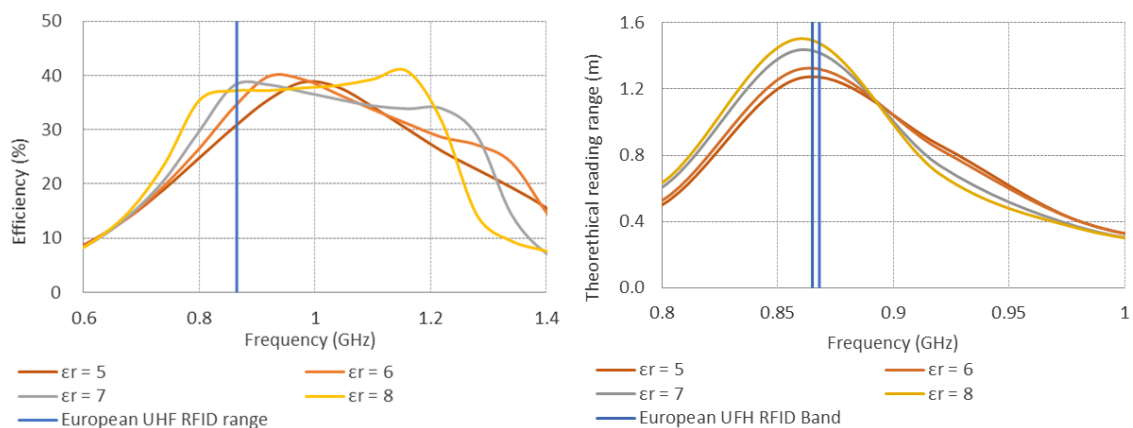


Figure III.4.5 Efficiency and theoretical reading range of the antenna as a function of the frequency and permittivity of concrete. Results obtained by numerical simulation using the software HFSS (values of permittivity taken from (Soutsos, et al., 2001)).

As previously discussed, the conductivity of concrete affects the efficiency of the antenna. For higher conductivity, a greater portion of the electromagnetic field is lost in creating currents inside concrete. As a consequence, the reading range decreases for higher values of conductivity (σ) as shown in Figure III.4.6.

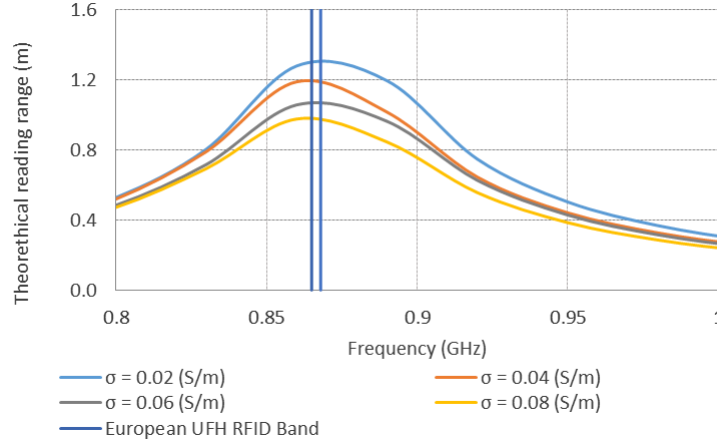


Figure III.4.6 Decrease of theoretical reading range as a function the conductivity of concrete (values of conductivity taken from (Soutsos, et al., 2001))..

In order to prove that the protective box is effective in reducing the influence of concrete on the operation of the antenna, the antenna is simulated with a thinner protective box. This time, the Teflon® is directly in contact with the antenna and no air cavity is left around the antenna. The performance of the antenna in this second case are much more dependent on the concrete conditions, as shown in Figure III.4.7. This result proves that a bigger protective box is highly beneficial for the improvement of the overall performance of the antenna

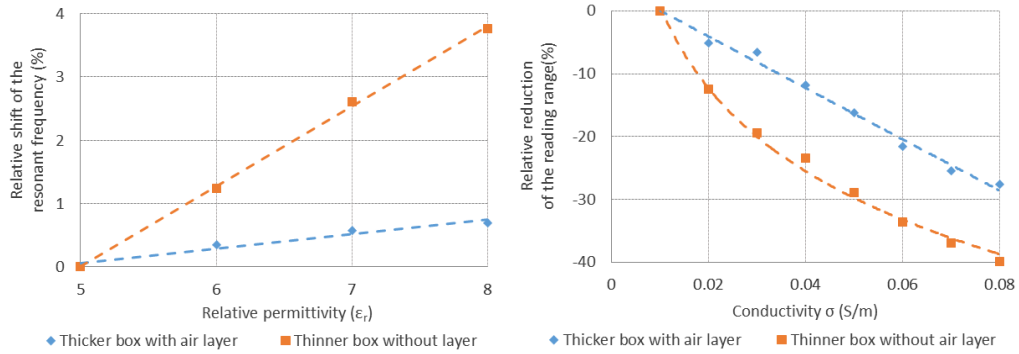


Figure III.4.7 Comparison between the performances of the antenna when protected by a thin box (without any air gap between the antenna and the Teflon® box) or a thicker box (with 5 mm air gap between the antenna and the box). On the left, we can see that the resonant frequency of the antenna protected by the thinner box is much more sensitive to the changes in permittivity. Similarly, when the antenna is protected by a thin box, its reading range decreases more rapidly when the conductivity is increased.

In Figure III.4.7 we introduce the “relative shift of resonant frequency” and the “relative reduction of the reading range”. They are calculated as follows:

$$\text{Relative shift of Resonant Frequency}|_{\varepsilon_r} = \frac{ResFreq_{\varepsilon_r=x} - ResFreq_{\varepsilon_r=5}}{ResFreq_{\varepsilon_r=5}} * 100$$

where $ResFreq_{\varepsilon_r=x}$ indicates the frequency for which the antenna has the maximum reading range for a particular value of permittivity ε_r of the surrounding concrete.

$$\begin{aligned} &\text{Relative reduction of the reading range}|_{\sigma_r} \\ &= \frac{\max(\text{reading range})_{\sigma=x} - \max(\text{reading range})_{\sigma=0.01}}{\max(\text{reading range})_{\sigma=0.01}} * 100 \end{aligned}$$

where $\max(\text{reading range})_{\sigma=x}$ indicates the maximum reading range for a particular value of conductivity σ (expressed in S/m) of the surrounding concrete.

III.5 ASSEMBLY OF THE SYSTEM

In this section, we present the fabrication of the system and the assembly of the different parts.

III.5.1 Components to be assembled

Figure III.5.1 graphically summarises the structure of the final device. The entire device is fabricated on a single PCB (engraved with the LPKF ProtoMat 100). The sensing elements are connected to the circuit by thin insulated copper wires soldered to specific pads designed on the PCB.

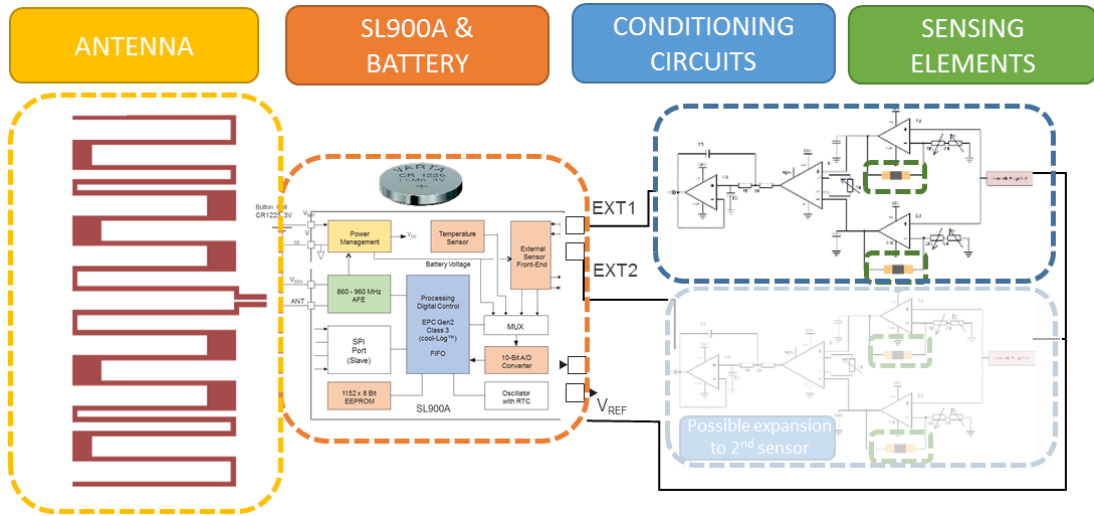


Figure III.5.1 Schematic of the final device in which we highlight the different parts previously discussed.

III.5.2 Assembly

The components are manually soldered in place. Figure III.5.2 shows the soldered device.

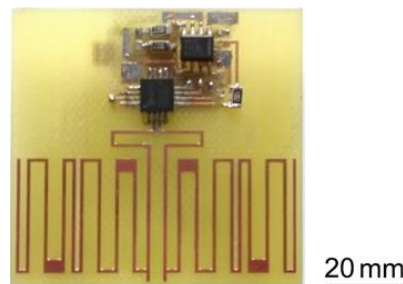


Figure III.5.2 Assembled RFID tag.

We noticed that the quality of the connection was not always optimal, especially for the connection to the SL900A. For future development, we believe that using an oven for soldering is the optimal solution. The reflow techniques ensure better contacting and, in addition, the temperature profile during soldering is specifically

designed to minimise the thermal shocks and potential damages to the electronic components.

III.5.3 Protection for embedded applications

For the use in concrete, the device has to be protected. Because of the different heights and electromagnetic rationales of the components (see Section III.4.1.1 for more information) and because greater protection toward shocks and rough environment is preferable, we chose not to protect our device with a simple protective film, but with a rigid box, despite its bigger size.

We selected the Polytetrafluoroethylene (PTFE and better known as Teflon). This polymer is well known for its high compatibility to high pH and consequently well suited to the concrete environment.

Figure III.5.3 shows the box fabricated for the second version of the device.

The total volume of the device is 43 cm^3 , a volume comparable to the aggregates used in the construction industry (America's Cement Manufacturers, 2015).

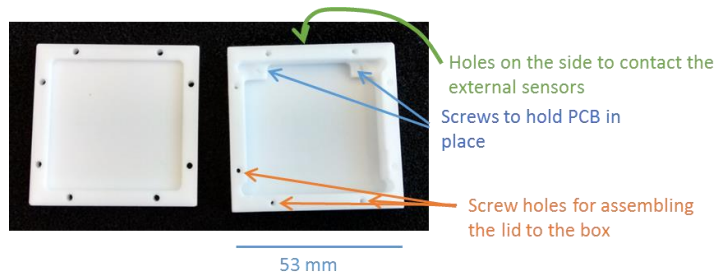


Figure III.5.3 Protective Teflon box. On the left of the image, we can see the lid and on the right is the box where the circuit is hold. Both the lid and the box present evident recesses; these are made to ensure a 5 mm air gap between the antenna and the protective box. The sensors need to be exposed to the concrete environment for proper operation. We can see in the image that the box has an opening on its side for the passage of the wires connecting the sensors exposed to the outside world to the circuit protected inside the box. This opening is sealed with silicone to guarantee a closed and protected environment to the circuit.

III.6 TESTS IN MORTAR

In order to test the possibility of retrieving the information from inside cementitious material, the fully assembled device is embedded in a 2-litre mould of mortar (Figure III.6.1).

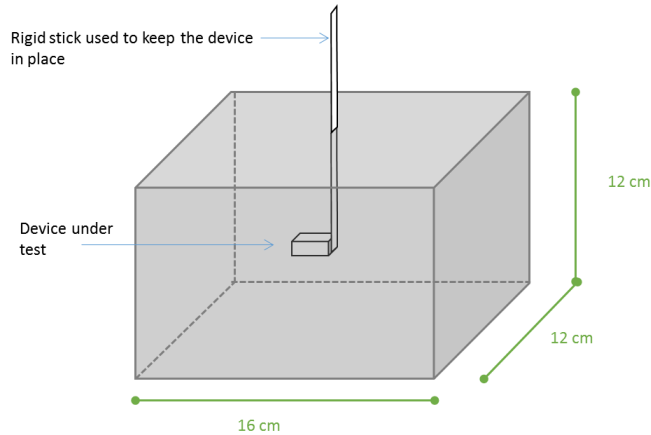


Figure III.6.1 Schematic of the test of the mortar block with the prototype embedded in it. The device is placed centrally in the mortar block and kept in place by a rigid polymeric stick glued to a side of the device.

During pouring and hardening the device is kept at a depth of 5 cm. The device is constantly read during the phase of pouring and hardening to ensure that the communication link is maintained. Figure III.6.2 shows the instrumentation used during the test.

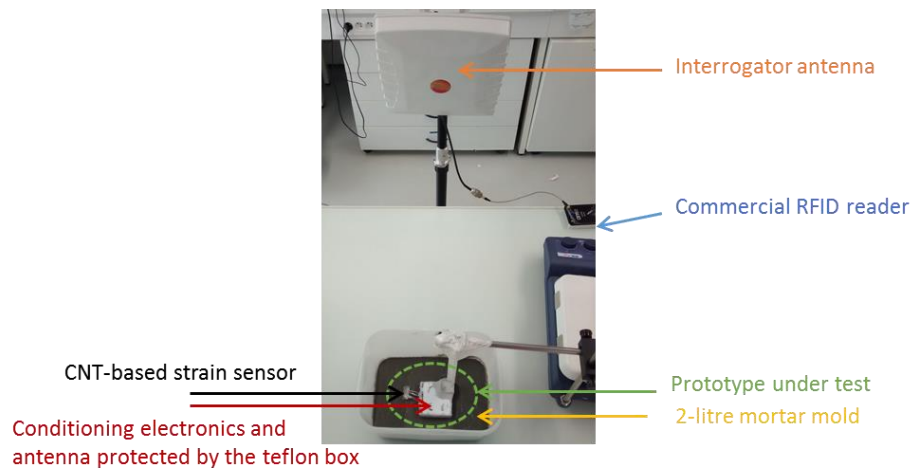


Figure III.6.2 Prototype under test. The device is positioned in the middle of a 2-litre mould of mortar. In the picture, we can see that the device is progressively covered with concrete to ensure that no damage is inflicted to the external sensor. During pouring and the hardening phase, the device was constantly interrogated to control if the wireless communication was ensured.

The reading range of the device is evaluated in the range 800-1000 MHz, as shown in Figure III.6.3.

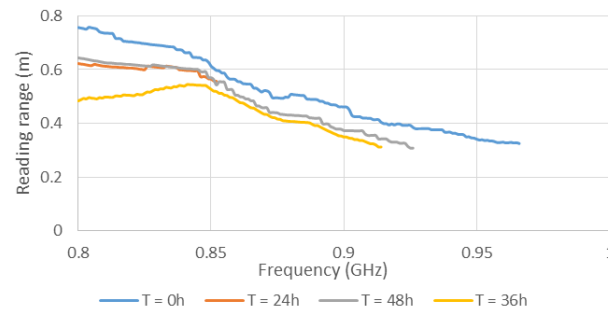


Figure III.6.3 Reading range of the device embedded in mortar in the frequency range 800-1000 MHz. The evolution of the reading range is shown at different time intervals after the sensor is embedded in mortar (time reference indicated as T=0h).

We can see that the device can be read during the hardening process. Nevertheless, the experimental results are different from the simulation results in three main areas:

- the resonant frequency,
- the reduced reading range,
- the reduction of the reading range associated to the drying process.

The resonant frequency should have been centred at 860 MHz, but from the plot we can infer that the resonant frequency is lower than 800 MHz (our instrumentation doesn't allow us to investigate the response of RFID tags for frequencies lower than 800 MHz). This can be due to a variety of factors, among which:

- a permittivity of mortar different from the one expected,
- a difference in the geometry of the protective box or the mortar block between the simulation and the experimental conditions,
- a mismatch between the impedances of the SL900A and the antenna,
- a coupling with the conditioning circuit more important than the one simulated.

III.7 PERSPECTIVES

III.7.1 Antenna optimisation

The antenna is one of the essential bricks of the proposed sensor because it ensures the communication of the readings to the outside of the structure.

As previously discussed, the protective box is designed to leave an air gap between the antenna and the concrete environment to improve the antenna performance. A systematic study will address the optimisation of this box. The study will aim at finding the optimal shape to ensure a good compromise between the size and the performance.

Moreover, since the experimental results differ significantly from the simulation results, both in terms of reading range and in terms of resonant frequency, a campaign of test will be organised. This campaign is aimed at finding the reasons of the discrepancy between simulation and experimental results as well as at proposing modification to ensure an optimal performance in the European UHF range.

Enhancing the reading range is important because it indicates that only one antenna can survey a section of a structure, interrogating several sensors at one time (Figure III.7.1).



Figure III.7.1 Survey of a section of a concrete structure by using only one interrogator antenna (picture adapted from (Jansen, 2011)).

One additional possibility to investigate is the separation of the antenna and the circuit with a ground plane. This solution would decrease the coupling with the circuit ensuring more stable performances and would increase the gain of the antenna. On the other hand, the size required to build such new antenna is higher, consequently a compromise should be found.

III.7.2 Energy harvesting

The current version of the device is partly powered by the power received from the interrogator outside the concrete structure (passive operation of the SL900A), but the vast majority of the capabilities of the designed systems are powered by the embedded battery. We believe that for the future development of the device, an energy harvesting is highly desirable.

The use of an energy harvester is interesting for two reasons. Firstly, it harvests the power needed for the operation of the circuit, thus guaranteeing a longer life-time of the embedded device. Secondly, it reduces the size of the circuit by eliminating the need for a battery.

The energy harvesting technique most suited for the application seems to be the electro-magnetic energy harvesting. Several commercial and research solutions are available to achieve energy harvesting in the UHF band (Arrawatia, et al., 2011) (Taris, et al., 2012) (De Donno, et al., 2013). The size of these solutions can be as little as 14 mm x 14 mm (PowerCast, 2015).

The energy is stored in a capacitor. The stored energy is a function of the capacity of the capacitor according to the formula hereafter:

$$\text{Stored Energy} = \frac{1}{2} \text{Capacity} * \text{Voltage}^2$$

From this formula we can calculate the required capacity of the capacitor. We know that:

- the power consumption of the circuit is around 400 μW ,
- the SL900A has 2 external inputs and we want to have information on multiple parameters of the concrete environment, consequently we assume that we use 2 circuits at the same time,
- we estimate a need to power the system for 0.5 s in order to perform several measurements and average them out.

From these assumptions, we conclude that the required energy stored in the capacitor is:

$$\text{Required Energy} = \text{Power Consumption} * 2 \text{ circuits} * \text{ON Time} = 400 \mu\text{J}$$

The required capacity is then:

$$\text{Capacity} = 2 \frac{\text{Required Energy}}{\text{Voltage}^2} \approx 250 \mu\text{F}$$

As comparison with the battery currently used (12 mm radius), the capacitor needed to store such amount of energy is 7 mm x 4 mm x 2 mm (the capacitor selected is the Panasonic EEF-CX0G221XR).

In conclusion, energy harvesting techniques are a viable option in terms of the size required for their implementation and, moreover, could guarantee a longer lasting energy supply to the embedded system.

III.8 CONCLUSIONS

We developed the electronic platform necessary to decode, digitize and communicate the sensor's output.

The circuit's power consumption is only 400 μW , more than 200 times less than commercial circuits (such as the MAX1452 (Maxim Integrated, 2011)) and shows a reduced size (2 cm^2). It is fully adapted to the detection of small resistive changes in the sensing element as a consequence of applied micrometric deformations.

The antenna is specifically optimized for the communication through concrete and its size is sufficiently small to be embedded in concrete. The price of the miniaturization is the decrease in bandwidth of the antenna, but, according to the simulations, it is still sufficient to accommodate some variability in the environmental conditions that cause a shift of the resonant frequency. Some further work is required in this area to better tune the antenna on the European UHF band.

The protective case demonstrated to be adapted to shelter the device from harmful infiltrations and ensure the operation of the device in aggressive environments.

We demonstrated the performance of the device embedded 6 cm deep into mortar. The reading range is sufficient to envision the use of only one reader to survey multiple embedded sensors at one time, in order to acquire precise information of a portion of a structure at a reduced cost.

The total volume of the device is 43 cm^3 , a volume comparable to the aggregates used in the construction industry (America's Cement Manufacturers, 2015).

For all these reasons, we believe that the device developed is fully adapted to the embedded SHM of concrete structures.

PART IV.

VALIDATION OF THE SOLUTION THROUGH APPLICATION

PART IV.

VALIDATION OF THE SOLUTION THROUGH APPLICATION

In this section, we describe the tests ran in mortar and concrete in order to validate the effectiveness of the devices for in-situ applications. A few prototypes were developed in order to test different aspects of the developed system.

Firstly, the sensing element was tested in a mortar slab under controlled environment. The slab was subject to bending and the output of the sensing element recorded. The test was oriented to the identification of the effectiveness of the sensing element in detecting deformation when embedded in cementitious materials. We compare the result of surface and embedded detection of deformation in order to further demonstrate the effectiveness of embedded structural monitoring compared to surface monitoring.

Secondly, the device was embedded into an outdoor experiment in the first SenseCity experimentation. The devices were buried into a 5 m x 5 m x 0.15 m concrete slab, the concrete foundation of a wooden chalet. This test was designed to prove the compatibility of the device to concrete environment for longer periods and in real-scale outdoor structures. We demonstrate the possibility of tracking the cyclic micrometric deformation of a concrete structure induced by temperature variations. Moreover, we demonstrate the possibility of retrieving the information wirelessly from within the structure.

IV.1 OPERATION IN MORTAR

The first tests were conducted in laboratory environment for greater control over the experimental conditions.

IV.1.1 Methodology

IV.1.1.1 Fabrication

For the mortar fabrication, the NF EN 196-1 norm is followed in order to have results comparable with the literature and a repeatable fabrication process. Figure IV.1.1 shows the steps for the fabrication of the test slabs.

Three parallelepipedic slabs are fabricated:

- the first one without sensor,
- the second one only with one sensing element located at the very centre of the slab (on the neutral axis/plane),
- the third one with 2 sensing elements, one central and one located 22 mm away from the first one along the slab longest dimension.

Before any test, the specimens are dried for 150 days.

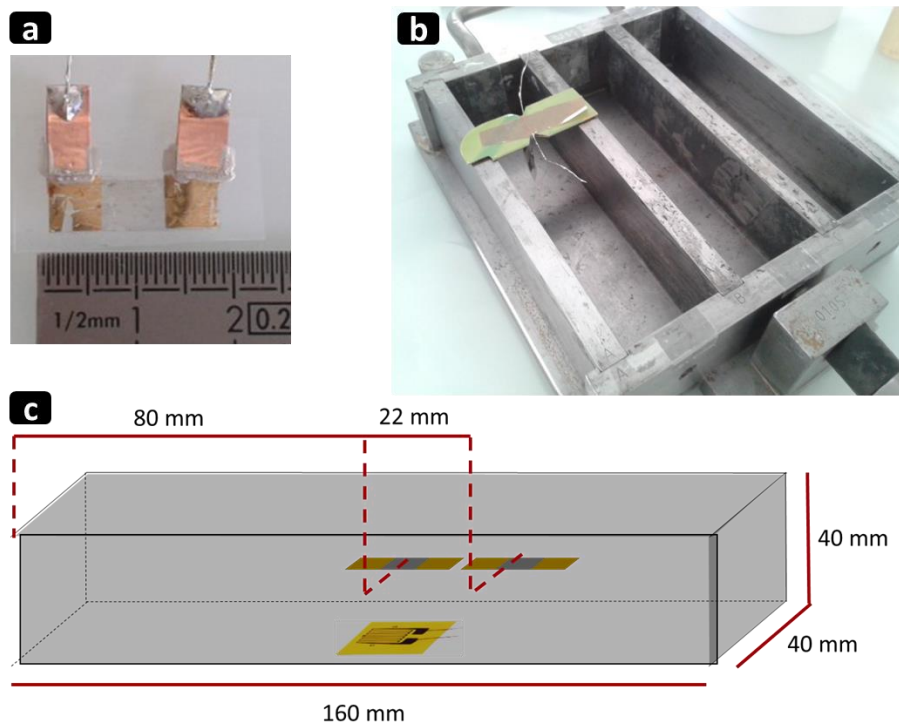


Figure IV.1.1 Fabrication process of the mortar slab with embedded sensor. a) electrical contacting to the sensor is ensured by wired attached to the golden electrodes by silver paste. The CNT network and the electrodes are consequently protected by a thin insulating layer of SU8. b) the sensor is fixed in position within a metallic mould. The mortar is then poured into the mould. The mould is covered with plastic film to avoid a too rapid drying process. After 24 h, the specimen is extracted from the mould, wrapped into plastic sheets and left to dry for additional 150 days. c) schematic of a test slab. Three specimens were fabricated. One without sensors embedded, one with only a central sensor embedded,

one with two sensors (one in the middle and one 22 mm on a side). A Kethley 2612B is used for resistive measurements.

IV.1.1.2 Deformation of the test slabs

A 3-point flexural test is performed on the mortar slab. The loading point is shown on Figure IV.1.3. Firstly, we want to identify if the presence of the sensing element decreased the strength of the test slab. Secondly, we analyse the output of the embedded sensors.

During the tests, a commercial metallic strain gauge (10 mm long) was glued on the bottom surface of the test slab in order to have data on the external deformation.

All slabs were deformed by application of a load on the central point with a universal testing machine Instron 4486. The machine controls the downward displacement of the top flexural point and the force applied was measured during all the test. The slabs were loaded until complete fracture occurred.

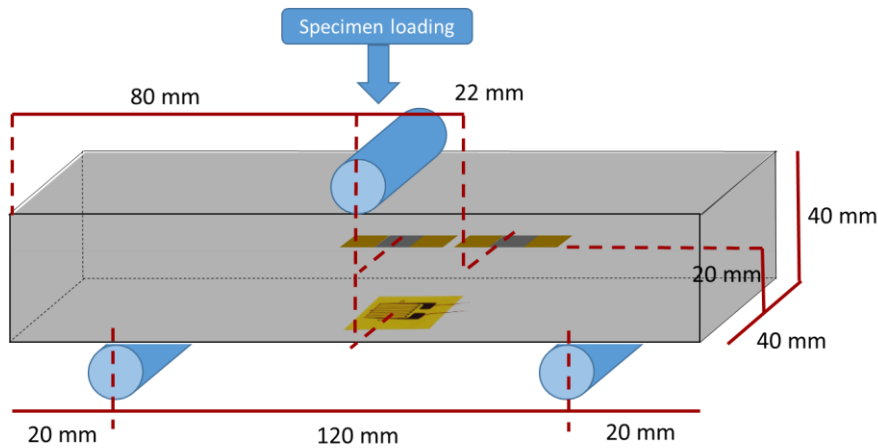


Figure IV.1.2 Structure of the mortar specimen under test.

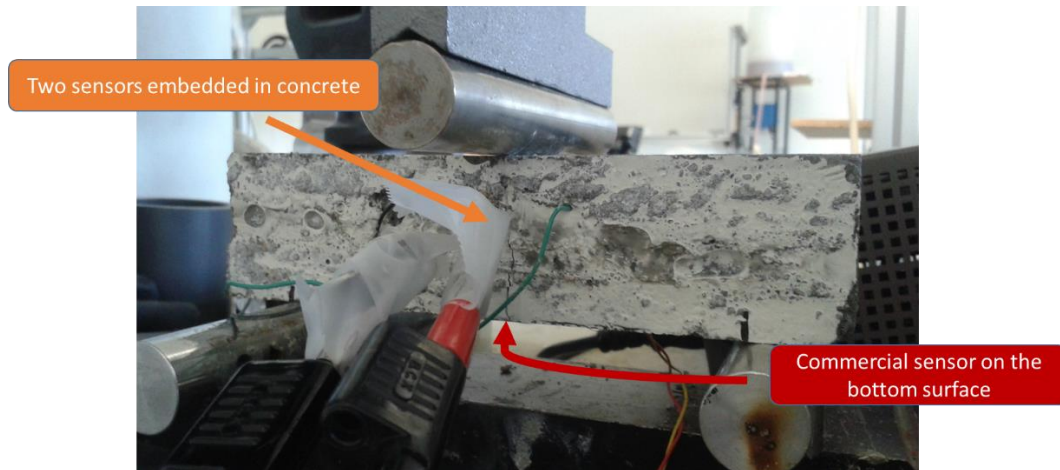


Figure IV.1.3 3-point flexural tests. Above, a schematic showing the test. Below, an image taken during the actual characterization. We can see the mortar slab, the electrical connections and the loading points. The adhesive tape around the electrical wire is to provide electrical insulation and ensure separation between the different electrodes during the test.

IV.1.2 Results

IV.1.2.1 Strength of the test slab

We compared the maximum force experienced by the three slabs at the moment of failure. From this, the flexural strength was calculated by

$$\sigma = \frac{3FL}{2bd^2}$$

where F is the force at the fracture point (N) L is the length of the support span (120 mm), b and d are respectively the width and the thickness of the slab (both 40 mm). Figure IV.1.4 summarises the results. We can see that the presence of the sensing element strongly influences the strength. We can see that the decrease in flexural strength is around 30% of the original value. We believe that the decrease in flexural strength is caused by the introduction of a smooth discontinuity in the slab that decreases internal cohesion and represents a slippage surface. The width of the sensor represents 38 % of the width of the mortar slab. We are currently fabricating new sensing element of different sizes and shapes that will be tested in the future to see if the influence on the flexural strength can be minimized.

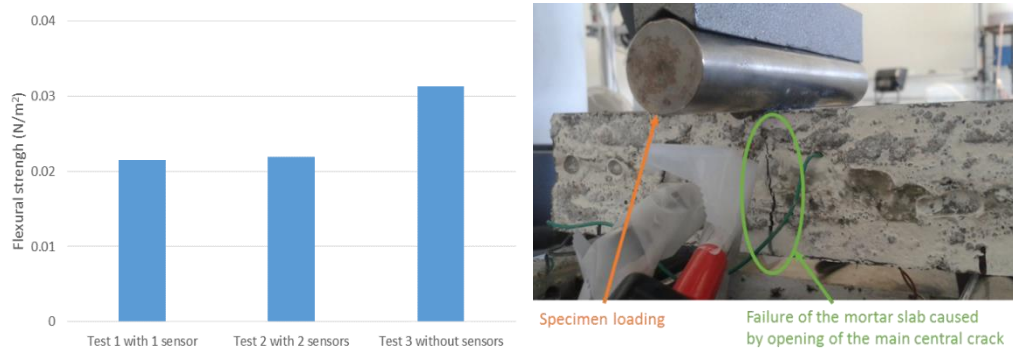


Figure IV.1.4 On the left, the comparison of the flexural strength for the three slabs. On the right, an image of the failure of the mortar slab caused by the opening of the main central crack.

IV.1.2.2 Detection of deformation

Figure IV.1.5 shows the relationship between downward displacement of the top flexural point and the measured force.

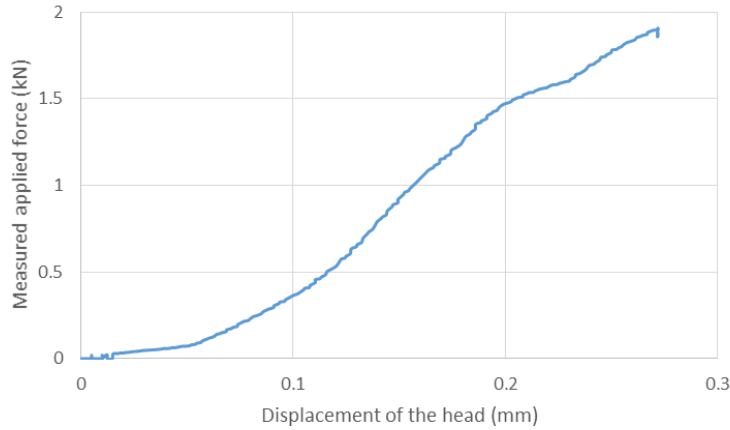


Figure IV.1.5 Relationship between the downward displacement of the top flexural point and the generated force. The curve ends when the failure occurred.

The external deformation observed by the commercial metallic strain gauge seems linear dependent on the force applied to the slab, as shown in Figure IV.1.6. The failure of the slab causes the resistance of the strain gauge to become infinite.

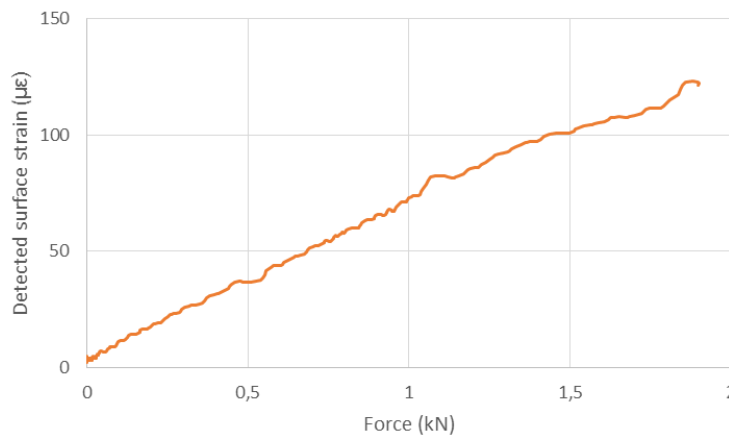


Figure IV.1.6 Relationship between the force applied on the mortar slab and the strain measured on the bottom surface of the sample by the commercial metallic strain gauge.

The sensors inside the mortar slab show a completely different behaviour (see Figure IV.1.7).

Since all the three embedded sensors demonstrated a similar behaviour, we believe that these results are not due to measurement errors but, on the other hand, to some physical modification applied to the sensing element.

Firstly, the embedded sensors are positioned on the neutral axis of the mortar slab, thus, the expected strain measured by the internal sensors should be almost zero since it is positioned on the neutral axis. On the other hand, the change in

resistance of the device (around 1 %) suggests a deformation of 10000 $\mu\epsilon$, two orders of magnitude bigger than the strain detected by the external sensor. This suggests that the sensors are not only monitoring the strain.

Moreover, the resistance change does not vary uniformly with the applied force. The increment is discrete until final rupture occurs. In the characterization with two sensors embedded in the slab, we can observe a clear delay between the central sensor and the one on its side.

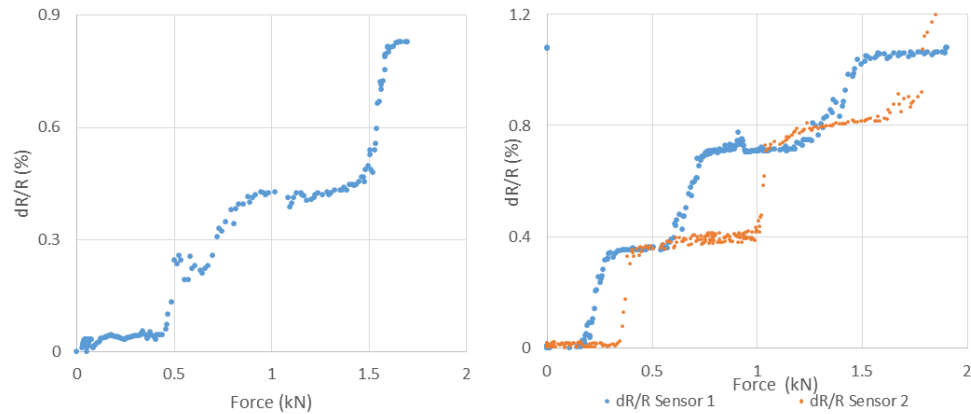


Figure IV.1.7 Change of resistance induced by the deformation applied on the mortar slab. On the left, the result of the 3-point bending test with only one sensor embedded in the mortar slab. On the right, the result for two embedded sensors (Sensor 1 is placed at the centre of the slab and Sensor 2 is 22 mm on its side).

We hypothesise three possible causes to interpret this result:

- degradation of the contacts between the wire and the sensing element,
- delamination at the interface concrete/sensing element during deformation,
- opening of micro cracks.

The degradation of contacts could explain an increase in resistance, but it is difficult to associate all the observed phenomena to this cause. In fact, we believe that after degradation of the contacts, the signal should be noisier. Moreover we could not interpret the nearly constant height of the step as well as the delay between the two sensors in the characterization with two sensors embedded.

In delamination, the sensor loses contact totally or partially with the material. Since the curvature is larger for the sensor positioned on a side, we would expect a greater change for this sensor than the one positioned in the centre. Moreover, by losing contact with the material, the sensors should experience a contraction, with consequent reduction of the resistance, more than a sudden increase of resistance. For these reasons, we believe that the delamination hypothesis can be discarded.

The opening of micro cracks could explain all the observed phenomena. Several works focusing on the modelling of creep formation in cementitious materials (concrete and mortar) (Bazant & Oh, 1983) (Hsu, 1984) (Bazant, 1988) (Van Zijl, 2000) (Muttoni & Ruiz, 2005) (Hilaire, et al., 2013), suggested that the opening of cracks does not follow a single straight line, but a band of tortuous micro cracks

(see Figure IV.1.8). It has been proved that cementitious materials start to develop micro fractures in their interior parts from 20-25 % of the ultimate load (Hsu, 1984) (Rossi, et al., 2012). The tortuosity of the micro cracks is directly linked to the quantity and size of aggregates.

The micro cracks in the vicinity of the sensing element might induce an elongation of few μm localised on a small portion of the device, thus explaining the discrete increment of the resistance (Figure IV.1.8).

Micro cracks open first at the most stressed location. In the 3-point bending configuration, it is underneath the point of application of the load. Hence cracks should appear first here and other cracks only later when at locations away from the centre (Figure IV.1.8). This is consistent with the delays observed on the curves.

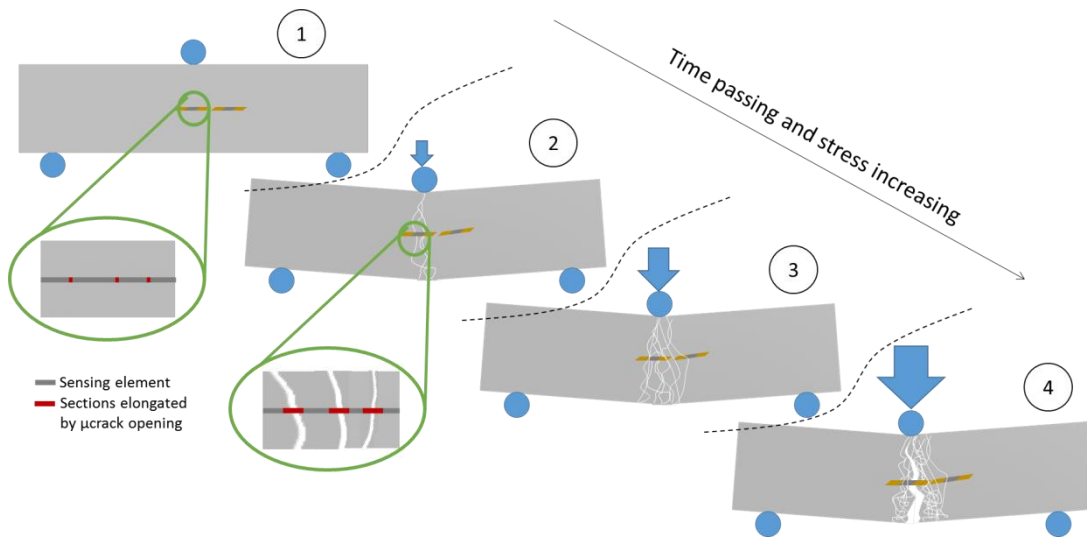


Figure IV.1.8 Band model of crack opening in concrete and mortar. At rest (Stage 1 of the schematic), the sensors are at initial length and the mortar is not deformed. For increasing loading, the mortar slab starts to deform. For stresses higher than 20-25 % of the ultimate load, micro cracks start to open, causing a local deformation of the sensors (Stage 2). Increasing the load, the band of the micro cracks expands toward the extremities, eventually reaching the second sensor (Stage 3). When the ultimate load is reached, a central macro crack originates on the bottom surface and expands all the way through the mortar slab (Stage 4).

IV.1.3 Conclusions and future work

The experimental data on the 3-point flexural behaviour of mortar slabs monitored by embedded CNT-based strain gauge suggests the possibility of detecting micro fractures induced by the load applied onto the specimen.

In order to validate the hypothesis that the resistance steps in the sensing element's resistance are caused by the opening of micro cracks, further tests are necessary. It is important to combine acoustic and/or optical characterizations to the deformation in order to correlate the sensing element's reading with the observation of the opening of new micro cracks.

Another possibility is to saw a cross section of a deformed mortar slab in order to optically characterize the distribution of micro cracks inside the specimen.

Moreover, the experiment shows a clear decrease in robustness of the mortar slab as a consequence of the presence of the sensors. In future characterizations, is it important to understand how to minimise the impact of the sensors on the structure itself.

If the capability of detecting micro cracks is confirmed, the sensor should be tested for the detection of micro cracks generated by drying shrinkage. As seen in Section I, the detection of micro cracks generated by drying shrinkage is an essential parameter to predict structural deficiencies accelerated by higher permeability of cementitious materials.

IV.2 OPERATION IN CONCRETE

Extensive outdoor tests are conducted in the **sense^{CITY}** (IFSTTAR, 2015) project, a scientific “miniature city” that recreates a realistic urban environment for testing micro and nano sensors. **sense^{CITY}** aims at facilitating urban applications of nanotechnologies and in this project, 25 sensors are embedded in the concrete foundations of one of the smart house of the “miniature city” (Figure IV.2.1).



Figure IV.2.1 The first installation of the the **sense^{CITY}** project, a scientific “miniature city” that recreates a realistic urban environment for testing micro and nano sensors.

IV.2.1 Methodology

A variety of sensors are embedded in concrete:

- 10 CNT-based strain gauges,
- 11 commercial metallic strain gauges used to compare the results obtained with the CNT-based sensors
- 4 temperature and humidity sensors for additional characterization of environmental conditions

It is important to note that the commercial metallic strain gauges selected for this test are low-cost foil strain gauges; no embeddable vibrating wire strain gauge is used in this test. As discussed in Section I, the embeddable vibrating wire strain gauges are bulky and expensive; here we want to investigate the possibility of detecting micrometric deformation with low cost devices, hence the choice of low-cost foil strain gauges.

IV.2.1.1 Choice of sensors

The CNT-based strain gauges are the one fabricated by our group and described in detail in Section II.

The commercial metallic strain gauges are primarily selected for their compliance to concrete environment (according to their datasheets). Secondly, a selection of geometries and sizes are chosen to identify the best suited shape for the detection of micrometric deformation in concrete. The majority of devices exploited in the experiment are of similar size of the CNT-based strain sensor to better compare the

results. Figure IV.2.2 shows a summary of the strain gauges employed in this experiment.

Brand	Sokki kenkyuko			RS	
Model	FRG-3	PL-100S	PR-20-11	N11FA812011	N11MA212023
Nominal Resistance (Ω)	120	300	120	120	120
Gauge Factor	2,1	2,12	2,08	2,1	2,0
Gauge length (mm)	3	100	20	8	2
Quantity employed	1	2	1	5	2

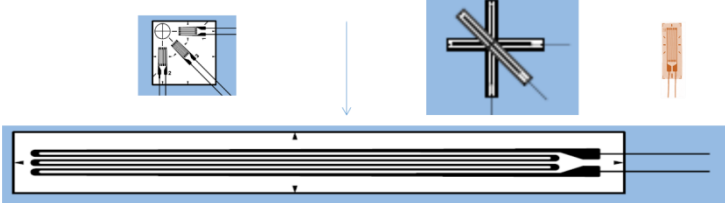


Figure IV.2.2 Summary of the commercial metallic strain gauges used in this experience. The images at the bottom, represent the shape of the different sensors.

The selected temperature and humidity sensor is the Sensirion SHT75, known to work well with concrete environment (tested at IFSTTAR and CEREMA in previous unpublished work). We chose this integrated temperature and humidity sensor because it directly provides the digitized information on the two parameters of interest with a precision of 1.8 %.

IV.2.1.2 Protection

To protect the embedded sensors for their operation in the aggressive environment of concrete different techniques are followed.

For the CNT-based strain gauges, a thin layer of SU8 (epoxy resin) is deposited on the CNT network in order to provide protection and insulation from the environment. The deposition of this thin film ensures a good stability of the resistive measurement over changes in pH and humidity of the environment.

The commercial strain gauges are embedded as purchased. No modifications are introduced in order to better compare our devices to the commercial ones.

The temperature and humidity sensors are packaged to prevent direct contact of the sensor with the environment (especially during the first phase of pouring, concrete is wet and it would destroy this type of sensor). For this reason, a conic protection was fabricated by 3D printing. The sensor is inserted into the conic structure that acts as a protective chamber; the aperture of the structure is covered by a GoreTex® sheet that ensures a passage of humidity between the environment and the sensor chamber but not water; finally, the whole structure is protected and insulated by a thin silicone layer (see Figure IV.2.3). The GoreTex® membrane is not covered by silicone to ensure passage of humidity through it.

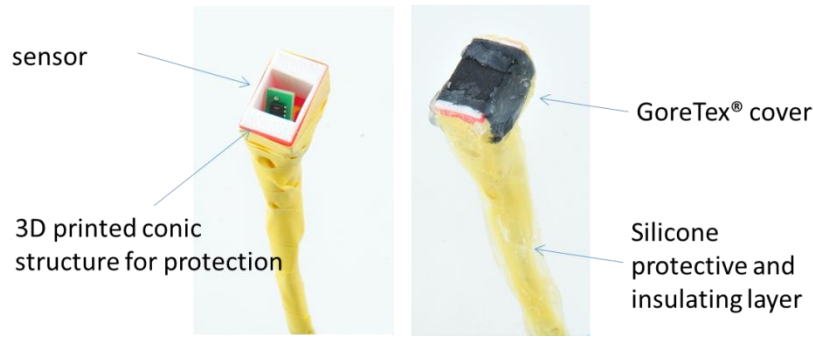


Figure IV.2.3 Protection for the temperature and humidity sensor.

IV.2.1.3 Conditioning and positioning

In order to be sensitive to mechanical deformations, we attached two wedges on either side of the sensor as shown in Figure IV.2.4. Both commercial and CNT-based sensor are conditioned this way. Two sensors are attached to a rigid substrate to discern behaviors caused by environmental conditions.



Figure IV.2.4 Preparation of the strain gauge to ensure the transmission of the deformation from the concrete matrix to the embedded sensor.

The concrete slab in which the sensors are embedded is 13 cm thick. The sensors are positioned at different depth in the concrete slab. The sensors are kept in place by a plastic shaft anchored to the ground (Figure IV.2.5)

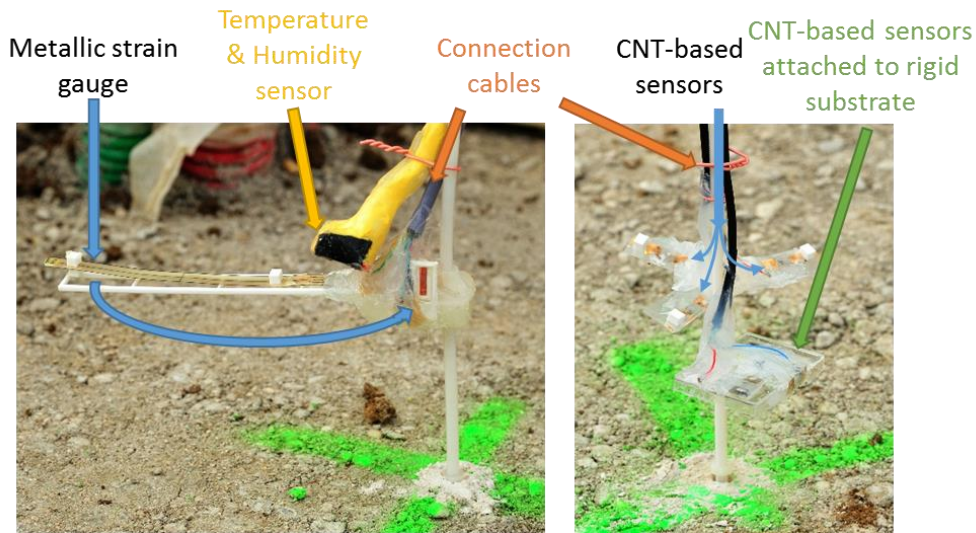


Figure IV.2.5 Positioning of sensor prior concrete pouring. The sensors are positioned at different heights and kept in place by a plastic shaft anchored to the ground

IV.2.1.4 Conditioning

Since the wireless architecture proposed in the previous sections is still manually soldered and its fabrication takes a lot of time, the sensors are connected to the outside world by cables. Consequently, all piezoresistive sensors are measured with a Wheatstone bridge in half-bridge configuration. All the cables used in this experiment are coaxial cables to reduce the ambient electromagnetic noise.

Only one wireless platform is fabricated for validation of communication through concrete. The wireless platform is embedded in concrete at a depth of 3 cm.



Figure IV.2.6 Embedded wireless platform

The temperature and humidity sensor require an RJ45 cable for data communication.

IV.2.1.5 Concrete pouring

Concrete is poured in small quantities close to the sensor; the concrete is then manually positioned all around the sensors to ensure that no damage is caused to them.

After all the sensors are carefully covered, the remaining part of the slab is filled with concrete.

Finally, the surface of the poured concrete is smoothed.

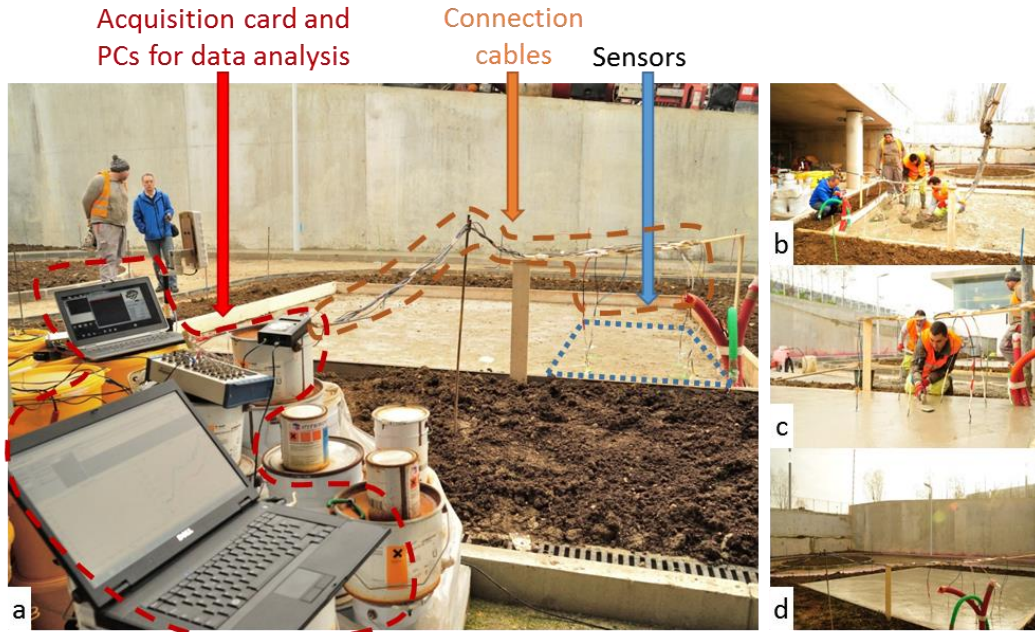


Figure IV.2.7 Phase of concrete pouring. a) All sensors are in place and ready to be embedded. We can see the cable connections to the acquisition card and the computers for continuous measurement. b) Concrete is manually positioned around the sensors to ensure that no damage is caused to them. c) The surface of the poured concrete is smoothed. d) The concrete slab after the process. We can see the cables exiting the surface of the concrete.

IV.2.2 Results

IV.2.2.1 Wireless communication

The reading range of the wireless communication was measured for 30 days from the moment the concrete was poured.

The measurement is performed using the same equipment at all time (see Figure IV.2.8). The reading range remained (50 ± 5) cm during the entire period. No significant change was observed with the decrease of water content of concrete. The antenna connected to the interrogator has a gain of (6.4 ± 0.1) dBi at 865-868 MHz (European UHF RFID slot). For longer reading ranges, antennas with higher gain should be used.

Is it important to notice that the experiment is performed on an early prototype of the wireless system. The more recent prototype described in III.3 has higher performance, consequently the reading range should be higher or, in turn, the sensor could be embedded deeper in concrete. Tests are scheduled for the end July 2015.

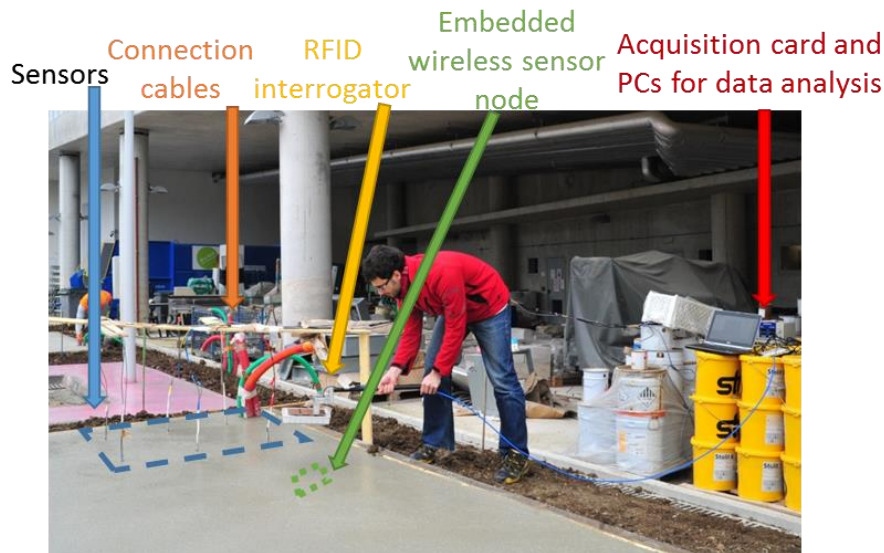


Figure IV.2.8 Wireless interrogation of the embedded sensor in concrete.

IV.2.2.2 Early age concrete

During the first 72 hours, concrete is known to harden and loose a great mass of water. We characterized the concrete in this period; unfortunately, our acquisition system stopped working for several hours, thus leaving a gap in our data. Despite this, we present some preliminary results.

After pouring, the temperature was in the range (12 ± 3) °C (see Figure IV.2.9). We can see that the temperature influences the “control sensors”, that is to say the sensors that are glued to a rigid substrate. The commercial metallic strain gauge and the CNT-based one show different range of resistance variation that can be attributed to different temperature sensitivities.

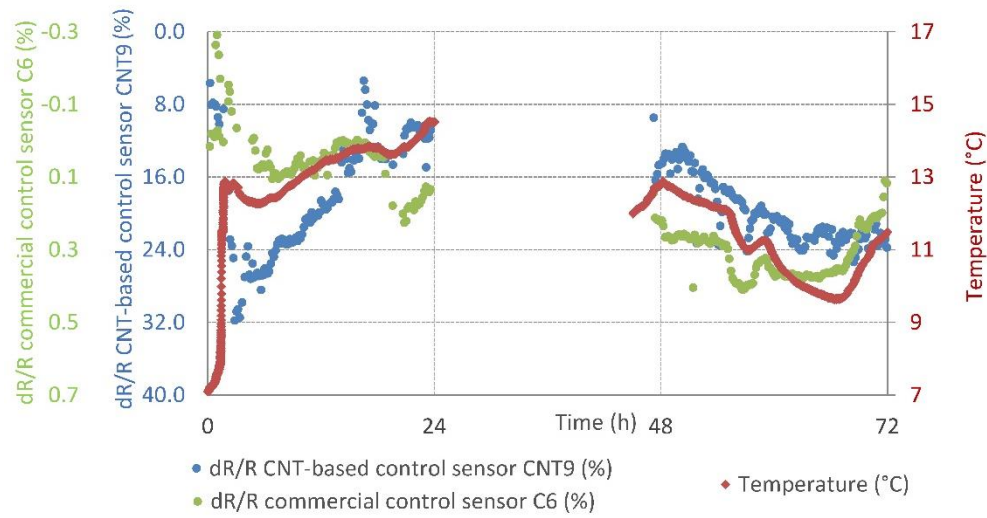


Figure IV.2.9 In red, internal temperature measured by the embedded temperature sensor. In green and blue, the resistance variation of, respectively, the commercial control sensor and the CNT-based one.

The outputs of the sensors that are free to be deformed inside concrete show a range of variation several orders of magnitude higher than the control sensors (see Figure IV.2.10 and Figure IV.2.11). In the plots we show two results per sensor type (commercial and CNT-based) which are representative of the results obtained by each group of sensors.

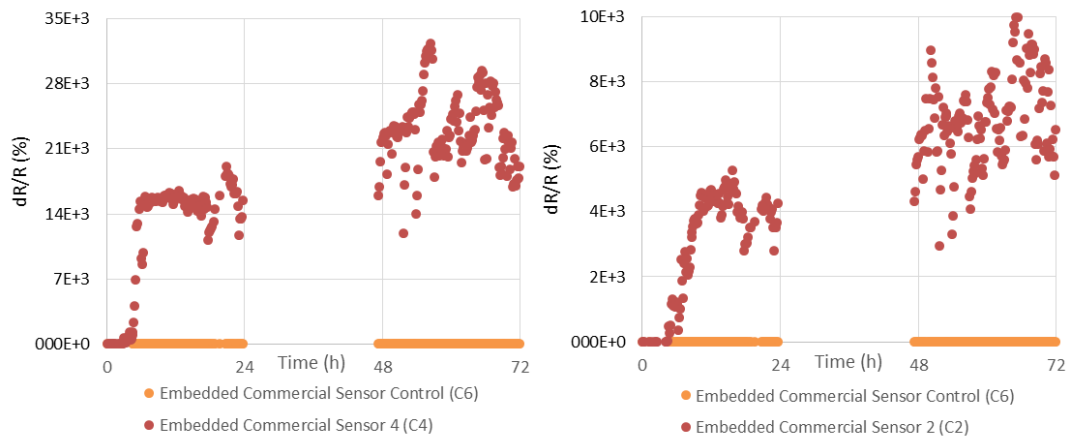


Figure IV.2.10 Variation of the resistance of two commercial strain gauges compared to the control sensor. The variation of the commercial devices is several orders of magnitude higher than the variation of the control sensor (see Figure IV.2.9 for the detail plot of the control sensor).

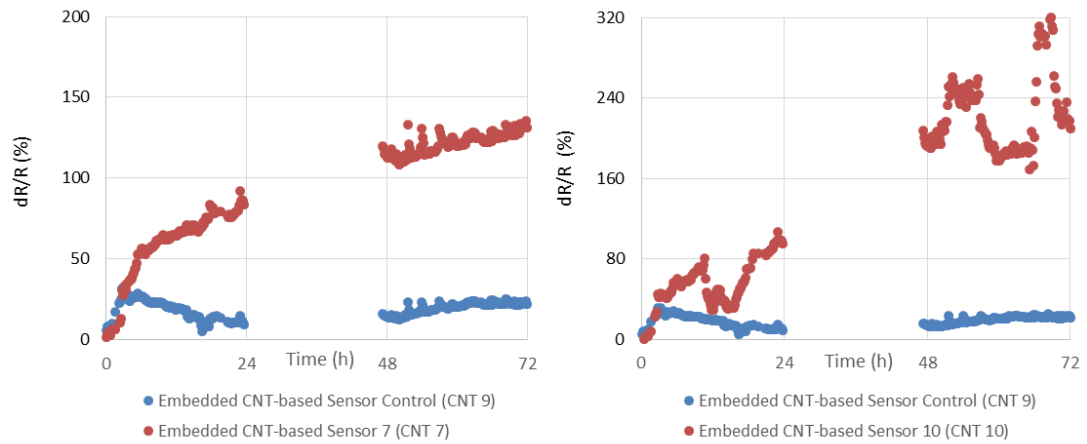


Figure IV.2.11 Variation of the resistance of two CNT-based strain gauges compared to the control sensor. The variation of the commercial devices is roughly two orders of magnitude higher than the variation of the control sensor (see Figure IV.2.9 for the detail plot of the control sensor).

These results suggest that during hardening of concrete, some intense mechanical deformation is applied to the sensors free to be deformed.

Nevertheless additional tests are necessary to analyse this phenomenon.

IV.2.2.3 Durability of the embedded sensors

The number of sensors still operational is evaluated six months after pouring concrete. CNT-based sensors show a survival rate significantly higher than that of the commercial ones (see Figure IV.2.12). We tend to exclude that the difference in survival rate is due to the cable connection to the acquisition card. The connections are made in the same way and the same connection cables are used for the experiment. This result can be interpreted as a higher compliance to the harsh environment of concrete of the CNT-based sensors.

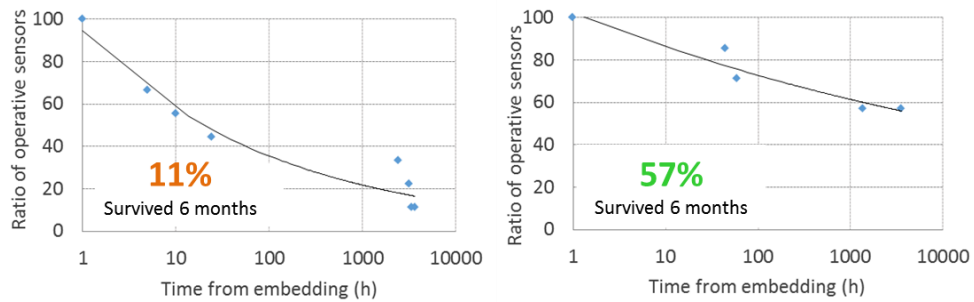


Figure IV.2.12 Comparison of the survival rate of commercial strain gauges (on the left) and CNT-based ones (on the right) after six months of operation in concrete.

IV.2.2.4 Temperature in concrete

With the temperature sensor embedded in concrete we can study how the internal temperature of concrete is affected by the outside temperature (see Figure IV.2.13). We observe a regular delay of roughly 4 hours between the outside temperature fluctuations and the internal ones. Moreover, the temperature inside

concrete are smoothed, consequently the range of variation is decreased considerably.

At the time of this characterization, the wooden chalet covered the concrete foundation, thus preventing direct sunlight. Moreover, no significant change in temperature is observed by the temperature sensors positioned at different heights within the concrete slab.

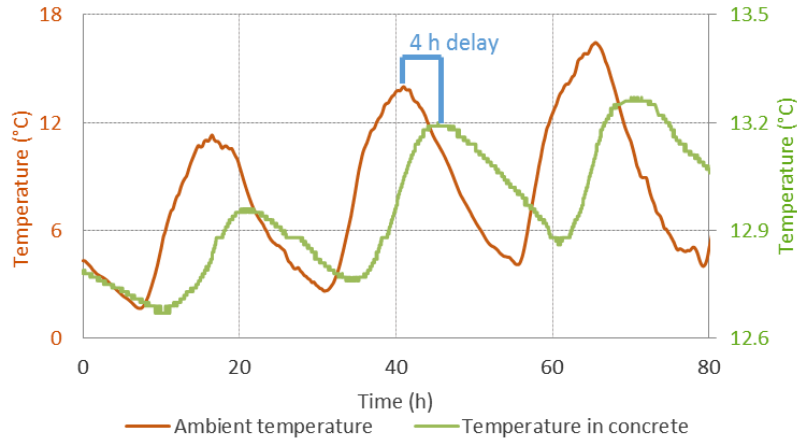


Figure IV.2.13 Comparison between internal temperature in concrete and external temperature.

Thanks to the embedded temperature sensor that provides the internal temperature of concrete, it is possible to estimate the thermally-induced expansion of the concrete slab. The scientific literature suggests values of the coefficient of thermal expansion ranging from 8 to 14 (Meyers, 1951) (Kada, et al., 2002) (Sellevold & Bjøntegaard, 2006). As an approximation, we assume the thermal expansion coefficient of the hardened concrete of this experiment equal to $10 * 10^{-6} \text{ }^{\circ}\text{C}^{-1}$. (The Engineering Toolbox, 2015)

The expected thermal-induced strain is then equal to:

$$\frac{dL}{L} = 10 * 10^{-6} * \frac{dT}{T}$$

This value can then be compared with the strain detected by the embedded sensors. In the following paragraphs, we show such comparison for a period ranging from 3 days to a week.

For our calculations, we take the minimum temperature registered in the period as the reference temperature.

IV.2.2.5 Detection of thermally-induced strain with commercial sensors

Figure IV.2.14 shows the comparison between the expected thermally-induced strain and the strain measured by a commercial strain gauge.

The light green shaded area around the green curve represents the error associated with the measurement (given by the distributor (Radiospare, 2008)). We can see

how the expected strain is contained in this area, suggesting that the strain gauge is able of detecting the thermally-induced strain in concrete.

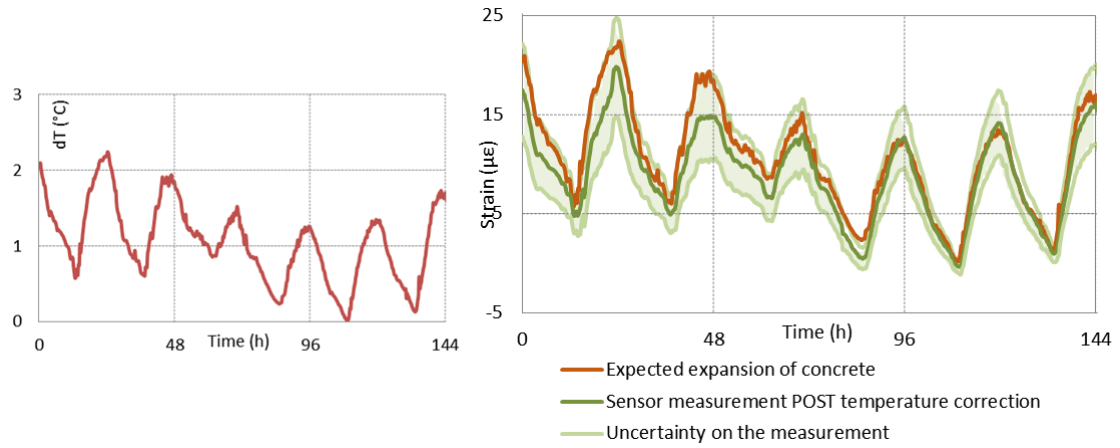


Figure IV.2.14 On the left, the plot of the internal temperature of concrete. On the right, the comparison between the expected thermally-induced strain and the strain measured by the commercial strain gauge. The expected thermally-induced strain is always contained in the uncertainty range around the measurement.

IV.2.2.6 Detection of thermally-induced deformation with CNT-based sensors

A similar result can be obtained with the CNT-based strain gauges. Figure IV.2.15 shows the results. In this case we cannot plot the uncertainty associated with the measure.

We can see that the sensor readings are noisier than the results presented in the previous paragraph. For this reason the identification of the thermally-induced strain can only be achieved on shorter periods.

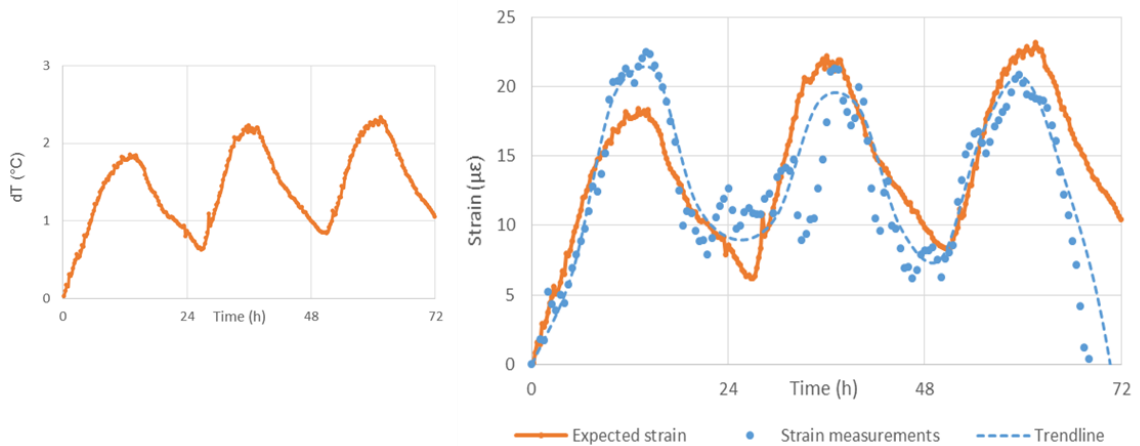


Figure IV.2.15 On the left, the plot of the internal temperature of concrete. On the right, the comparison between the expected thermally-induced strain and the strain measured by the CNT-based strain gauge.

IV.2.3 Conclusions

The **sense^{CITY}** experimentation platform offered the possibility of testing the sensing element as well as the wireless device in realistic conditions and to compare the results with commercially available low cost solutions.

During hardening the sensors share a similar output, which motivates us to believe that they are sensing some deformation phenomena. Further characterizations are needed to interpret this preliminary result.

During the operation in concrete, the CNT-based sensors showed a higher compatibility to harsh environment, confirming our hypothesis that our sensors are suited for embedded concrete monitoring.

In fully dried concrete, we manage to observe thermal-induced micrometric deformation, the conclusive proof that the system is capable of detecting micrometric deformations and compatible to multiple stresses induced by temperature fluctuations.

This work represents the first report of micrometric deformation monitoring by using nano sensor nodes. What is more, the device was tested in realistic conditions, showing the great potential of this innovation and the readiness of this technology for real applications.

PART V.

CONCLUSIONS AND PRESPECTIVES

PART V.

CONCLUSIONS AND PRESPECTIVES

Goals

This work aimed at providing a cost-effective technique for the in-situ detection of micro scale defects at the core of concrete structures for the anticipation of structural deficiencies and, ultimately, a safer and more sustainable construction industry.

We intended to achieve this goal by the introduction of an innovative low-cost, fully functional wireless nano sensor node adapted for the detection of micro deformations inside concrete.

Synthesis of results

First, we built a flexible and robust sensing element capable of precisely detecting micro deformations. We relied on the well-known piezoresistive properties of CNT networks to fabricate a flexible strain sensor by inkjet deposition of MWCNTs on ETFE. We demonstrated the precision, the remarkable cyclability and the hysteresis-free operation of the sensor in laboratory conditions, with the possibility of compensating for temperature fluctuations. The thorough optimisation of the fabrication process opened the doors to the serial fabrication of the devices with low variability in resistance, gauge factor, and temperature sensitivity. The possibility of batch producing the sensor and the use of low-cost materials ensure the cost effectiveness of the sensing element in the long term. Moreover, the sensing element demonstrates good sensitivity and selectivity to other parameters such as pH, temperature and humidity, a clue that leads us to believe that the device can provide a customizable base for the production of a multipurpose sensing element.

Secondly, we proved the capability of the proposed nano strain sensor to detect micrometric deformation in cementitious materials. We first proved it by observing the behaviour of mortar slabs monitored by embedded CNT sensors under 3-point flexural tests in laboratory conditions. In this experiment we link an evident piezoresistive response of the device to the opening of cracks caused by deformation of the slab. The additional evidence that the device is capable observing micro deformations in real-life concrete structures was achieved in the **sense^{CITY}** experimentation platform. In this experiment, the sensing elements were tested in realistic conditions and we observed micrometric deformations of the concrete expanding due to rising temperatures. Moreover, the presented nano sensors show higher durability compared to commercially available low-cost strain gauges, further justifying the interest in the development of this technology for embedded SHM.

Finally, the communication of the measurements from the core of the structure toward the end user is ensured by an electronic platform specifically designed to

decode, digitize and communicate the sensor's output in the harsh environment of concrete. The condition circuit consumes 200 times less than commercial circuits with the same purpose and has a reduced size (2 cm^2). It is fully adapted to the detection of small resistive changes in the sensing element caused by micrometric deformations while it compensates for temperature fluctuations. The antenna is specifically optimized for communication through concrete and its size is sufficiently small to be embedded in concrete. The choice of the RFID protocol ensures an efficient communication even in crowded environments, opening the road to the mass deployment of this technology in real structures. The protective case was shown to be well adapted to shelter the device from harmful infiltrations and ensure the operation of the device in aggressive environments.

The capability of the designed system of communicating embedded measurements was demonstrated for nodes embedded 6 cm deep into mortar. The total volume of the device is 43 cm^3 , a volume comparable to the aggregates used in the construction industry (America's Cement Manufacturers, 2015).

Analysis and Perspectives

This work constitutes the first report on the embedded detection of micrometric deformation of concrete by nano wireless sensor nodes and establishes a new paradigm in embedded sensing for SHM. The use of nanotechnologies in wireless sensor nodes for the detection of micro deformations inside concrete represents an innovation with the potential of providing the first low-cost technology adapted for mass deployment in SHM.

In addition, we significantly contributed to the development of a highly reproducible fabrication process of printed CNT sensors, sensitive to a variety of stimuli (pH, humidity, strain and temperature).

The extended capabilities of the sensing element and the adaptability of the designed circuit provide a new toolset to the SHM community for the volume detection of anomalies at a micro scale. Moreover, thanks to the variety of the parameters detectable by the system, this device can respond to the need of other field of research, such as water quality monitoring.

Finally, the small-size and fully functioning prototype demonstrates the readiness of this technology for industrialization.

PART VI.

APPENDIXES

PART VI.

APPENDIXES

VI.1 APPENDIX I – OPTIMISATION OF THE FABRICATION PROCESS OF THE CNT-BASED

VI.1.1 Preliminary test to optimize the fabrication of the CNT sensor

Being a complex procedure several preliminary test were run to optimize the different phases of fabrication. This section provides the information on the definition and optimization of the fabrication steps.

VI.1.1.1 Ink fabrication

Our goal is to deposit the CNTs via inkjet deposition. Consequently, CNTs are dispersed in a liquid solvent. The literature offers a wide selection of techniques for CNT dispersion in a liquid solvent. Two main approaches can be identified: the dispersion in water with the help of surfactants and the dispersion in organic solvent.

Both approaches are pursued. The MWCNTs are dispersed in solvent using an ultrasonic probe (Bioblock Scientific VibraCell 75043) operated at 150 W for 20 min followed by centrifugation at 10 kG for 4 h. The multi-walled carbon nanotubes (MWCNTs) are Graphistrenth C100 from Arkema.

The table below summarizes all the tested solutions for CNT dispersion. The colour of the solution is used as a qualitative evaluation of the quantity CNTs dispersed in the solvent after centrifugation. The assessment on the conductivity was performed on a drop of solution deposited onto a silicon substrate and cured at 60°C. Silver paste was used to achieve good electrical contact and the conductivity was tested by a Keithley 4200-SCS. All devices with a sheet resistance higher than 10 GΩ was considered as not conductive.

Solvent	Surfactant	Concentration of CNTs (wt.%)	Concentration of surfactants (wt.%)	Colour	Conductive	Notes
Chlorobenzene		0.05		light grey	NO	Lower conductivity than inks based on Dichlorobenzene
		0.1		Grey	YES	
		0.2		Grey	YES	
		0.5		Grey	YES	
Chlorobenzene	SDBS	0.05	1	light grey	NO	No evident sign of improvement over plain Chlorobenzene
		0.1	1	Grey	YES	
1,2 Dichlorobenzene		0.01		Grey	YES	
		0.02		Black	YES	

		0.05		Black	YES	
1,2 Dichlorobenzene	SDBS	0.01	1	Grey	YES	No evident sign of improvement over plain Dichlorobenzene
N,N-dimethyl formamide		0.05		Transparent	NO	no sign of dispersion
		0.2		Transparent	NO	
		1		Transparent	NO	
Acetone		1		Transparent	NO	no sign of dispersion
Isopropanol		1		Transparent	NO	no sign of dispersion
Water	SDBS	0.1	0.01	light grey	NO	Bundled CNTs prevent the ink from being printed
		0.1	0.1	Grey	NO	
		1	0.01	Grey	NO	
		1	0.05	Black	YES	
		1	0.1	Black	YES	
Water	Nafion	0.1	0.1	Transparent	NO	no sign of dispersion
		0.1	1	Transparent	NO	
		1	1	Transparent	NO	

Table VI.1.1 Table showing the different test run to identify the best solvent to disperse CNT in a liquid solution. The solution chosen as ink for the work is highlighted in red

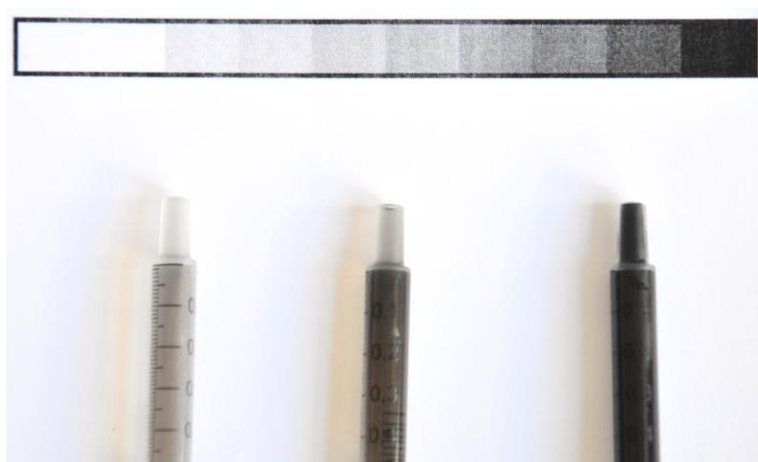


Figure VI.1.1 Three 1,2-Dichlorobenzene-based solutions in three different concentrations: a) 0.01 wt.% b) 0.02 wt.% c) 0.05 wt.%

DMF, a widely used solvent for CNTs, turned out to be very inefficient to disperse this particular type of MWCNTs. So was isopropanol and acetone. Because all water-based inks contained bundles of CNTs big enough to obstruct the ejection nozzles of the inkjet printer, they are discarded.

Between the chlorobenzene-based and the dichlorobenzene-based ink, the latter is more conductive. Consequently, dichlorobenzene is selected as solvent for the production of the ink. Among the different concentrations tested, we select the 0.02 wt.% because it represents the best compromise between the number of CNTs

dispersed (and consequently the conductivity of the ink) and the size of the bundles of CNTs.

The resulting dispersion is stable for more than 3 months.

VI.1.1.2 Substrate selection

A variety of polymeric substrates is tested to selected the optimal material to fabricate the device. Here below we list the tested polymers, supplied by Goodfellow.

PET (Polyethylene terephthalate, thickness 300 μ m): despite being widely used in the domain of flexible electronics (Logothetidis, 2014), it is not compatible with the dichlorobenzene-based ink.

PEI (Polyetherimide, thickness 175 μ m): the resulting devices are poorly conducting. Under microscopy, it seemed that the surface of deposition was lightly abraded, probably due to poor compatibility with Dichlorobenzene. For this reason PEI is discarded.

Even if PTFE (Polytetrafluoroethylene, thickness 300 μ m) is resistant to chemicals, it can't be used since we did not manage to deposit a uniform and conductive layer on it. Moreover we cannot obtain a good adhesion of the deposition.

On ETFE (Ethylene-Tetrafluoroethylene Copolymer, thickness 125 μ m) we achieved the most uniform deposition. The deposited layer is conductive and reproducible. It is our best candidate for the dichlorobenzene-based ink.

FEP (Fluorinated Ethylene Propylene Copolymer, thickness 100 μ m) is compatible with Dichlorobenzene, but the deposition is uneven and the resulting layer is not conductive.

Among the different polymers under test, the most promising results are obtained on ETFE, justifying the choice as substrate for the entire work.

VI.1.1.3 Ink enhancement for higher uniformity and reproducibility

Despite the deposition of dichlorobenzene-based CNT ink on EFTE was by far the most uniform among the different pair of ink-substrate, if observed under optical microscopy, it is possible to notice discontinuities and pattering at a micro scale (Figure VI.1.2a). We attribute this to poor wettability of the CNT solution on the substrate. As suggested by the literature we add surfactants to decrease the surface tension of the solution (Vaisman, et al., 2006) (Hopkins, et al., 2011) (Geng, et al., 2008) (Clark, et al., 2011) (Park, et al., 2012). The deposition of the resulting solution is uniform, as shown in Figure VI.1.2b.

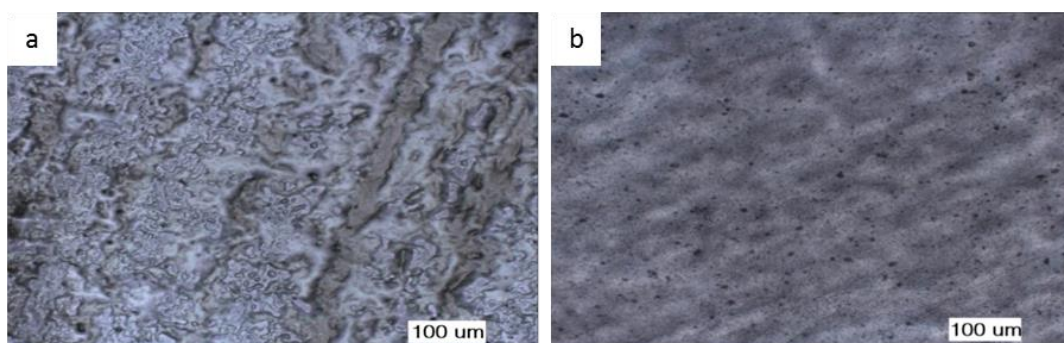


Figure VI.1.2 Optical image of the deposition of the CNT ink based on dichlorobenzene on EFTE. a) Without addition of surfactants. b) With addition of surfactants (SDBS, 0.3 wt.%) in the solution.

VI.1.1.4 Development of an effective rinsing process

Even though it appears continuous under optical microscopy, a single inkjet-printed layer is poorly conducting (resistance above 1 GΩ). This can be attributed both to the presence of leftover by-products trapped in the CNT network and to poor quality and conductivity of the used CNTs. The first suggestion is confirmed by SEM images (Figure VI.1.3a) that clearly show the presence of leftover SDBS particles as well as dichlorobenzene trapped in the CNT matrix.

A rinsing process is designed to eliminate these by-products. After several tests consisting of immersion and slight agitation of the samples in different solvents and the inspection of the result with SEM, methanol and acetone are identified as the best solvents to eliminate respectively SDBS crystals and dichlorobenzene.

Consequently, the rinsing process used in the fabrication consists of immersion and slight agitation in methanol and acetone for 8 s each, followed by drying under nitrogen flow.

This process removes most surfactant and solvent, though some traces of solvent can still be observed (Figure VI.1.3b). By depositing several layers, the voids are filled and the conductivity rapidly increases.

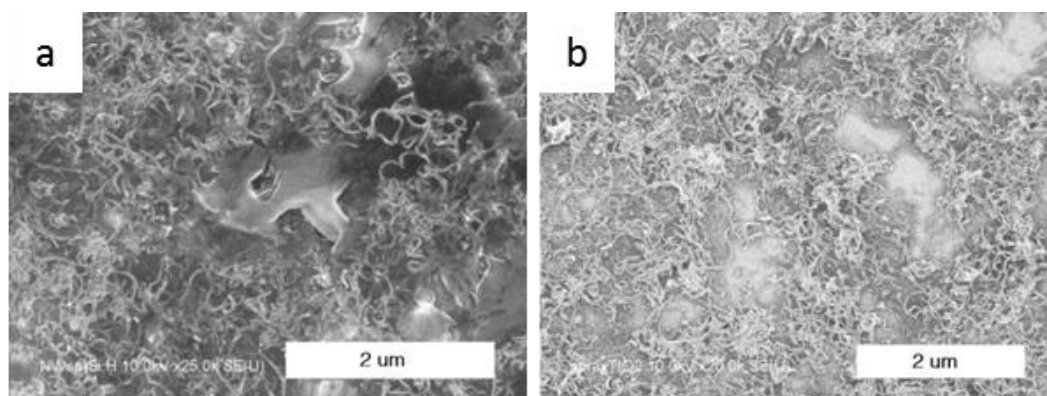


Figure VI.1.3 Effect of rinsing on the CNT network at the micro scale. a-b) SEM image of a single layer deposition a) before rinsing. b) after rinsing. We observe a clear removal of most surfactant and solvent traces.

VI.1.1.5 Deposition of contacts

In order to provide electrical contacting to the device, two possibilities are investigated: deposition of metal contacts by inkjet deposition and deposition via evaporation.

All metal inks available in the laboratory at the time of the tests required a curing process at more than 100°C, a temperature that causes irreversible changes to the polymeric substrate. Moreover the adhesion of such inks is relatively low on ETFE. These reasons pushed us to investigate the other contacting technique.

The gold evaporation proved to be the most promising technique because the substrate stays at a temperature lower than 25°C, the adhesion is considerably higher on ETFE, and the metallic sheet deposited follows the substrate under mechanical deformation without cracking.

Consequently, gold evaporation was selected as the technique to deposit the electrodes during the fabrication of the devices. We deposit pairs of 100 nm thin, 5 mm x 5 mm Au electrodes using thermal evaporation under vacuum (10⁻⁷ mbar).

Moreover this technique allows us to fabricate 72 pairs of electrode at once with a mask specifically designed for the purpose. Figure VI.1.4

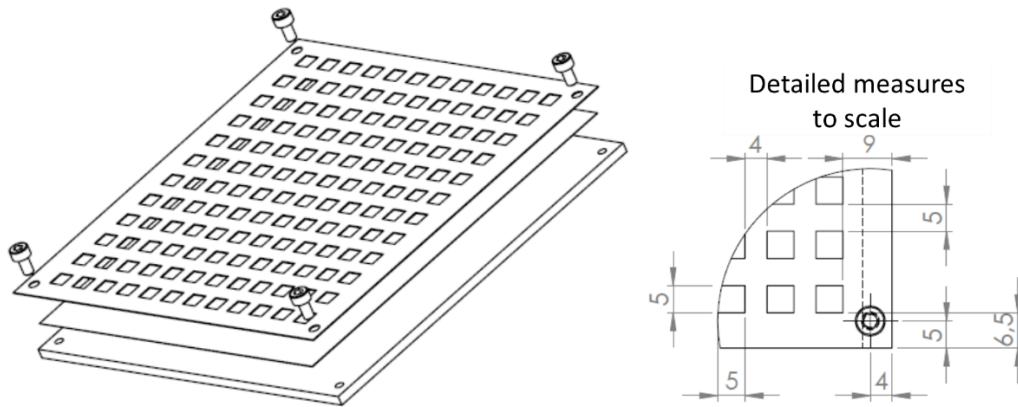


Figure VI.1.4 Evaporation mask designed for the deposition of 72 pairs of electrodes.

VI.1.2 Fabrication of the sensors

The fabrication process is highly reproducible and allows the serial production of sensors. In the following paragraphs, we describe the different steps.

VI.1.2.1 Substrate cleaning

The substrates are first cleaned with acetone bath for 10 s and dried under nitrogen flow.

VI.1.2.2 Electrode deposition

The electrodes are deposited as second task because it requires physical contact between the substrate and the mask. Depositing the electrodes after the inkjet deposition could damage the CNT network just deposited.

Figure VI.1.5 shows the substrate on which 72 pairs of gold electrodes were deposited.

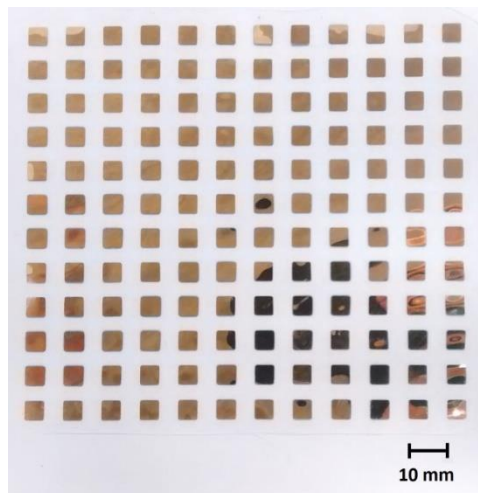
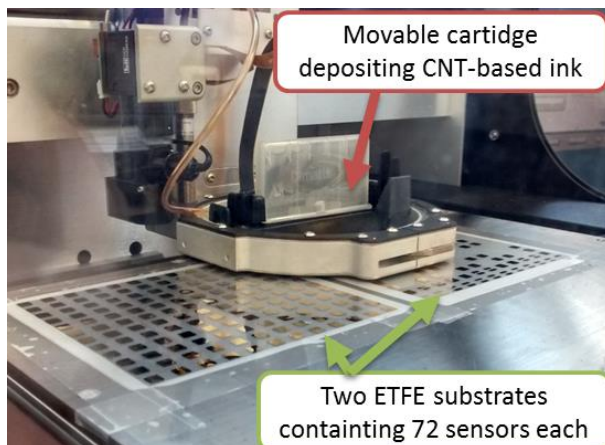


Figure VI.1.5 Evaporation of gold electrodes on polymeric substrate.

VI.1.2.3 Inkjet deposition and rinsing process

The third step involved depositing the CNT-based ink on the substrate by inkjet printing. 20 layers are deposited to decrease the resistivity of the device and every two depositions the device is rinsed to eliminate the by-product trapped in the CNT network .



VI.2 APPENDIX 2 – BIBLIOGRAPHY OF THE AUTHOR

PUBLICATIONS IN JOURNALS AND CONFERENCE PROCEEDINGS:

Accepted paper with corrections required:

- Michelis, F.; Bodelot, L.; Bonnassieux, Y.; Lebental, L. 2015 *Highly reproducible, hysteresis-free, flexible strain sensors by inkjet printing of carbon nanotubes*. Carbon

Papers under submission:

- Michelis, F.; Laheurte, J.-M.; Zaki, F.; Bodelot, L.; Bonnassieux, Y.; Lebental, L. (expected September 2015) *Wireless Nano Sensors for Embedded Durability Monitoring in Concrete*. Carbon
- Michelis, F.; Bodelot, L.; Bonnassieux, Y.; Lebental, L. (expected October 2015) *Modelling of piezoresistive behaviour of Carbon NanoTube networks above percolation threshold*. Applied Physics Letters
- Lebental, B.; Ghaddab, B.; Gaudefroy, V.; Michelis, F.; Ruiz Gracia, C.; Aranda, P.; Ruiz Hitzky, E. (expected July 2015) *Piezoresistive thin film of graphene-on clay/carbon nanotubes for Weigh In Motion application*. Building and Construction Materials

First author of articles published in proceeding of:

- Michelis, F.; Laheurte, J.-M.; Zaki, F.; Bodelot, L.; Bonnassieux, Y.; Lebental, L. 2015 *Wireless Nanosensors for Embedded Measurement in Concrete Structures* Proceedings to Nanotechnology in Construction 5 – Chicago (USA)
- Michelis, F.; Lebental, B.; Bodelot, L.; Cojocaru, C.-S. ; Sorin, J.L.; Bonnassieux, Y. 2014 *Wireless flexible strain sensor based on CNTs for Structural Health Monitoring*. Proceedings to TechConnect World 2014 – Washington DC (USA)
- Michelis, F.; Lebental, B.; Bodelot, L.; Cojocaru, C.-S. ; Sorin, J.L.; Aboushady, H.; Bonnassieux, Y. 2014 *Wireless flexible strain sensor based on Carbon Nanotube Piezoresistive Networks for Embedded Measurement of Strain in Concrete*. Proceedings to European Workshop of Structural Health Monitoring – Nantes

Author of articles published in proceeding of:

- Ghaddab, B.; Gaudefroy, V.; Michelis, F.; Ruiz Gracia, C.; Aranda, P.; Ruiz Hitzky, E.; Lebental, B. 2014 *A novel weigh-in-motion sensor using asphalt-embedded thin film of graphene-on-clay and carbon nanotubes* Proceedings to International Conference & Exhibition on Advanced & Nano Materials (ICANM) - Calgary (Canada)
- Ghaddab, B.; Lebental, B.; Gaudefroy, V.; Michelis, F.; Ruiz Hitzky, E.; Aranda, P.; Ruiz Gracia, C. 2014 *An innovative sensor for weigh-in-motion applications* Proceedings to European Workshop of Structural Health Monitoring – Nantes

PRÉSENTATIONS IN WORKSHOPS WITHOUT PROCEEDINGS:

- Sense-City inauguration
- IDRW 2014 - 10th French Korean Joint Workshop
- LPICM Seminar, Ecole Polytechnique (February 2014)
- Doctoriales 2013 – Ecole Polytechnique (September 2013)
- Poster à la Journée Sense-City : 1ères Rencontres Académiques-Industriels Nov.2013

VI.3 APPENDIX 3 – TEACHING AND SUPERVISION OF STUDENTS

TEACHING AT ESIEE PARIS
(ECOLE SUPÉRIEURE D'INGÉNIEURS EN ÉLECTRONIQUE ET ÉLECTROTECHNIQUE)

TOTAL NUMBER OF TEACHING HOURS: 120H

Teaching in the International Master of Science in Electronics

Teaching activities: Lecturer for Courses and Tutorials

Taught modules:

- Modelling and Simulation of MEMS
- Principles of MEMS Sensors and Actuators
- Optoelectronics and Photonics
- Advanced Electron Devices
- Electron Devices

Teaching in the First two years of Bachelor's degree

Teaching activities: Lecturer for Tutorials

Taught Modules:

- Electrostatics
- Physics – Mechanics
- Physics – Vector Calculus
- Physics – Wave Optics
- Digital Acquisition and Converters

CO-SUPERVISION OF STUDENTS IN RESEARCH ACTIVITIES

End-of-studies internships:

Fadi ZAKI (Université Paris Est)	Circuit de conditionnement d'un capteur résistive à base de nanotubes de carbone
Benjamin CADUC (Ecole Polytechnique)	Performances d'un capteur résistif à base de nanotubes de carbone multi-parois pour la mesure du pH
Aladdin KABALAN Houssam RETIMA (Université Paris Est)	Design of a meander-like antenna for communication through concrete

Apprenti Ingegneur:

Yaowu ZANG (Institut d'Optique)	Développement et optimisations de capteurs à base de nanocomposants
------------------------------------	---

Research projects:

Marc CHACHUAT Guillaume GENTHIAL Olivier MOINDROT Carolina NIJSSEN Léa SAVIOT (Ecole Polytechnique)	Capteurs à base de nanocomposants
Pauline LAMOTTE Elisa MESSIO (Ecole Polytechnique)	Caractérisation de capteurs CNT

VII. BIBLIOGRAPHY

Aİtcin, P. C., 2003. The durability characteristics of high performance concrete : a review. *Cement and Concrete Composites*.

ALChemE, 2015. *Electrokinetics*. [Online]
Available at: http://alcheme.tamu.edu/?page_id=6823
[Consultato il giorno 6 7 2015].

America's Cement Manufacturers, 2015. *Aggregates*. [Online]
Available at: <http://www.cement.org/cement-concrete-basics/concrete-materials/aggregates>
[Consultato il giorno 22 06 2015].

AMS, 2013. *SL900A Datasheet*, s.l.: s.n.

Andringa, M., Neikirk, D. P., Dickerson, N. & Wood, S., 2005. *Unpowered wireless corrosion sensor for steel reinforced concrete*. Irvine, CA, s.n.

Aouad, M., Stokoe II, K. H. & Briggs, R., 1993. Stiffness of Asphalt Concrete Surface Layer from Stress Wave Measurements. *Transportation Research Record*.

Arkema, 2008. *Arkema Graphistrength Multi Walled Carbon Nanotubes*, s.l.: Arkema Group.

Arrawatia, M., Baghini, M. & Kumar, G., 2011. *RF energy harvesting system from cell towers in 900MHz band*. Bangalore, s.n.

Azhari, F. & Banthia, N., 2012. Cement-based sensors with carbon fibers and carbon nanotubes for piezoresistive sensing. *Cement and Concrete Composites*.

Back, J. H. & Shim, M., 2006. Ph-dependent electron-transport properties of carbon nanotubes. *The Journal of Physical Chemistry B*, 110(47), pp. 23736-23741.

Baeza, F. J., Galao, O., Zornoza, E. & Garcés, E., 2013. Multifunctional Cement Composites Strain and Damage Sensors Applied on Reinforced Concrete (RC) Structural Elements. *Materials*.

Baeza, F. J., Galao, O., Zornoza, E. & Garcés, E., 2013. Multifunctional Cement Composites Strain and Damage Sensors Applied on Reinforced Concrete (RC) Structural Elements. Volume 6, pp. 841-855.

Balasubramanian, K. & Burghard, M., 2005. Chemically Functionalized Carbon Nanotubes. *Small Journal*, 1(2).

Balberg, I. & Binenbaum, N., 1985. Cluster structure and conductivity of three-dimensional continuum systems. *PHYSICAL REVIEW A*, 31(2).

-
- Bao, W. S., Meguid, S. A., H., Z. Z. & Zeng, G., 2012. Tunneling resistance and its effect on the electrical conductivity of carbon nanotube nanocomposites. *Journal of Applied Physics*, 111(093726).
- Barone, P. W., S. B., Heller, D. A. & Strano, M. S., 2005. Near-infrared optical sensors based on single-walled carbon nanotubes. *Nature Materials* , Volume 4, pp. 86-92.
- Barroca, N. et al., 2013. Wireless sensor networks for temperature and humidity monitoring within concrete structures. *Construction and Building Materials*.
- Baskar Rao, M. et al., 2009. Structural Health Monitoring (SHM) Using Strain Gauges, PVDF Film and Fiber Bragg Grating (FBG) Sensors: A Comparative Study. *Proc. National Seminar on non-Destructive Evaluation* , pp. 332-337.
- Bauer-Reich, C. et al., 2014. *An Investigation of the Viability of UHF RFID for Subsurface Soil Sensors*. Milwaukee, USA, s.n.
- Baughman, R. H., Zakhidov, A. A. & Heer, W. A. d., 2002. Carbon Nanotubes—the Route Toward Applications. *Science*, Volume 297, p. 787.
- Bazant, M., 2011. *Mit course 10.626/10.426 : Compact part of the double*, s.l.: s.n.
- Bazant, Z. P., 1988. Material models for structural creep analysis. In: *Mathematical modelling of Creep and Shrinkage of Concrete*. s.l.:Wiley & Sons.
- Bazant, Z. P. & Oh, B., 1983. Crack band theory for fracture of concrete. *Matériaux et Constructions*, 16(93).
- Bellucci, S., 2005. Carbon nanotubes: physics and applications. *Physica Status Solidi* , 2(1).
- Benchirouf, A. et al., 2012. *Investigation of RFID passive strain sensors based on carbon nanotubes using inkjet printing technology*. s.l., s.n.
- Bentz, D. P. & Garboczi, E. J., 1991. Percolation of phases in a three-dimensional cement paste microstructural model. *Cement and Concrete Research*.
- Berhan, L. & Sastry, A. M., 2007. Modeling percolation in high-aspect-ratio fiber systems. I. Soft-core versus hard-core models. *Physical Reviews E*, 75(041120).
- Bernhard, J., Hietpas, K., George, E. & Kuchima, D., 2003. *An interdisciplinary effort to develop a wireless embedded sensor system to monitor and assess corrosion in the tendons of prestressed concrete girders*. s.l., s.n.
- Bhadra, S. et al., 2013. A Wireless Passive Sensor for Temperature Compensated Remote pH Monitoring. *IEEE Sensors Journal*.
- Bhadra, S., Thomson, D. J. & Bridges, G. E., 2013. A wireless embedded passive sensor for monitoring the corrosion potential of reinforcing steel. *Smart Material Structures*, 22(075019).
- Bhattacharyya, R., Floerkemeier, C., Sarma, S. & Deavours, D., 2011. *RFID tag antenna based temperature sensing in the frequency domain*. Orlando, FL, USA, s.n.

- Bocca, M. et al., 2011. A Synchronized Wireless Sensor Network for Experimental Modal Analysis in Structural Health Monitoring. *Computer-Aided Civil and Infrastructure Engineering*, Volume 26, p. 483–499.
- Bradley, K., Gabriel, J.-C. P. & Grüner, G., 2003. Flexible Nanotube Electronics. *Nano Letters*, 3(10), pp. 1353-1355.
- Caduc, B., 2014. *Performances d'un capteur résistif à base de nanotubes de carbone multi-parois pour la mesure du pH*, s.l.: s.n.
- Cahill, P. et al., 2014. *Structural Health Monitoring of Reinforced Concrete Beam Using Piezoelectric Energy Harvesting System*. s.l., s.n.
- Cao, C. L. et al., 2011. Humidity sensor based on multi-walled carbon nanotube thin films. *Journal of Nanomaterials*, Volume 2011.
- Cazeca, M., Meada, J., Chenb, J. & Nagarajana, R., 2013. Passive wireless displacement sensor based on RFID technology. *Sensors and Actuators A*.
- Cerioti, M. et al., 2009. *Monitoring heritage buildings with wireless sensor networks: the Torre Aquila deployment*. San Francisco, s.n.
- Chae, M., Yoo, H., Kim, J. & Cho, M., 2012. Development of a wireless sensor network system for suspension bridge health monitoring. *Automation in Construction*, p. 237–252.
- Chang, C.-Y. & Hung, S.-S., 2012. Implementing RFIC and sensor technology to measure temperature and humidity inside concrete structures. *Construction and Building Materials*.
- Chang, N.-K., Su, C.-C. & Chang, S.-H., 2008. Fabrication of single-walled carbon nanotube flexible strain sensors with high sensitivity. *Applied Physics Letters*, 92(063501).
- Cheng, L. et al., 2004. Dynamic load monitoring of the Tsing Ma Bridge using a high-speed FBG sensor system. *Engineering Structures*.
- Cho, S. et al., 2008. Smart Wireless Sensor Technology for Structural Health Monitoring of Civil Structures. *Steel Structures*, Volume 8, pp. 267-275.
- Clark, M. D., Subramanian, S. & Krishnamoorti, R., 2011. Understanding surfactant aided aqueous dispersion of multi-walled carbon nanotubes. *Journal of Colloid and Interface Science*, 354(1), pp. 144-151.
- Cohen, D. J., Mitra, D., Peterson, K. & Maharbiz, M. M., 2012. A Highly Elastic, Capacitive Strain Gauge Based on Percolating Nanotube Networks. *Nano Letters*, Volume 12, pp. 1821-1825.
- Colybris, 2011. *MEMS accelerometers for building & structural health monitoring*, Neuchatel: s.n.
- Cottey, A. A., 1938. The electrical conductivity of thin metal films with very smooth surfaces. *Thin Solid Films*, 1(4), p. 297–307.

Cottinet, P.-J. et al., 2013. Strain phenomenon in carbon nanotube buckpaper actuator: Experiments and modelling. *Sensors and Actuators A*, Volume 194, pp. 252-258.

Crossbow Technology Inc., 2005. *MICA 2 Mote - Technical Sheet*, s.l.: s.n.

Cusson, D., Lounis, Z. & Daigle, L., 2011. Durability Monitoring for Improved Service Life Predictions of Concrete Bridge Decks in Corrosive Environments. *Computer-Aided Civil and Infrastructure Engineering*, p. 524-541.

Dalmas, F. et al., 2004. Carbon nanotube-filled polymer of electrical conductivity in composites Numerical simulation three-dimensional entangled fibrous networks. *Journal of Material Science*, Volume 39, pp. 4441-4449.

De Donno, D., Catarinucci, L. & Tarricone, L., 2013. An UHF RFID Energy-Harvesting System Enhanced by a DC-DC Charge Pump in Silicon-on-Insulator Technology. *Microwave and Wireless Components Letters*, 23(6).

DeGarmo, E. P., Black, J. T. & Kohser, R. A., 2003. *Materials and Processes in Manufacturing*. s.l.:Wiley.

Dehghani, S., Moravvej-Farshi, M. K. & Sheikhi, M. H., 2012. Temperature Dependence of Electrical Resistance of Individual Carbon Nanotubes and Carbon Nanotubes Network. *Modern Physics Letters B*, 26(21).

Derrida, B., Stauffer, D., Hermann, H. J. & Vannimenus, J., 1983. Transfer matrix calculation of conductivity in three-dimensional random resistor networks at percolation threshold. *Journal de Physique - Lettre*, Volume 44.

Dimatix, Inc., 2007 . *Dimatix Materials Printer - DMP-2800 Series User Manual*, s.l.: s.n.

Divsholi, B. S. & Yang, Y., 2014. Combined embedded and surface-bonded piezoelectric transducers for monitoring of concrete structures. *NDT&E International*.

Dong, S.-G. et al., 2011. Effective monitoring of corrosion in reinforcing steel in concrete constructions by a multifunctional sensor. *Electrochimica Acta*.

Dongyu, X. et al., 2015. Temperature and loading effects of embedded smart piezoelectric sensor for health monitoring of concrete structures. *Construction and Building Materials*.

Dumoulin, C. et al., 2012. Monitoring of the ultrasonic P-wave velocity in early-age concrete with embedded piezoelectric transducers. *Smart Materials and Structures*.

Engineering, O., s.d. *STRAIN GAGE TECHNICAL DATA*, s.l.: s.n.

Fallah Rad, M. & Shafai, L., 2009. *A wireless embedded sensor for SHM applications*. s.l., s.n.

Fisher | Moore, 1999. *Ethylene tetrafluoroethylene (ETFE) Technical Information*, s.l.: s.n.

Fisher, F., Bradshaw, R. & Brinson, L., 2003. Fiber waviness in nanotubereinforced polymer composites-1: modulus predictions using effective nanotube properties. *Composites Science Technology*, 63(11), pp. 1689-1703.

FLIR Systems, Inc, 2011. *Assessment of Concrete Bridge Structures Using Infrared Thermography*, s.l.: s.n.

Fujifilm, 2007. *Dimatix Materials Printer - DMP-2800 Series User Manual*, s.l.: Dimatix, Inc., rev.15 ver.1.6.0.1 08/01/07.

Fursa, T., Demikhova, A. A. & Vlasov, V. A., 2014. The Relationship of the Structural Characteristics of Concrete with the Parameters of the Electrical Response Upon Elastic Impact Excitation. *Russian Journal of Nondestructive Testing*.

Furtado, C. A. et al., 2003. Debundling and Dissolution of Single-Walled Carbon Nanotubes in Amide Solvents. *Journal of American Chemical Society*, pp. 6095-6105.

Geiger, A. & E., S. H., 1982. Tests of universality of percolation exponents for a three-dimensional continuum system of interacting waterlike particles. *Physical Review Letters*.

Gekon Inc. , 2015. *Fibre Optic Strain Gauge*, Lebanon, USA: s.n.

Geng, Y. et al., 2008. Effects of surfactant treatment on mechanical and electrical properties of CNT/epoxy nanocomposites. *Composites Part A: Applied Science and Manufacturing*, 39(12).

Geokon Inc., 2015. *Rebar Strainmeters - 4911 Datasheet*, Lebanon, USA: s.n.

Geokon Inc., 2015. *Vibrating Wire Strain Gauges - 4200 series - Datasheet* , Lebanon, USA: s.n.

Ghaddab, B. et al., 2014. *Piezoresistive thin film of graphene-on clay/carbon nanotubes for Weigh In Motion application*. Calgary, s.n.

Gohier, A. et al., 2011. All-printed infrared sensor based on multiwalled carbon nanotubes. *Applied Physics Letters*, Volume 98, p. 063103.

Gopu, S. L. B., 2012. *Wave penetration in concrete*, s.l.: s.n.

Gou, P. et al., 2014. Carbon nanotube chemiresistor for wireless ph sensing. *Scientific report* , Volume 4.

Gou, P. et al., 2014. Carbon Nanotube Chemiresistor for Wireless pH Sensing. *Scientific Reports*.

Grow, R. et al., 2005. Piezoresistance of carbon nanotubes on deformable thin-film membranes. *Applied Physics Letters*, Issue 86.

Ha, D. W., Park, J. S., Kim, J. M. & Park, H. S., 2014. Structural Health Monitoring of Infrastructure Using Wireless Sensor System. *Ad Hoc Networks*, Volume 140.

-
- Han, B., Ding, S. & Yu, X., 2015. Intrinsic self-sensing concrete and structures: A review. *Measurement*.
- Han, J.-W., Kim, B., Li, J. & Meyyappan, M., 2012. Carbon Nanotube Based Humidity Sensor on Cellulose Paper. *The Journal of Physical Chemistry*, 116(41).
- Hansen, W., 2006. *Embedded Wireless Temperature Monitoring Systems For Concrete Quality Control*, Ann Arbor, University of Michigan: s.n.
- Hayasaka, I., 1976. *Method of manufacturing a resistor having a low temperature coefficient*. US Patent 3,979,823.
- Hecht, D., Hu, L. & Grünera, G., 2006. Conductivity scaling with bundle length and diameter in single walled carbon nanotube networks. *Applied Physics Letters*, 89(133112).
- Hierold, C., Jungen, A., Stampfer, C. & Helbling, T., 2007. Nano electromechanical sensors based on carbon nanotubes. *Sensors and Actuators A: Physical*, 136(1), pp. 51-61.
- HighestBridges.com, 2015. *HighestBridges.com*. [Online]
Available at: http://www.highestbridges.com/wiki/index.php?title=Millau_Viaduct
[Consultato il giorno 15 02 2015].
- Hilaire, A. et al., 2013. *Analysis of Concrete Creep in Compression, Tension and Bending: Numerical Modeling*. s.l., s.n.
- Hoffmann, H. & Vancea, J., 1981. Critical assessment of thickness-dependent conductivity of thin metal films. *Thin Solid Films*, 85(2), p. 147–167.
- Hopkins, A. R., Straw, D. C. & Spurrell, K. C., 2011. Influence of surface chemistry on inkjet printed carbon nanotube films. *Thin Solid Films*, Volume 250.
- Hoseini, M., Bindiganavile, V. & Banthia, N., 2009. The effect of mechanical stress on permeability of concrete: A review. *Cement & Concrete Composites*, Volume 31.
- Hsieh, Y.-M. & Hung, Y.-C., 2008. A scalable IT infrastructure for automated monitoring systems based on the distributed computing technique using simple object access protocol Web-services. *Automation in Construction*, 18(4), pp. 424-433.
- Hsu, T. T., 1984. Fatigue and microcracking of concrete. *Matériaux et Constructions*, 17(97).
- Hua, B., Chenb, W. & Zhou, J., 2013. High performance flexible sensor based on inorganic nanomaterials. *Sensors and Actuators B*, p. 522– 533.
- Huang, Y. & Terentjev, E., 2012. Dispersion of Carbon Nanotubes: Mixing, Sonication, Stabilization, and Composite Properties. *Polymers*, pp. 275-295.
- Hu, B., Chenb, W. & Zhou, J., 2013. High performance flexible sensor based on inorganic nanomaterials. *Sensors and Actuators B*, Volume 176, pp. 522-533.

Hu, C. et al., 2012. Inkjet Printing of Nanoporous Gold Electrode Arrays on Cellulose Membranes for High-Sensitive Paper-Like Electrochemical Oxygen Sensors Using Ionic Liquid Electrolytes. *Analytical Chemistry*, pp. 3745-3750.

Hu, L., Hecht, D. S. & Gruner, G., 2004. Percolation in Transparent and Conducting Carbon Nanotube Networks. *Nano Letters*, 4(12).

Hu, N. et al., 2010. Investigation on sensitivity of a polymer/carbon nanotube composite strain sensor. *Carbon*, Volume 48, pp. 680-687.

Hu, X., Wang, B. & Ji, H., 2013. A Wireless Sensor Network-Based Structural Health Monitoring System for Highway Bridges. *Computer-Aided Civil and Infrastructure Engineering*, Volume 28, pp. 193-209.

Identec Solutions, 2006. *Active UHF Tag i-Q32T - Technical Sheet*, s.l.: s.n.

Identec Solutions, 2012. *i-Q350 - Technical Sheet*, s.l.: s.n.

IFSTTAR, 2015. *Sense-city : Nanosensors for cities and the environment*. [Online] Available at: <http://www.ifsttar.fr/en/research-expertise/major-projects/sense-city-nanosensors-for-cities-and-the-environment/> [Consultato il giorno 02 06 2015].

Intel, 2006. *Intel® Mote 2 Engineering Platform*, s.l.: s.n.

Ishida, H. & Furukawa, H., 2014. Wireless Power Transmission Through Concrete Using Circuits Resonating at Utility Frequency of 60 Hz. *IEEE Power Electronics*, 30(3).

Jansen, K., 2011. *Concrete Bridge Substructure*. [Online] Available at: <http://ceephotos.karcor.com/tag/column/> [Consultato il giorno 07 07 2015].

Jiang, S., 2011. *Optimum Wireless Power Transmission for Sensors Embedded in Concrete*, s.l.: Florida International University.

John, D. G., Searson, P. C. & Dawson, J. L., 1981. Use of AC Impedance Technique in Studies on Steel in Concrete in Immersed Conditions. *British Corrosion Journal*.

Kada, H. et al., 2002. Determination of the coefficient of thermal expansion of high performance concrete from initial setting. *Materials and Structures*, 35(1).

Kaempgen, M. & Roth, S., 2006. Transparent and flexible carbon nanotube/polyaniline pH sensors. *Journal of Electroanalytical Chemistry*, 586(1).

Kharkovsky, S., Qingzhao, K. & Gangbing, S., 2014. Cure-state monitoring of concrete and mortar specimens using Smart Aggregates. *Proceedings Instrumentation and Measurement Technology Conference (I2MTC)*.

Kim, J., Yun, J.-H., Song, J.-W. & Han, C.-S., 2009. The spontaneous metal-sitting structure on carbon nanotube arrays positioned by inkjet printing for wafer-scale production of high sensitive gas sensor units. *Sensors and Actuators B*, p. 587-591.

-
- Kim, S., 2005. *Wireless Sensor Networks for Structural Health Monitoring*, University of California at Berkeley: s.n.
- Kim, S. et al., 2012. Surface modifications for the effective dispersion of carbon nanotubes in solvents and polymers. *Carbon*, 50(1), pp. 3-33.
- Kim, S. et al., 2006. *Wireless Sensor Networks for Structural Health Monitoring*. s.l., s.n.
- Kim, S. et al., 2007. *Health Monitoring of Civil Infrastructures Using Wireless Sensor Networks*. s.l., s.n.
- Kim, T., Byun, J., Song, H. & Hong, Y., 2012. *Inkjet-printed SWCNT films for stretchable electrode and strain sensor applications*. s.l., s.n., pp. 143 - 144.
- Kirkpatrick, S., 1973. Percolation and Conduction. *REVIEWS OF MODERN PHYSICS*, 45(4).
- Ko, J. & Ni, Y., 2005. Technology developments in structural health monitoring of large-scale bridges. *Engineering Structures*, Volume 27, p. 1715–1725.
- Komuro, N., Takaki, S., Suzuki, K. & Citterio, D., 2013. Inkjet printed (bio)chemical sensing devices. *Analytical and Bioanalytical Chemistry*, 405(17), pp. 5785-5805.
- Kong, J. et al., 2000. Nanotube Molecular Wires as Chemical Sensors. *Science*, 287(5453).
- Kong, J. et al., 2000. Nanotube Molecular Wires as Chemical Sensors. *Science*, Volume 287, p. 622.
- Kottapalli, A. V. et al., 2003. *Two-tiered wireless sensor network architecture for structural health monitoring*. San Diego, CA, s.n.
- Kumar, S., Murthy, J. & Alam, M. A., 2005. Percolating Conduction in Finite Nanotube Networks. *Physical Review Letters*, 95(066802).
- Kurata, M. et al., 2011. *Long-term assessment of an autonomous wireless structural health monitoring system at the new Carquinez Suspension Bridge*. s.l., s.n.
- Kwon, O.-S. et al., 2013. Fabrication and characterization of inkjet-printed carbon nanotube electrode patterns on paper. *Carbon*, Volume 58, pp. 116-127.
- Laflamme, S., Kollosche, M., Connor, J. & Kofod, G., 2013. Robust Flexible Capacitive Surface Sensor for Structural Health Monitoring Applications. *Journal of Engineering Mechanics*, 139(7), pp. 879-885.
- Lau, P. H. et al., 2013. Fully Printed, High Performance Carbon Nanotube Thin-Film Transistors on Flexible Substrates. *Nano Letters*, 13(8), pp. 3864-3869.
- Lavric, J., Zineelabidine, A., L, B. & Peigney, M., 2015. *Étude de la piézorésistivité au sien de capteurs de contraintes à base de nanotubes de carbone*, s.l.: Ecole Polytechnique.

Le Cam, V. & Martin, W., 2011. *Guide de mise en oeuvre de PEGASE - Plateforme Experte Générique pour applications sans-fil embarquées*, s.l.: IFSTTAR - A3IP.

Lebental, B., 2010. *Instrumentation immergée des matériaux cimentaires par des micro-transducteurs ultrasoniques à nanotubes de carbone : perspectives pour le contrôle non destructif in-situ de durabilité*, s.l.: Université Paris Est.

Lebental, B. et al., 2014. *Capteur pour la chaussée à base de couches minces piézorésistives de nanoparticules noyées dans le matériau de chaussée*. France / FR 14 52842.

Lee, B. Y. et al., 2011. Universal Parameters for Carbon Nanotube Network-Based Sensors: Can Nanotube Sensors Be Reproducible?. *ACS Nano*, 5(6), pp. 4373-4379.

Lee, J. H., Yang, D., Kim, S. & Park, I., 2013. Stretchable strain sensor based on metal nanoparticle thin film for human motion detection & flexible pressure sensing devices. *The 17th International Conference on Solid-State Sensors, Actuators and Microsystems*, pp. 2624-2627.

Lesch, A. et al., 2014. Large scale inkjet-printing of carbon nanotubes electrodes for antioxidant assays in blood bags. *Journal of Electroanalytical Chemistry*, Volume 717-718, pp. 61-68.

Li, C. & Chou, T., 2008. Continuum percolation of nanocomposites with fillers of arbitrary shapes. *Applied Physics Letters*, 90(17).

Li, C., Thostenson, E. & Chou, T.-W., 2008. Effect of nanotube waviness on the electrical conductivity of carbon nanotube-based composites. *Composites Science and Technology*, Volume 68.

Li, H. et al., 2006. Structural Health Monitoring System for the Shandong Binzhou Yellow River Highway Bridge. *Computer-Aided Civil and Infrastructure Engineering*, Volume 21.

Lim, C. C., G. N. & Sirivivatnanon, V., 2000. Microcracking and chloride permeability of concrete under uniaxial compression. *Cement & Concrete Composites*, Volume 22.

Lin, C., Wang, H. & Yang, W., 2010. Variable percolation threshold of composites with fiber fillers under compression. *Journal of Applied Physics*, Volume 108.

Lipomi, D. J. et al., 2011. Skin-like pressure and strain sensors based on transparent elastic films of carbon nanotubes. *Nature Nanotechnology*, Volume 6, pp. 788-792.

Li, S. et al., 2014. Working mechanisms of strain sensors utilizing aligned carbon nanotube network and aerosol jet printed electrodes. *Carbon*, Volume 73, pp. 303-309.

Li, Y. & Kröger, M., 2012. A theoretical evaluation of the effects of carbon nanotube entanglement and bundling on the structural and mechanical properties of buckypaper. *Carbon*, 50(5), pp. 1793-1806.

-
- Li, Y. et al., 2006. Mechanical and NH₃ sensing properties of long multi-walled carbon nanotube ropes. *Carbon*, 44(9), pp. 1821-1825.
- Logothetidis, S., 2014. *Handbook of Flexible Organic Electronics: Materials, Manufacturing and Applications*. s.l.:Elsevier.
- Loh, K. J. et al., 2007. Multifunctional layer-by-layer carbon nanotube–polyelectrolyte thin films for strain and corrosion sensing. *Smart Materials and Structures*, Volume 16, pp. 429-438.
- Loh, K., Lynch, J., Shim, B. & Kotov, N., 2007. Tailoring Piezoresistive Sensitivity of Multilayer Carbon Nanotube Composite Strain Sensors. *Journal of Intelligent Material Systems and Structures*, 19(7), pp. 747-764.
- Ltd, T. S. K. C., 2011. *TML Strain Gauge Performance Characteristics*, s.l.: s.n.
- Lukschová, Š., Příkryl, R. & Pertold, Z., 2007. Petrographic examination of concrete from 20th and identification of reactive components. *Proceedings to the 5th International Conference on Arch Bridges* .
- Luo, H. et al., 2001. Investigation of the electrochemical and electrocatalytic behavior of singlewall carbon nanotube. *Analytical Chemistry*, 73(5), pp. 915-920.
- Lynch, J. P. & Loh, K. J., 2006. Summary Review of Wireless Sensors and Sensor Networks for Structural Health Monitoring. *The Shock and Vibration Digest*.
- Lynch, J. P. et al., 2003. Field validation of a wireless structural monitoring system on the Alamosa Canyon Bridge. *10th Annual International Symposium on Smart Structures and Materials*.
- Mabrook, M. et al., 2009. The morphology, electrical conductivity and vapour sensing ability of inkjet-printed thin films of single-wall carbon nanotubes. *Carbon*, 47(3), pp. 752-757.
- Maiwald, M., Werner, C., Zoellmer, V. & Busse, M., 2010. INKtelligent printed strain gauges. *Sensors and Actuators A*, Volume 162, pp. 198-201.
- Manzari, S. et al., 2012. *Polymer-doped UHF RFID tag for wireless-sensing of humidity*. Orlando, FL, USA, s.n.
- Markman, G. D., Siegel, D. S. & Wrigh, M., 2008. Research and Technology Commercialization. *Journal of Management Studies*, 45(8).
- Materer, N., Apblett, A. & Ley, T., 2011. *Passive, wireless corrosion sensors for transportation infrastructure*, Midwest City, Oklahoma, USA: Oklahoma Transportation Center .
- Maune, H. & Bockrath, M., 2006. Elastomeric carbon nanotube circuits for local strain sensing. *Applied Physics Letters*, Volume 89.
- Mauter, M. S. & Elimelech, M., 2008. Environmental Applications of Carbon-Based Nanomaterials. *Environmental Science and Technology*, 42(16), pp. 5843-5859.
- Maxim Integrated, 2011. *MAXI452 Datasheet*, s.l.: s.n.

- MEMSIC Inc., s.d. *IRIS Mote - Technical Sheet*, San Jose, California: s.n.
- Merlino, P. & Abramo, A., 2011. An Integrated Sensing/Communication Architecture for Structural Health Monitoring. *IEEE Sensors Journal*, 9(11).
- Meyers, S. L., 1951. Thermal expansion characteristics of hardened cement paste and of concrete. *Highway Research Board Proceedings*, Volume 30.
- Michelis, F. et al., 2014. Wireless Flexible Strain Sensor Based on Carbon Nanotube Piezoresistive Networks for Embedded Measurement of Strain in Concrete.. *EWSHM - 7th European Workshop on Structural Health Monitoring*.
- Mirica, K., Azzarelli, J. M. W. J. G., Schnorr, J. M. & Swager, T. M., 2013. Rapid prototyping of carbon-based chemiresistive gas sensors on paper. *PNAS*, pp. 3265-3270.
- MO, H.-B. & ZHOU, Z.-Q., 2009. Development of Microwave Testing Technique. *Nondestructive Testing*.
- Moradi-Marani, F., Rivard, P., Lamarche, C. & Kodjo, S., 2014. Evaluating the damage in reinforced concrete slabs under bending test with the energy of ultrasonic waves. *Construction and Building Materials*.
- Muttoni, A. & Ruiz, M. F., 2005. *Effets différés*, Lausanne: Ecole Polytechnique Federale de Lausanne.
- Nachman, L. et al., 2005. *The Intel® Mote platform: a Bluetooth-based sensor network for industrial monitoring*. s.l., s.n.
- National Instrument, s.d. *NI 9212 Datasheet*, s.l.: s.n.
- NG Spice, 2014. *NG Spice Presentation*. [Online]
Available at: <http://ngspice.sourceforge.net/presentation.html>
[Consultato il giorno 12 05 2015].
- Nintanavongsa, P., Muncuk, U., Lewis, D. & Chowdhury, K., 2012. Design Optimization and Implementation for RF Energy Harvesting Circuits. *Emerging and Selected Topics in Circuits and Systems*, 2(1).
- Nishimoto, H., Kawahara, Y. & Asami, T., 2010. Prototype implementation of ambient RF energy harvesting wireless sensor networks. *Sensors*, pp. 1282-1287.
- Noh, J. et al., 2011. Integrable single walled carbon nanotube (SWNT) network based thin film transistors using roll-to-roll gravure and inkjet. *Organic Electronics*, 12(12), pp. 2185-2191.
- O'Toolea, M., Shepherdb, R., Wallace, G. G. & D., D., 2009. Inkjet printed LED based pH chemical sensor for gas sensing. *Analytica Chimica Acta*, p. 308–314.
- O'Connor, M. C., 2006. RFID Cures Concrete. *RFID Journal*.
- Ogawa, S. & Sato, T., 2008. *Monitoring of Concrete Structures Using Passive Type RFID Tags with Sensory Functions*. s.l., s.n.
- Ohtsu, M., 1996. The history and development of acoustic emission in concrete engineering. *Magazine of Concrete Research*.

Oldham, K., 2008. A Gouy–Chapman–Stern model of the double layer at a (metal)/(ionic liquid) interface. *Journal of Electroanalytical Chemistry*, Volume 613.

Omega, E., s.d. *Strain gauge technical data sheet*, s.l.: s.n.

Ong, J. B. et al., 2008. A Wireless, Passive Embedded Sensor for Real-Time Monitoring of Water Content in Civil Engineering Materials. *IEEE Sensor Journal*.

Paek, J. et al., 2005. A Wireless Sensor Network for Structural Health Monitoring: Performance and Experience. *Center for Embedded Network Sensing*.

Pandit, P., Ansal, V., Venkataramana, K. & Parthiban, P., 2013. Experimental investigation on corroded reinforced concrete beam in coastal environment using strain gauges. *International Journal of Engineering and Innovative Technology*, 3(5).

Park, J. et al., 2012. The Effect of Dispersed MWCNTs Using SDBS Surfactant on Bacterial Growth. *World Academy of Science, Engineering and Technology*, Volume 70.

Park, S., Ahmad, S., Yun, C. & Roh, Y., 2006. Multiple crack detection of concrete structures using impedance-based structural health monitoring techniques. *Experimental Mechanics*.

Peigney, A. et al., 2001. Specific surface area of carbon nanotubes and bundles of carbon nanotubes. *Carbon*, 39(4), pp. 507-514.

Perveen, K., Bridges, G. E., Bhadra, S. & Thomson, D. J., 2014. *Compact Passive Wireless Reinforced Concrete Corrosion Initiation Sensor That Can Be Installed in Existing Steel*. Nantes, France, s.n.

PowerCast, 2015. *P2110B datasheet*, s.l.: s.n.

Radiospare, 2008. *N11FA812011 Datasheet*, s.l.: s.n.

Rein, M., Breuer, O. & Wagner, H., 2011. Sensors and sensitivity: Carbon nanotube buckypaper films as strain sensing devices. *Composites Science and Technology*, p. 373–381.

Reyes-Reyes, M., Carroll, D. L., Blau, W. & López-Sandoval, R., 2011. Materials and Devices for Organic Electronics. *Journal of Nanotechnology*, Volume 2011.

Reza, F., Batson, G., Yamamuro, J. & Lee, J., 2003. Resistance changes during compression of carbon fiber cement composites. *Journal of Materials for Civil Engineering*.

Rigoni, F., Drera, G., Pagliara, S. & Goldoni, A., 2014. High sensitivity, moisture selective, ammonia gas sensors based on single-walled carbon nanotubes functionalized with indium tin oxide nanoparticles. *Carbon*, Volume 80, pp. 356-363.

Rocktest Telemac, 2015. *Embedded Strain Gauges - Datasheet*, Richmond, Australia: s.n.

Rossi, P. et al., 2012. Basic creep of concretes investigation of the physical mechanism by acoustic emission. *Cement and Concrete Research*, Issue 42.

RST Instruments Ltd., 2015. *Rebar Strain Meter Datasheet*, Maple Ridge, Canada: s.n.

RTS Instruments Ltd., 2015. *Vibrating Wire Strain Gauges Datasheet*, Maple Ridge, Canada: s.n.

Saha, A., Jiang, C. & Martí, A. A., 2014. Carbon nanotube networks on different platforms. *Carbon*, Volume 79, pp. 1-18.

Sample, A. & Smith, J., 2009. *Experimental results with two wireless power transfer systems*. s.l., s.n.

Sazonov, E., Li, H., Curry, D. & Pillay, P., 2009. Self-Powered Sensors for Monitoring of Highway Bridges. *IEEE Sensor Journal*, 9(11).

Scardaci, V. et al., 2012. *Carbon Nanotube network based sensors*. Birmingham, s.n.

Schwartz, G. et al., 2013. Flexible polymer transistors with high pressure sensitivity for application in electronic skin and health monitoring. *Nature Communications*, Volume 4.

Sebastian, J. et al., 2014. Health monitoring of structural composites with embedded carbon nanotube coated glass fiber sensors. *Carbon*, Volume 66, pp. 191-200.

Sebastian, J. et al., 2014. Health monitoring of structural composites with embedded carbon nanotube coated glass fiber sensors. *Carbon*, Volume 66, pp. 191-200.

Secor, E. B. et al., 2013. Inkjet Printing of High Conductivity, Flexible Graphene Patterns. *Journal of Physisical Chemistry Letters*, 4(8), pp. 1347-1351.

Sellevoid, E. J. & Bjøntegaard, Ø., 2006. Coefficient of thermal expansion of cement paste and concrete: Mechanisms of moisture interaction. *Materials and Structures*, 39(9).

Shams, K. & Ali, M., 2007. Wireless Power Transmission to a Buried Sensor in Concrete. *IEEE Sensors Journal*, 7(12), pp. 1573 - 1577.

Shan, X., Hao, J. & Hao, R., 2014. *Structural health monitoring method and apparatus based on optical fiber bend loss measurement*. USA .

Shi, D. et al., 2004. The effect of nanotube waviness and agglomeration on the elastic property of carbon nanotube-reinforced composites. *Journal of Engineering Material Technology*, 126(3), pp. 250-257.

Shi, X. H. & Shi, X., 2008. Chloride Permeability and Microstructure of Portland Cement Mortars Incorporating Nanomaterials. *Journal of the Transportation Research Board*.

Siegel, D. S., Veugelers, R. & Wright, M., 2007. Technology transfer offices and commercialization of university intellectual property: performance and policy implications. *Oxford Review of Economic Policy*, 23(4).

Sinnotta, S. B. & Rodney Andrews, R., 2001. Carbon Nanotubes: Synthesis, Properties, and Applications. *Critical Reviews in Solid State and Materials Sciences*, 23(1).

Sisgeo SRL, 2015. *SK40 Vibrating String Strain Gsanges Datasheet*, Masate, Italy: s.n.

Slobodian, P. et al., 2011. Effect of compressive strain on electric resistance of multi-wall carbon nanotube networks. *Journal of Experimental Nanoscience*, 6(3), p. 294–304.

Smarsly, K. & Lawb, K. H., 2014. Decentralized fault detection and isolation in wireless structural health monitoring systems using analytical redundancy. *Advances in Engineering Software*, Volume 73, pp. 1-10.

Song, J.-W. et al., 2009. The production of transparent carbon nanotube field emitters using inkjet printing. *Physica E*, pp. 1513-1516.

Sounthararajan, V. M. & Sivakumar, A., 2013. Corrosion Measurements in Reinforced Fly Ash Concrete Containing Steel Fibres Using Strain Gauge Technique. *International Journal of Corrosion*, Volume 2013.

Soutsos, M., Bungey, J. & Millard, S., 2001. Dielectric properties of concrete and their influence on radar testing,. *NDT&E International*, Volume 34.

Srinivasan, R., Carkhuff, B. G., Phillips, T. E. & Saffarian, H., 2006. *Miniature Wireless Full Spectrum EIS Corrosion Sensor*. s.l., s.n.

Srivastava, R. K. et al., 2011. The strain sensing and thermal–mechanical behavior of flexible multi-walled carbon nanotube/polystyrene composite films. *Carbon*, 49(12), pp. 3928-3936.

Stadermann, M. et al., 2004. Nanoscale study of conduction through carbon nanotube networks. *Physical Reviews B*, 69(201402).

Storey, M., van der Gaag, B. & Burns, B., 2011. Advances in on-line drinking water quality monitoring and early warning systems. *Water Research*.

Straser, E. G., Kiremidjian, A. S. & Meng, T. H., 1998. *Modular, wireless damage monitoring system for structures*. US 6292108 B1.

Taris, T., Vigneras, V. & Fadel, L., 2012. *A 900MHz RF energy harvesting module*. s.l., s.n.

Tawie, R. & Lee, H. K., 2010. Piezoelectric-based non-destructive monitoring of hydration of reinforced concrete as an indicator of bond development at the steel–concrete interface. *Cement and Concrete Research*.

Test Consult, 2015. *Bridge & Structure Monitoring*. [Online]

Available

at:

<http://www.testconsult.co.uk/itemdetail.aspx?id=52&dept=instrumentation-and->

monitoring

[Consultato il giorno 12 02 2015].

Texas Instruments, 2008. *INA333 Datasheet*, s.l.: s.n.

Texas Instruments, 2013. *OPA333 Datasheet*, s.l.: s.n.

The Engineering Toolbox, 2015. *Coefficients of Linear Thermal Expansion*. [Online]

Available at: http://www.engineeringtoolbox.com/linear-expansion-coefficients-d_95.html

[Consultato il giorno 17 07 2015].

Tokyo Sokki Kenkyujo Co., l., 2011. *Strain Gauge Performance Characteristics*, s.l.: s.n.

University of California - Berkeley, 2015. *Aggregates for Concrete*, s.l.: s.n.

University of California - Berkley , 2015. *Aggregates for Concrete*, s.l.: s.n.

Vaisman, L., Wagner, H. D. & Marom, G., 2006. The role of surfactants in dispersion of carbon nanotubes. *Advances in Colloid and Interface Science*, Volume 128.

Van Zijl, G. P. A. G., 2000. *Computational modelling of masonry creep and shrinkage*, Delft: Technische Universiteit Delft.

Vena, A., Sorli, B., Foucaran, A. & Belaizi, Y., 2014. *A RFID-enabled sensor platform for pervasive monitoring*. Montpellier, s.n.

Wang, C. et al., 2012. Extremely Bendable, High-Performance Integrated Circuits Using Semiconducting Carbon Nanotube Networks for Digital, Analog, and Radio-Frequency Applications. *Nano Letters*, Volume 12, pp. 1527-1533.

Wang, J., 2005. Carbon-nanotube based electrochemical biosensors: A review. *Electroanalysis*, 17(1).

Wang, Y., Lynch, J. P. & Law, K. H., 2005. *Validation of an integrated network system for real-time wireless monitoring of civil structures*. s.l., s.n.

Watters, D., Bahr, D., Jayaweera, P. & Huestis, D., 2003. *SMART PEBBLES™: Passive Embeddable Wireless*, Sacramento, CA, USA: SRI International.

Wenzel, H., 2009. *Health Monitoring of Bridges*. s.l.:Wiley & Sons.

Whelan, M. J., Gangone, M. V., Janoyan, K. D. & Jha, R., 2009. Real-time wireless vibration monitoring for operational modal analysis of an integral abutment highway BRIDGE. *Engineering Structures*, 30(10), p. 2224–2235.

World Economic Forum, 2014. *The Global Competitiveness Report 2014–2015*, Geneva: s.n.

Xiao, H., Li, H. & Ou, J., 2011. Self-monitoring Properties of Concrete Columns with Embedded Cement-based Strain Sensors. *Journal of Intelligent Material Systems and Structures*, 22(2), pp. 191-200.

-
- Yamada, T. et al., 2011. A stretchable carbon nanotube strain sensor for human-motion detection. *Nature Nanotechnology*, Volume 6, pp. 296-301.
- Yin, G. et al., 2011. A carbon nanotube/polymer strain sensor with linear and anti-symmetric piezoresistivity. *Journal of Composite Materials*, pp. 1315-1323.
- Yu, H. & Caseres, L., 2010. *Corrosion sensor*. US 8833146 B2.
- Yu, M.-F., Lourie, O., Dyer, M. J. & Moloni, K., 2000. Strength and Breaking Mechanism of Multiwalled Carbon Nanotubes Under Tensile Load. *Science*, Volume 287, p. 637.
- Yu, X. & Kwon, E., 2009. A carbon nanotube/cement composite with piezoresistive properties. *Smart Material Structures*.
- Yu, Y. et al., 2013. Influence of filler waviness and aspect ratio on the percolation threshold of carbon nanomaterials reinforced polymer nanocomposites. *Journal of Materials Science*, Volume 48, pp. 5727-5732.
- Zhang, R. et al., 2013. Strain sensing behaviour of elastomeric composite films containing carbon nanotubes under cyclic loading. *Composites Science and Technology*, pp. 1-5.
- Zhang, R. et al., 2013. Strain sensing behaviour of elastomeric composite films containing carbon nanotubes under cyclic loading. *Composites Science and Technology*, 74(24), pp. 1-5.
- Zhao, H., Zhang, Y., Bradford, P. D. & Zhou, Q., 2010. Carbon nanotube yarn strain sensors. *Nanotechnology*, Volume 21.
- Zheng, J., Wong, H. & Buenfeld, N., 2009. Assessing the influence of ITZ on the steady-state chloride diffusivity of concrete using a numerical model. *Cement and Concreat Researches*.
- Zhu, X. Q., Hao, H. & Fan., K. Q., 2013. Detection of delamination between steel bars and concrete using embedded piezoelectric actuators/sensors. *Journal of Civil Structural Health Monitoring*.